Magnetisation Texture Motion Driven by Spin Currents: Simulation and Measurement

Lin Huang

University of Leeds

School of Physics and Astronomy

Submitted in accordance with the requirements for the degree of

Doctor of Philosophy

March, 2024

Intellectual Property Statement

The candidate confirms that the work submitted is his own and that appropriate credit has been given where reference has been made to the work of others.

Acknowledgements

Firstly, I would like to thank my supervisors, Prof. Christopher Marrows, Dr. Gavin Burnell and Dr. Simon Connell, for their supervision and support during the project. I am especially thankful for Chris's suggestion on my simulation works and step-by-step support about communicating with the editor for paper publishment. Chris provided much-needed encouragement to me during the COVID lab lockdown. Also, I am thankful for Gavin's help in setting up the lock-in amplifier and current resources for our experiments. I am grateful for Simon's expertise with Atomic Force Microscopy. His explanation about the equipment performance helped me find a way to optimise the MFM measurement.

I am extremely grateful for all the help and kindness received from our Condensed Matter Physics group. From the first time training on the equipment I had never used before to the shared moments of joy during hikes, I gained so much power to keep a positive mind and work hard. Many thanks to Dr. Mannan Ali, who runs our group safely day by day. He also gave us a chance to think and understand the principle of the standard operation steps, such as why we wanted to use the equipment with different gas pressures instead of just remembering the numbers we could put in. Also, thank you so much to Dr. Philippa Shepley, Dr. Matthew Rogers and Dr. Nathan Satchell, who gave me training early in my PhD. I would like to thank my colleague, Md Golam Hafiz. We collaborated closely to enhance the performance of sputtered SiO_x.

During the experimental part of this project, I spent many late nights in the AFM lab. Many thanks to Dr. Lekshmi Kailas. Her help was indispensable in addressing technical issues with the AFM system.

This journey would have been significantly more challenging without the supportive community at the University of Leeds. Again, thanks to all the people who provided help to me during my PhD.

Finally, I must thank my friends and family. Over a quarter of my time in Leeds was during the COVID lockdown. Their communication reduced my loneliness and encouraged me to face the difficulties during my PhD.

Whenever I start a new adventure, these cherished moments during my PhD will light up the way I go and warm my heart forever.

Abstract

This thesis contains the study results of magnetic texture motion induced by spin currents through both simulation analyses and experiments. The exploration into the force interactions between spin currents and magnetic textures furnishes a better understanding of the complex dynamical behaviour of these textures. More accurate predictability of magnetic texture responses within varied external conditions is crucial for applying magnetic texture as information carriers of spintronic devices.

Periodic heterostructures of ferromagnetic materials and heavy metals were fabricated via sputtering techniques. The samples presented pronounced Dzyaloshinskii-Moriya Interaction (DMI). This interaction helps the stabilization of magnetic textures. The initial step was characterizing the magnetic properties of the Ta/$[Pt/Co_{68}B_{32}/Ir]_n$/Pt system. These characterized magnetic parameters were used in subsequent micromagnetic simulations. The simulation results demonstrated the possibility of stabilizing skyrmions on our samples with an external magnetic field. More importantly, simulations found the different behaviours of skyrmion in varied widths and damping characteristics tracks. The result analysis revealed that the initial trajectory of the skyrmion is altered upon the balance between spin transfer torque from the transmitted spin wave, linear momentum transfer torque from the reflected spin wave and the repulsive forces from the sample edges.

The latter portion of this project is the experimental investigations of domain dynamics driven by spin currents from thermal gradients along the narrow tracks. Magnetic Force Microscopy (MFM) was used to look for the domain position before and after the heating application. An Oersted field due to the applied dc current must be accounted for the displacement of the domains. The effects of the Oersted field and thermal gradients were discussed. Ultimately, we observed the domain driven by a series of thermal gradients on the metal sample.In recent research, insulating materials, such as YIG, are widely used because they ensure that electric currents do not interfere with the magnetic texture movements or the pure spin current dynamics being studied. The results of our research can give the researchers more choices from designable magnetic heterostructures

than traditional insulating magnetic materials.

Contents

List of Figures

List of Tables

Abbreviations

AFM	Antiferromagnet	ac	Alternating Current
dc	Direct Current	DW	Domain wall
FM	Ferromagnet	HM	Heavy metal
LMTT	Linear momentum transfer torque	LLG	Landau- Lifshitz- Gilbert
MFM	Magnetic force microscopy	MOKE	Magneto-optic Kerr effect
MLA	Maskless lithography aligner	OOMMF	Object oriented micromagnetic framework
OOP	Out of plane	SQUID	Superconducting quantum interference device
SkHE	Skyrmion Hall effect	SOC	Spin oribit coupling
SW	Spin wave	STT	Spin transfer torque
SP-STM	Spin-resolved scanning tunnelling microscopy	XMCD	X-ray magnetic circular dichroism
VFM	Varying field microscopy	XRR	X-ray reflectometry
PMA	perpendicular magnetic anisotropy		

Common Symbols

a	lattice constant	A_{ex}	Exchange stiffness
C	Spin wave stiffness constant	$\mathcal{D}$	Dissipative tensor
D_{DMI}	Dzyaloshinskii Moriya vector	d_{m}	Magnetic layer thickness
$\mathbf{f}$	Converted force	$\mathrm{F}_{\mathrm{edge}}$	Repulsive force from the sample edge
$\mathbf{G}$	Gryovector	g	g-factor
H	Field	j	Current density
K_{u}	anisotropy constant	L_{edge}	Penetration depth of the magnetisation twist
L_{mag}	Characteristic length scale of spin wave damping	$\mathbf{M}$	Magnetisation
M_{s}	Saturation magnetisation	n	Refractive index
O	Spin-depedent Seebeck effect coefficient	p	Momentum
$\mathbf{q}$	Wavevector	Q	Topologial charge
s	Spin quantum number or number of the neighbouring atoms	S	Density of entropy
$\hat{\mathbf{u}}$	Easy axis direction with unit vector	U	Skyrmion potential energy
$\mathbf{v}$	Velocity	V_{edge}	Potential of the repulsion from the sample edge
w	Sample width	α	Gilbert damping constant
β	Skyrmion Hall angle	μ_0	Vacuum permeability
γ	Electron gyromagnetic ratio	Ξ	Dimensionless parameter for force calculation
κ	Dimensionless parameter for force calculation	η	Dimensionless parameter for force calculation
σ	Scattering cross-section or current conductivity	Φ	Domain wall tilt angle or magnetic flux in an area

ΔT	Temperature difference	∇T	Temperature gradient
ρ	Normalised spin wave amplitude or g-factor	ϵ	Equilibrium distance of van der Waals force
δ	Real part of the refractive index	ι	Imaginary part of the refractive index

Chapter 1

Background Theory and Literature Review

1.1 Spintronic Devices and Skyrmionics Memory Devices

Electronic devices, such as transistors, digital logic gates, flash memory devices, and other functions in microscale circuits, are already commonly used in modern technology. After decades of development, people started expecting devices with smaller sizes and higher efficiency, and researchers started facing the disadvantages of electronic devices. Smaller transistors face the higher challenge of breakdown voltage, avalanche multiplication, current leaking and quantum-related challenges such as maintaining the coherence of qubits [1–4]. Joule heating is unavoidable to high-performance electronic devices because of the energy dissipation. Also, the rising heat changes the working environment of the electronic devices, which will limit the longevity and efficiency of the devices because of the thermal conductivity. The high-performance computer will need more energy to reduce the heat produced, which leads to high energy consumption [5, 6].

Unlike electronic devices, spintronic devices are based on the spin of electrons and take advantage of both the electrons and the spins. Because the spin of a single electron can be regarded as a magnetic moment, one of the most common applications of the spintronic device is the magnetic memory device [7–9].

Granular ferromagnetic materials are used to make traditional magnetic memory devices such as hard disk drives, and the magnetic domains are used to represent the digital information 0 or 1. Magnetic random-access memory (MRAM) is another type of traditional magnetic memory device, it uses the magnetic state of the magnetic tunnel junction (MTJ) to store information. However, the sizes of the storage elements limit the size of the magnetic memory device [10].

A smaller-sized magnetic element has high potential for the future magnetic memory device. Skyrmions are the smallest elements with different spin directions, which give more ways and spaces to compile information. Skyrmions have topological spin texture, the directions of spins have axial symmetry. Skyrmions can have different types of texture including Néel-type and Bloch-type. In most of the thin films, 2D texture can be characterised by the Pontryagin number (winding number) $Q = \int d^2 r \rho(r)$, where ρ is the topological charge density. Q describes the number of times the spins need to 'turn' from the centre of the skyrmion through the domain wall to the outside of the skyrmion, this is also related to the magnetisation axis of the core of skyrmion. The different types of skyrmions texture are listed in Fig. 1.1.

From Fig. 1.1(a), (b) and (g) is the skyrmion texture type with Q=-1. The Néel type and Bloch type skyrmions are most commonly used in the simulation. Only these two extreme types of skyrmions were identified from the chiral symmetry breaking magnetic materials in the experiment before 2018. [11–13] Antiskyrmions were observed in ($Mn_{1.4}Pt_{0.9}Pd_{0.1}Sn$) in 2019 [14]. The antiskyrmion is shown in Fig. 1.1(c) and has winding number Q=+1. The combination of 2 skyrmions (d) has Q=-2 whereas the single vortex (e) and meron (f) both have Q=-0.5. Fig. 1.1(h) shows the texture called a skyrmionium and its Q value is 0.

Also, the skyrmions can be driven by current [15] has high potential to realise the high-speed and large information storage density spintronic devices.

Skyrme first defined the mathematical concept of a skyrmion in high-energy physics [16]. Skyrmionic states were assumed to be a non-equilibrium state, and those skyrmions would not appear as spontaneous ground states [17]. However, Bogdanov showed the theoretical possibility of getting skyrmions in magnetic materials due to chiral interactions like the Dzyaloshinskii-Moriya interaction (DMI) [18].

Traditionally, the magnetic materials are mostly simple bulk ferromagnets or antiferromagnets. In past decades, the research about the magnetic properties of all kinds of artificial thin or 2D samples that can host skyrmion attracted much attention. In 2009, by neutron scattering on the cubic B20 compound MnSi sample, a stable antiskyrmion helped the author prove that the effects of Gaussian thermal fluctuations need to be counted when stabilising the skyrmion [19]. Further studies were made and suggested that skyrmion can be written [20, 21], deleted [22] and read [23]. These show that skyrmionics is a promising region for computation and data storage.

1.2 Heterostructure of Heavy Metal/ Ferromagnetic Material/ Heavy Metal

Skyrmions can be created by different mechanisms, such as the dipolar interaction [24], the relativistic Dzyaloshinskii Moriya interaction (DMI) [25], frustrated exchange interactions [26] and four-spin exchange interactions [27]. In recent research, DMI is the most concentrated mechanism, and most research depends on it. DMI is the result of the non-negligible spin-orbit coupling (SOC) in lack of inversion symmetry magnetic system [25]. The phenomenological formula for the DMI is expressed by the

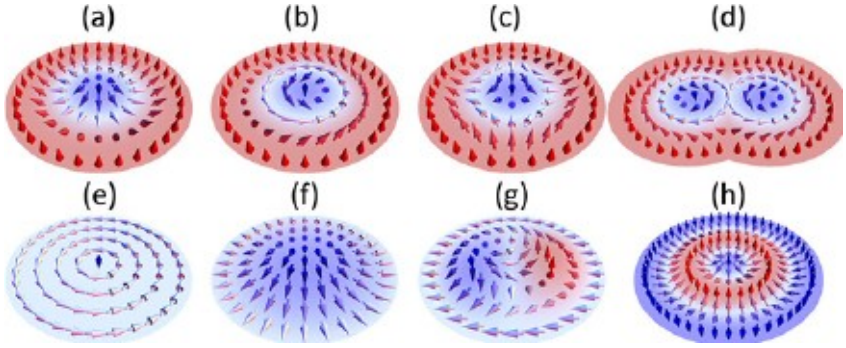

Figure 1.1: Series of skyrmion textures. The slyrmions with Q value equals to -1 (a) Néel-type skyrmion ; (b) Bloch-type; the texture with Q value equals to 1 (c) antiskyrmion; the texture with Q value equals to -2 (d) biskyrmion; the texture with Q value equals to -0.5 (e) vortex and (f) meron; the texture with Q value equals to -1 (g) bimeron, the texture with Q value equals to 0 (h) skyrmionium. [13]

$H_{\mathrm{DMI}} = -\mathbf{D}_{\mathrm{DMI}} \cdot \mathbf{S_1} \times \mathbf{S_2}$, where $\mathbf{D}_{\mathrm{DMI}}$ is the Dzyaloshinskii Moriya vector and S_1 and S_2 are adjacent spins. If the S_1 and S_2 have clockwise rotation, the energy of the spins will decrease.

To ensure the stable existence of the skyrmions and reduce the undesirable deviation of the skyrmions in the spintronic devices, researchers try to find materials that can have strong DMI and minimise the skyrmion Hall effect (SkHE). No only the velocity parallel or anti-parallel to the orientation of the driving current, the skyrmion also accompany with a transverse velocity.[28] Because of the skyrmion topology, the skyrmion experiences a quasiclassical force Magnus force in the current flow. The Magnus gyrotropic force force shifts the skyrmion trajectory perpendicular to the orientation of the current flow.[29, 30]

In multilayer structures, inversion symmetry is broken due to the interfaces between layers. Around 2015, more and more research teams pointed out that the Dzyaloshinskii-Moriya interaction will be more common in antiferromagnets (AFM) than ferromagnets (FM) [31]. Later, artificial materials like the FM/AFM coupled structures could theoretically get rid of the SkHE when driven by an applied force [32]. The skyrmion can also get rid of the SkHE in AFM structure driven by spin current or electron current. The skyrmion in the top and bottom AFM structure layer experience opposite Magnus force because of the opposite topological charge at each layer of the AFM structure. The cancellation of the Magnus force allows the skyrmion moves along the direction

of the driven current or spin wave. [30, 33]

So, the AFM and FM combined samples got many interests. The anisotropic frustrated magnet [34], heavy metal/ultrathin ferromagnet/insulator (HM/FM/Insulator) trilayers [35] and few of 2D Van der Waals crystals [26] were also proved to host skyrmions in theory. What is more, inversion symmetry is broken due to the interfaces in the multilayers' structure. The heterostructure of magnetic materials and heavy metals can have strong SOC. Skyrmions can be found in multilayers of magnetic metals [36] or metal films deposited on heavy metal substrates [27].

$Co_{68}B_{32}$ has strong perpendicular magnetic anisotropy (PMA). This means that its magnetic moments prefer to align perpendicular to the film plane. PMA is highly desirable in thin-film magnetic structures as it supports different magnetic textures in different repeat stacks [37]. Co is the key component of $Co_{68}B_{32}$, it has high spin polarization [38], which improves the efficiency of spin-transfer torque (STT) mechanisms in spin current dynamic. $Co_{68}B_{32}$ can form high-quality interfaces with common heavy metals. We chose Platinum (Pt) and Iridium (Ir) because they exhibit strong spin-orbit coupling. Considering the heavy metal and FM interface properties, the [Pt/$Co_{68}B_{32}$/Ir] heterostructure is the fundamental structure to find and stabilise the skyrmion with external magnetic field in this project.

1.3 Motion of Skyrmion Driven by Spin Currents

In order to read the information stored in the skyrmion, the skyrmion needs to move to the reader or the expected direction. The reading efficiency and accuracy are highly dependent on the position of skyrmions during the movement. So, the skyrmion motion driven by different methods is essential to be studied.

One of the tools to move a skyrmion to the detector is the injected electron current. Spin-transfer torque (STT) and spin-orbit torque (SOT) are two mechanisms of the current-driven skyrmion.

The STT is the effect from the electron polarized spins which influence the orientations of the magnetizations.[39] The SOT is from the interaction between the electron's spin and its orbital motion.[40] The spin of the electrons in the current and the current-induced effective magnetic field can exert a torque on the local magnetic moments to transfer the angular momentum. The dynamics of skyrmions caused by electron

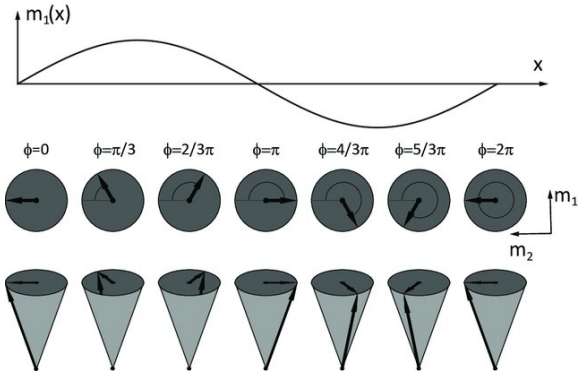

Figure 1.2: The harmonic spin wave visualized as a sequence of precessing magnetic moments with phases. [45]

currents are also interesting and significant in order to apply the effects in the industry [41][15]. But the spin current or spin wave (SW) is also a promising way to drive skyrmions [42]. Spin current is a flow of spin angular momentum. Not only the spin polarised electrons current can refer to the spin current, the collective magnetic motion of the spins as shown in Fig. 1.2 in a magnetic material can also be regarded as another type of spin current and known as spin wave.[43–45] The wavelength of the SW is the length when the length that phase change from 0 to 2π, the SW wave vector = $\frac{2\pi}{\lambda}$. Joule heating is directly related to the flow of charge but SW can propagate without the motion of electrical charge and most of the magnetic material is low magnetic damping, so SW can reduce the Joule heat with less energy consumption.

In recent years' published papers, the SW-driven skyrmion motion in simulations is still a hot topic. The SW twisted magnon can provide skyrmion with a rotated gyration motion [46]. The polarised laser can modify the SW flow direction, the skyrmions in skyrmion crystal in Cu_2OSeO_3 then can be rotated by the Magnus force from both SW and thermal gradient because the system is inhomogeneous. [47, 48]. The SW transmitted to the skyrmion will also give rise to the skyrmion diode effect based on the opposite motions of the skyrmion with different SW injected directions in a certain frequency and sample width. In the paper of Xichao Zhang's team [49], the motions of skyrmion at L corner and T junction were simulated. Because of the Magnus force, skyrmion prefers to turn left when there is no repulsive force from the edge. As shown in Fig. 1.3 (a), the skyrmion driven to the left when the SW excited from the bottom of the T junction. The skyrmion Fig. 1.3 (b) will not drop to the bottom of the T junction

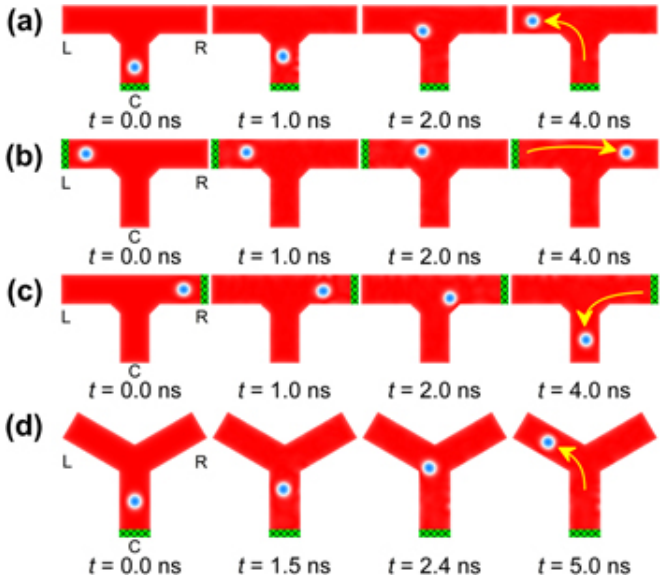

Figure 1.3: Snapshots of the skyrmion (Q = 1) locations driven by the SW excitated on different position of the T junction. (a) The SW propagated from the bottom of the T junction. The SW propagated from the (a) left and (b) right of the T junction. (c) Similar simulation when the skyrmion driven by the SW from the bottom of the Y junction. [49]

when the excitation of SW is on the left on the T junction while (c) it drops to the bottom of the T junction when the skyrmion is driven by the SW from the right of the T junction. The arrival of the skyrmion at the C branch can be the signal 1 (true) of the logic gate; contrarily, the absence of a skyrmion at the C branch is the signal 0 (false). Their consideration of reflection in simulation also shows the importance of the linear momentum transfer torque (LMTT) [50].

Not only affecting the skyrmion displacements on the x, y-axis, SW also affects the shape and structure of skyrmion by time-varying perpendicular sine field $H = H_0 \sin 2\pi f t$, the hybridised modes, and breathing modes because of the breaking of topological protection [51]. A sinusoidally varying magnetic field can be tuned to match the SW frequencies and the smoothly varying amplitude can minimize the sudden changes in the magnetic flux which might induce unwanted errors. The SW can propagate perpendicular to the plane of the skyrmion or along the strings of 3D skyrmions. As shown in Fig. 1.4, by measuring the varification of skyrmions topologic charges, positions and sizes along the skyrmion string direction, the skyrmion

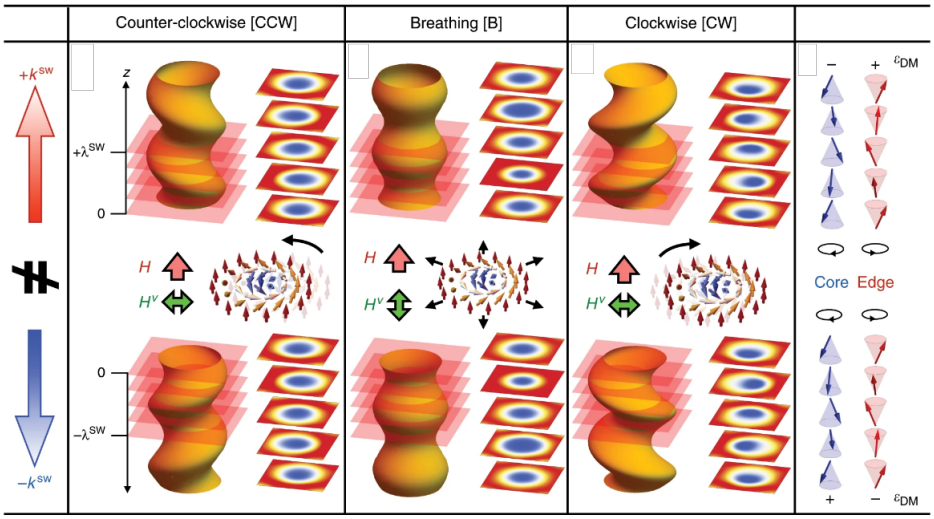

Figure 1.4: Schematic illustration of CCW, breathing, and CW excitation modes on skyrmion strings.[52]

anticlockwise and clockwise rotation modes and breathing modes can be determined. [52]. If the magnetic layer used in the future is thick and non-negligible, the rotation mode might also happen and show as a non-straight domain pattern when observed in the in-plane direction.

Most of the micromagnetic dynamic simulation models considered SW will be thoroughly scattered on domain walls or skyrmions, which can also explain the skyrmion Hall effect. The strength of the SW transmission and reflection can be gained by compare the upstream and the downstream amplitude SW amplitude. However, the strength of the scattering SW is hard to gain from the magnetisation data compared to the transmitted SW and reflected SW, it need to gain the amplitude of a SW in a propgation angle which the data collection started simulation cell will be complicated to determine. Also, the balance between spin transfer torque (STT) from transmitted SW and LMTT from reflected SW is more promising in explaining the transient retrograde skyrmion motion in our simulation result. The force model considers equivalent force from transmitted and reflected SW, which will be discussed in §1.6. The skyrmion driven by spin wave on varying track widths were simulated and showed a transient retrograde motion, which will be shown in Chapter 4.

Also, because of the spin Seebeck effect, the spin current can be generated in the magnetic material by heat gradient. In recently published papers, the discussed heat-

gradient-driven magnetic texture data are still mostly based on the simulation data [53–55]. The Seebeck coefficient is simply defined and different between papers, which causes confusion during calculations. In Yi's paper, the Seebeck coefficient based on the properties of the magnetic material is defined, which will be shown in §1.8.2 [56]. Some experimental papers present the domain wall or skyrmion lattice motion driven by the temperature gradient, and magnetic insulator samples have good results that can prove the skyrmions or domains will move towards the hot region [48, 57]. Comparing the conducting magnetic material, using an insulator can help people eliminate the effect of electron currents. But at the same time, the research of spin Seebeck effect-driven magnetic texture motion on conducting magnetic metal materials still remains blank. In this project, the components of the multilayers are all conducting. The domain wall motion observed by magnetic force microscopy (MFM) measurements is still similar to the domain wall motion in insulating materials, which will be shown and discussed in Chapter 7.

1.4 Imaging the Magnetic Patterns

There are a handful of ways to image the magnetic textures, such as the Kerr microscope, spin-resolved scanning tunnelling microscopy (SP-STM), X-ray magnetic circular dichroism (XMCD) and Magnetic Force Microscope (MFM). In recent years, most skyrmion spatial motions or results of skyrmion edge interaction were captured by magneto-optic Kerr effect (MOKE) [58, 59], or spin-resolved scanning tunnelling microscopy (SP-STM). We already successfully gained the demagnetisation pattern of the samples by Kerr microscope, but the image resolution with the largest expansion objective lens (x50) in the lab is not high enough for us to find skyrmion or distinguish skyrmion from the background with defects in real-time. The magnetic texture imaging tool becomes a better choice in this project since it can measure nanoscale texture.

Meanwhile, the MFM is widely used to present the changes of skyrmion sizes and shapes of different domains [60, 61]. MFM measurement showed current induced skyrmion on low pinning material CoFeB [62, 63]. Also, MFM measurement with varying external field microscopy (VFM) can show lots of magnetic texture dynamics. In some published papers, designed current pulse-driven skyrmion [64] and differ-

ent phases in hybrid ferromagnetic/ ferrimagnetic multistacks [65] were measured by MFM. Thermal induced skyrmion diffusion [66] and ac magnetic field induced skyrmion diffusion [58] were imaging by VFM. In Cao's paper [67], the normal MFM already shows a good performance on imaging skyrmion motion similar to the results in Chapter 5, a direct domain shape and location difference visualisation by adding external AC field on the whole sample and superparamagnetic probe of MFM were realised. The result perfectly matches the mathematical signal subtraction between the initial state MFM figure and the final state MFM figure. Though this method is clear to show domain wall (DW) shape-changing, it won't improve the single skyrmion motion observation because the 2D dot-like skyrmion position is already easily tracked by normal MFM. Also, the varying field will affect the SW excitation on the sample. To track the skyrmion motion driven by spin current, we can now only apply the current pulses and measure after the pulses because each high-resolution MFM image (at least 512 points per line) requires around 15 minutes to finish the scan of the interested area.

1.5 Skyrmion Dynamics

Numerical micromagnetic simulations are well-suited to studying SW-driven skyrmion dynamics, and there are many recent examples, in most of which the track for the skyrmions is narrower than 100 nm or not larger than 4 times the skyrmion diameter [42, 49, 50, 68–70]. By studying the skyrmion motion in tracks of different widths, we can predict the skyrmion motion in an experimentally easily achievable sample. Though the high performance lithography can create 100 nm wide track, the smallest feature size which the optical lithography equipment (MLA 150) in Leeds cleanroom can make is 600 nm. We also study the SW-driven skyrmion motion as a function of varying the Gilbert damping constant. Our simulations were carried out with the micromagnetics package Oommf [71]. The simulation is based on an iteration of the Landau- Lifshitz- Gilbert (LLG) equation:

$$\frac{d\mathbf{M}}{dt} = -\gamma \mathbf{M} \times \mathbf{H}_{\text{eff}} + \frac{\alpha \mathbf{M}}{M_{\text{s}}} \times \left(\frac{d\mathbf{M}}{dt} \right), \tag{1.1}$$

which is an equation of motion for the magnetisation $\mathbf{M}$, where $\gamma = -2.211 \times 10^5$ $\text{mA}^{-1}\text{s}^{-1}$ and α are the gyromagnetic ratio and Gilbert damping constant, respectively. (Here and throughout, we use SI units unless otherwise specified.) M_{s} is the saturation

magnetization. $\mathbf{H}_{\text{eff}}$ describes the effective fields in the system arising from energy terms such as the exchange stiffness, DMI, and anisotropies as well as the applied magnetic field [49], defined as the partial derivative of the free energy density E with respect to the magnetisation $\mathbf{M}$,

$$\mathbf{H}_{\text{eff}} = -\frac{1}{\mu_0}\frac{\partial E}{\partial \mathbf{M}}, \tag{1.2}$$

in which $\mu_0 = 4\pi \times 10^{-7}$ H/m is the vacuum permeability. The free energy density contains terms arising from the magnetic field $\mathbf{H}$, which includes both the externally applied field and the demagnetisation field, Heisenberg exchange with exchange stiffness A_{ex}, uniaxial anisotropy with anisotropy constant K_{u} and easy axis direction with unit vector $\hat{\mathbf{u}}$, and interfacial Dzyaloshinskii-Moriya interaction [71], and is written as

$$E = -\mu_0 \mathbf{M}\cdot\mathbf{H} + A_{\text{ex}}\nabla\left(\frac{\mathbf{M}}{M_{\text{s}}}\right)^2 - K_{\text{u}}\left(\frac{\mathbf{M}}{M_{\text{s}}}\cdot\hat{\mathbf{u}}\right)^2 + E_{\text{DMI}} + E_{\text{demag}}, \tag{1.3}$$

where the interfacial DMI energy is written as [72]

$$E_{\text{DMI}} = \frac{D_{\text{DMI}}}{M_{\text{s}}^2}\left(M_z\frac{\partial M_x}{\partial x} - M_x\frac{\partial M_z}{\partial x} + M_z\frac{\partial M_y}{\partial y} - M_y\frac{\partial M_z}{\partial y}\right), \tag{1.4}$$

with interaction strength D_{DMI}. And E_{demag} is the energy of the demagnetizationi.

$$E_{\text{demag}} = -\frac{\mu_0}{2}\int_V (\mathbf{M}\cdot(-\mathbf{NM}))\, d\tau, \tag{1.5}$$

where the demagnetic tensor $\mathbf{N}$ depends the geometry of the material and dictates how the magnetic field is distributed within it due to its own magnetization, the intergral is taken over the volume of the sample.[73, 74]

1.6 Force Model of Micromagnetic Simulation of Skyrmion Motion

In this section, we briefly review some relevant results on skyrmion motion to introduce concepts that we shall use later to describe our work.

The Thiele equation describes the dynamics of rigid magnetisation textures in response to driving forces [75] and was originally derived to treat bubble domains. It can thus also be used to treat the motion of skyrmions in response to driving forces

such as a current of magnons arising from a SW [76–78]. For a skyrmion spin texture with spatial co-ordinate **R**, it is written as

$$\mathbf{G} \times \mathbf{v} - \alpha \mathcal{D} \cdot \mathbf{v} = -\mathbf{f}(\mathbf{R}), \tag{1.6}$$

where the gyrovector $\mathbf{G} = (0, 0, G) = (0, 0, -4\pi Q)$, for a skyrmion with topological charge $Q = -1$. $\mathbf{v} = \dot{\mathbf{R}}$ is the velocity of skyrmion, whilst $\mathcal{D}$ is a dissipative tensor with the form $\begin{pmatrix} \mathbb{D} & 0 & 0 \\ 0 & \mathbb{D} & 0 \\ 0 & 0 & 0 \end{pmatrix}$ for an isolated skyrmion in a thin film [79]. $\mathbf{F} = -\nabla U$ is the force which is defined as the negative spatial derivative of the skyrmion potential energy U. Because of the $\mathbf{H}_{\text{eff}}$ definition and $f_{\mathbf{u}} = \gamma \int_S \mathbf{H}_{\text{eff}} \frac{d(\frac{\mathbf{M}}{M_s})}{d\mathbf{u}} dS$, where S is the non-uniform magnetisation surface and $\mathbf{u}$ can be either x or y, the converted force is represented in Eq. 1.6 by $\mathbf{f} = \mathbf{F}\gamma/(M_s \mu_0 d_{\text{m}})$, where d_{m} is the thickness of the magnetic layer [80] since a quantity with dimensions of velocity is required in that form of the Thiele equation.

This yields

$$\begin{aligned} \mathbf{G} \times \mathbf{v} - \alpha \mathcal{D} \cdot \mathbf{v} &= \left(4\pi Q v_y - \mathbb{D}\alpha v_x,\ -4\pi Q v_x - \mathbb{D}\alpha v_y, 0\right) \\ &= (-f_x, -f_y, 0), \end{aligned} \tag{1.7}$$

from which we obtain

$$v_x = \frac{1}{G^2 + \alpha^2 \mathbb{D}^2} \left(4\pi Q f_y + \alpha \mathbb{D} f_x\right), \tag{1.8}$$

and

$$v_y = \frac{1}{G^2 + \alpha^2 \mathbb{D}^2} \left(-4\pi Q f_x + \alpha \mathbb{D} f_y\right). \tag{1.9}$$

Motion in the x-direction is particularly interesting here since we define that as the spin wave propagation direction. The presence of the gyroscopic term in Eq. 1.6 means the y-component of force will also affect the skyrmion velocity along the x-axis, as shown in Eq. (1.8).

1.7 Forces on a Skyrmion

In the simulation work, we set up a skyrmion at the centre of a magnetic track which has magnetic properties same as the sample Ta/Pt/$Co_{68}B_{32}$/Ir/Pt. A Néel-type skyrmion will be formed by injected 2 ns width current pulse (current density = 10^8 A $cm^{-}2$)

and be stablized by a out of plane magnetic field. The magnetization informationwill be set as the initial state of the simulations. The forces on a skyrmion will from two sources. The principal source is the SW magnon current drive, $\mathbf{f}_{\text{mag}}$, that can include the scattering of SWs as well as the reflection, transmission, and absorption of SWs. Nevertheless, the repulsion at the edge of the sample also plays a role. Thus we can have $\mathbf{f} = \mathbf{f}_{\text{mag}} + \mathbf{f}_{\text{edge}}$ [81] in Eq. 1.6.

1.7.1 Force From the Sample edge: Repulsive Force

The repulsive force from the edges of a nanostrip of width w across the y-direction and thickness d_{m} as a function of skyrmion position y can be written as [81]:

$$\begin{aligned}\mathbf{F}_{\text{edge}} &= -V_{\text{edge}}\nabla\left[\exp\left(\frac{-(y+\frac{w}{2})}{L_{\text{edge}}}\right)+\exp\left(\frac{(y-\frac{w}{2})}{L_{\text{edge}}}\right)\right] \\ &= \mathbf{f}_0\left[\exp\left(\frac{-(y+\frac{w}{2})}{L_{\text{edge}}}\right)+\exp\left(\frac{(y-\frac{w}{2})}{L_{\text{edge}}}\right)\right]\frac{M_s\mu_0 d_{\text{m}}}{\gamma},\end{aligned} \tag{1.10}$$

where V_{edge} is used to parameterise the strength of the repulsion, and the penetration depth of the magnetisation twist being induced by the DMI at the sample edges is L_{edge}. We define l_{edge} as the normalized length

$$l_{\text{edge}} = L_{\text{edge}}/\sqrt{2A_{\text{ex}}/(\mu_0 M_{\text{s}}^2)}. \tag{1.11}$$

The physical parameters $\mathbf{f}_0$ and l_{edge} can be expressed in term of the dimensionless parameters $\Xi = D_{\text{DMI}}\sqrt{2/(\mu_0 M_{\text{s}}^2 A_{\text{ex}})}$, $\kappa = 2K_{\text{u}}/(\mu_0 M_{\text{s}}^2)$ and $\eta = H_z/M_{\text{s}}$ [82]. Here, H_z is the external out-of-plane magnetic field. We can then write the values of the force and interaction depth as

$$|\mathbf{f}_0| = \frac{e\pi}{\sqrt{2}}\left(\Xi - \frac{2}{|l_{\text{edge}}|}\right)\sqrt{\frac{2A_{ex}\gamma'^2}{\mu_0}}, \tag{1.12}$$

in which $e \approx 2.71828$ is Euler's number, and

$$|l_{\text{edge}}| = \frac{\pi^3\Xi}{-4(\pi^2-4)\eta + 2\pi^2\kappa}. \tag{1.13}$$

1.7.2 Magnetic Force from the Scattering Spin Wave

Considering the effect of SWs impinging on a skyrmion and scattering from it, $\mathbf{f}_{\text{mag}} = \mathbf{f}_{\text{scatter}}(\mathbf{R})$. In Ref. [81], the authors considered the force arising from spin wave scattering on skyrmion, with a decay of the scattering force based on the SW attenuation

owing to the distance between the SW source and skyrmion position $\mathbf{R}$. The scattering force is written as:

$$\begin{aligned}\mathbf{f}_{\text{scatter}}(\mathbf{R}) &= je^{\frac{-\mathbf{R}\cdot\hat{\mathbf{q}}}{L_{\text{mag}}}} q(\sigma_{\parallel}\hat{\mathbf{q}} + \sigma_{\perp}(\hat{\mathbf{z}} \times \hat{\mathbf{q}})) \\ &= je^{\frac{-R_x}{L_{\text{mag}}}} q(\sigma_{\parallel}\hat{\mathbf{x}} + \sigma_{\perp}\hat{\mathbf{y}}) \qquad (1.14) \\ &= f_{\text{scatter}\parallel}\hat{\mathbf{x}} + f_{\text{scatter}\perp}\hat{\mathbf{y}}, \qquad (1.15)\end{aligned}$$

where $\mathbf{q} = \hat{\mathbf{q}}q$ is the wavevector of the spin wave, assumed to be along the x-direction, and j is the magnon current density at the spin wave source position $j = \frac{|\mathbf{G}|v_e}{4\pi}$. The skyrmion effective velocity is $\mathbf{v}_e = \rho^2\frac{\hbar\mathbf{q}}{m}$, where ρ is the spin wave amplitude, q is the magnitude of SW wavevector and m is the magnon mass [83]. σ is the magnon scattering cross-section of the skyrmion,

$$\begin{pmatrix}\sigma_{\parallel}\\ \sigma_{\perp}\end{pmatrix} = \int_0^{2\pi}\begin{pmatrix}1-\cos\chi\\ -\sin\chi\end{pmatrix}\frac{d\sigma}{d\chi}\,d\chi, \qquad (1.16)$$

where χ is the scattering angle of the spin wave on skyrmion and $\frac{d\sigma}{d\chi}$ is the energy-dependent scattering cross-section. Usually, $\sigma_{\perp} \approx \frac{4\pi}{q}$ and $\sigma_{\parallel} \sim \frac{1}{q^2}$ [83, 84]. The skyrmion Hall angle is $\beta = \arctan\left(\sigma_{\parallel}/\sigma_{\perp}\right)$, so $f_{\text{scatter}\parallel}/f_{\text{scatter}\perp} = \tan\beta$. The parameter L_{mag} accounts for the attenuation of spin waves by the Gilbert damping according to

$$L_{\text{mag}} = \left(\alpha\sqrt{\frac{m}{2\hbar}2\pi f}\right)^{-1}, \qquad (1.17)$$

in which f is the spin wave frequency.

1.7.3 Magnetic Force from the Transmitted Spin Wave

To optimise the data analysis from getting the amplitude of the scattering spin wave with a skyrmion Hall angle to the reflected and transmitted spin wave from upstream and downstream of the skyrmion, we need to know the force model from the reflected and transmitted spin wave. For spin waves propagating along the track (x-direction) and perfect transmission through the skyrmion ($T = 1$, $R = 0$), the magnons must change their spin after passing through the domain wall at the skyrmion edge, and so transfer angular momentum to the local magnetisation, giving rise to a spin transfer torque (STT) on the magnetisation at that point [85]. In the Thiele approach of regarding the skyrmion as a particle, this torque gives rise to a force that leads to a skyrmion

velocity $\frac{-\rho^2}{2}\mathbf{v}_g$, where ρ is the SW amplitude normalised by the M_s, $\mathbf{v}_g = 2\gamma_0 A_{ex}\mathbf{q}$ is the spin wave group velocity, in which $\gamma_0 = 2\gamma/(\mu_0 M_s)$. The total force component in the SW propagation direction will only come from this STT between fully transmitted SW magnons and the skyrmion. Whilst this idea was developed for a one-dimensional domain wall [85], where the force from transmitted SW will simply align with the x-axis, here we generalise it to a two-dimensional skyrmion. Thus, we need to consider the component of $\mathbf{f}_{transmit}$ perpendicular to the SW propagation direction. This force on the skyrmion arising from STT can be written as

$$\mathbf{f}_{transmit} = f_{transmit\parallel}\hat{\mathbf{x}} + f_{transmit\perp}\hat{\mathbf{y}} \tag{1.18}$$

which leads to

$$\begin{aligned} -4\pi f_{transmit\perp} + \alpha\mathbb{D} f_{transmit\parallel} &= (G^2 + \alpha^2\mathbb{D}^2)v_x \\ &= \frac{-\rho^2 v_g (G^2 + \alpha^2\mathbb{D}^2)}{2}, \end{aligned} \tag{1.19}$$

where the ratio between $f_{transmit\parallel}$ and $f_{transmit\perp}$ is set as $\tan\beta$ [84] and $f_{transmit\parallel}$ is in the negative on x direction, as shown in Fig. 1.5.

1.7.4 Magnetic Force from the Reflected Spin Wave

To determine the effect of SW reflection, the excited magnon number density can be written as $n = \rho^2 M_s/(2\hbar\gamma)$, where ρ is the normalised spin wave amplitude. Since this is a volume density, to be able to apply it to the one-dimensional force calculation, we must multiply n by the cross-sectional area of the track. A skyrmion can be regarded as a circular reverse magnetic domain with a chiral domain wall between it and its surroundings. The spin orientations in a one-dimensional section along the central horizontal axis of a Néel skyrmion is a pair of Néel domain walls as shown in Fig. 1.5(c) [86, 87]. The magnetisation unit vector can be expressed in spherical coordinates as shown in Fig. 1.5(d). The linear momentum of the left-hand-side domain wall of the skyrmion in this 1D section only has an x-component given by $p_{DW} = M_s/\gamma \int \phi \sin\theta(\partial\theta/\partial x)dx = 2\Phi M_s/\gamma$, where θ is the angle between the magnetisation and the z-axis, and ϕ is the angle between the in-plane projection of the magnetisation and x-axis (as shown in Fig. 1.5(d). The domain wall tilt angle $\Phi = \phi$ at the center of the domain wall [88]. Conservation of linear momentum then gives the force arising

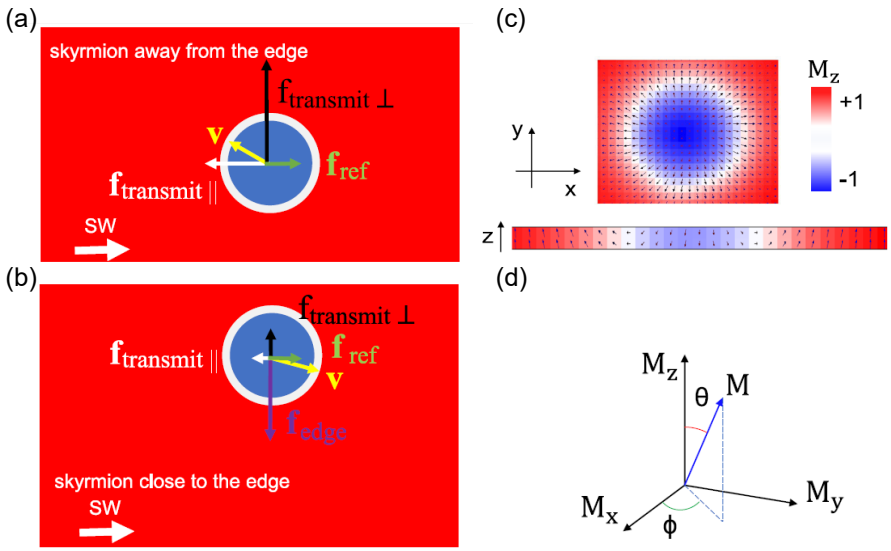

Figure 1.5: Spin wave driving forces for $Q = -1$ skyrmion. (a) When a free skyrmion experiences all the forces from impinging spin waves and the force from reflected spin waves is too small to overcome the effect from $\mathbf{f}_{\text{transmit}}$ and $\mathbf{f}_{\text{scatter}\perp}$, the skyrmion's longitudinal velocity component is opposite to the spin wave propagation direction. (b) Assuming the same transmitted SW is reduced, $\mathbf{f}_{\text{transmit}}$ can be overcome by $\mathbf{f}_{\text{ref}}$ and/or skyrmion is near enough to the track edge to experience edge repulsion, the additional force arising from linear momentum transfer can change the sign of the net longitudinal force and hence also the sign of longitudinal component of the velocity. The $\mathbf{v}$ is a unit vector pointing to the direction of the skyrmion velocity. (c) 2D diagram of skyrmion with 1D spin orientation. The bar under the skyrmion is a 1D section through the skyrmion along the x-axis. (d) The magnetisation unit vector in spherical coordinates.

from the reflection of magnons

$$\mathbf{F}_{\text{ref}} = \frac{d\mathbf{p}_{\text{DW}}}{dt} = -\frac{d\mathbf{p}_{\text{mag}}}{dt}, \tag{1.20}$$

where $\mathbf{p}_{\text{mag}}$ is the linear momentum of the magnons. Considering only x-components since that is the direction of magnon flow, we can then write

$$-\frac{dp_{\text{mag}}}{dt} = -nSv_g\delta p = -\frac{2M_s}{\gamma}\frac{d\Phi}{dt}, \tag{1.21}$$

where v_g is the magnitude of the spin wave group velocity, S is the cross-sectional area of the track, and the magnitude of the change in momentum is given by $\delta p = \hbar D_{\mathrm{DMI}}/A_{\mathrm{ex}}$ [20, 85, 88].

This means that

$$\frac{d\Phi}{dt} = -\frac{\rho^2 v_g \delta p}{4\hbar}, \tag{1.22}$$

and so

$$-\frac{dp_{\mathrm{mag}}}{dt} = \frac{M_s \rho^2 v_g D_{\mathrm{DMI}}}{2A_{\mathrm{ex}}\gamma}, \tag{1.23}$$

and so

$$\mathbf{f}_{\mathrm{ref}} = \left(\frac{\rho^2 \mathbf{v}_g D_{\mathrm{DMI}}}{2A_{\mathrm{ex}}\mu_0 d_m}, 0, 0\right). \tag{1.24}$$

$\mathbf{f}_{\mathrm{ref}}$ is a force that only has a component along the direction of magnon flow, defined here as the x-axis.

To have interaction between the magnons and skyrmion and the deflection of the skyrmion trajectory, the wavelength of magnons needs to be smaller than the skyrmion diameter. In our simulation, the spin wave wavelength is around 15 nm when the skyrmion size is more than 20 nm in varying magnetic track width.[89]

1.7.5 Force Model with only Force from the edge, Reflected and Transmitted Spin Wave

When the distance between the skyrmion and sample edge is a few times larger than l_{edge}, as is the case initially, $\mathbf{f}_{\mathrm{edge}}$ is negligible, and the forces on the skyrmion and the resultant skyrmion velocity are as shown in Fig. 1.5(a). Firstly, we consider the case where the spin waves are reflected by the skyrmion but not stronger than the transmitted spin waves, and the transmitted spin waves exert spin-transfer torque upon it [90]. Part of the torque's effect can be regarded as a longitudinal force $f_{\mathrm{transmit}\parallel}$ from transmitted SWs on the skyrmion particle, which yields retrograde motion of the skyrmion by reference to Eq. (1.19), as shown in Fig. 1.5(a). There is, in addition, a transverse force component $f_{\mathrm{transmit}\perp}$, meaning that the retrograde motion is not exactly back along the track towards the SW source, but at an angle.

On the other hand, when the strong reflection of the spin waves from the domain wall at the edge of the skyrmion is taken into account, an additional longitudinal force arises owing to the linear momentum transfer from the reflected magnons [20].

Suppose it exceeds the force arising from the STT. In that case, it will be strong enough to change the sign of the net longitudinal component of the force on the skyrmion and so change the skyrmion velocity to be positive along the x-axis.

Another possible mechanism to obtain forward motion is to consider the perpendicular force from the edge, the transverse component of which can give skyrmion forward motion, as shown in Fig. 1.5(b). Such edge-induced torques can be very large [91].

1.8 The Heat Gradient Driven Skyrmion

To generate a proper frequency spin wave, the distance between the antennas is one of the factors that will affect the wave vector, which means a series of chips with different distances antennas need to be fabricated. Compared to a spin wave antenna fabrication, a heater is easier to build because it just needs to be a large resistor with a small volume. Also, the raised temperature of a resistor is convenient to be measured by a four-point transport measurement.

In general, researchers suggest two different principles that will drive the magnetic patterns. One is the change in the entropy of the magnetic sample generated by the heat gradient. Another way is the magnonic current from the Seebeck effect.

1.8.1 The Entropy Difference Between Domain Wall and Domain

The magnetic pattern of the magnetic sample is stable with a particular external field and temperature. Domains and domain walls sit around the minimum energy state when the system stays or tries to reach its thermal equilibrium state at a finite temperature. People always suggest that the magnons generated by the temperature contribute to the entropy and free energy of the system.

In the second law of thermodynamics, the system prefers moving to the state with a lower free energy or forwarding to the state with a larger entropy. For example, all the atom's diffusion is because the system tends to be in a state with maximum entropy. So, the domain or domain wall should also obey this law. In Wang's paper [92], they set up a magnetic track with a head-to-head domain wall on it. The free energy of a region of a domain and domain wall was calculated. The motion of domains and domain walls is influenced by the difference in free energy between regions containing

domains and those with domain walls, rather than solely by the energy of the domain wall itself. A domain wall tends towards a state with a smaller free energy difference between the domain and the domain wall. Their free energy difference decreases with high temperature. Also, the entropy density difference increases when the temperature is high. Obeying the law, the domain wall will tend to move to the region where the free energy difference is smaller, which means the domain wall will move towards the hotter region.

The difference of the system free energy with different temperatures can be regarded as a magnetic field,

$$H_{\nabla \mathrm{T}} = \frac{\Delta S \nabla T}{2\mu_0 M_\mathrm{s}}, \tag{1.25}$$

where the S is the density of the entropy, and ∇T is the thermal gradient.

By using the Walker formula $v = \gamma H \Delta / \alpha$ [93, 94], the domain wall velocity driven by the equivalent field $H_{\nabla \mathrm{T}}$ is:

$$v_{\mathrm{DW}\nabla \mathrm{T}} = \gamma \frac{H_{\nabla \mathrm{T}} \Delta}{\alpha}, \tag{1.26}$$

where α is the damping constant, Δ is the domain wall width. In Eq. 1.26, the domain wall velocity is proportional to the ∇T. The larger temperature gradient can generate a larger free energy difference and entropy, which will generate a larger domain wall velocity towards the hotter region. The magnons flow from the hot region to the cold region generated by the heat gradient is compensated by the magnons in the bound states when calculating the free energy.

1.8.2 The Seebeck effect, spin Seebeck effect and spin-dependent Seebeck effect

The Seebeck effect, Spin Seebeck effect, and spin-dependent Seebeck effect are different contents of the thermoelectric phenomena. The Seebeck effect is a well-known thermoelectric phenomenon; a thermal gradient on the different materials can generate different electric voltage in a loop. The different thermal responses of the distribution of charge carriers between different materials cause the electric potential. [95] Meanwhile, the Spin Seebeck effect is a phenomenon from magnetic material. A thermal gradient on the different magnetic materials can generate different spin potentials.

When the spin transport is based on the spin-polarized conduction electrons, the phenomenon will be called spin-dependent Seebeck effect.[96, 97] Due to the spin-up

and spin-down electrons having different scattering rates and densities. The different properties of the spins and electrons make the different materials have different spin Seebeck coefficients.

For regular conducting metal material with a thermal gradient, the electrons will accumulate at different ends of the sample, which generate an electric voltage along the direction of the thermal gradient. For conducting ferromagnetic material[98, 99], the spin-up and spin-down electrons will accumulate and generate a spin voltage, so the Seebeck effect for a conducting ferromagnetic is called the spin-dependent Seebeck effect.

At the thermal equilibrium state, the charge current in an open circuit is zero, so there will not be a net charge flow of electric charge

$$j_c = 0 = j_\uparrow + j_\downarrow, \tag{1.27}$$

where $j_\uparrow$ and $j_\downarrow$ are the spin up current and spin down current. Meanwhile, the spin current is $j_s = j_\uparrow - j_\downarrow$.

$\sigma_\uparrow$ and $\sigma_\downarrow$ are the spin current conductivity for spin up and spin down electrons, respectively. Here, the spin Seebeck effect coefficient $O = \frac{\sigma_\uparrow O_\uparrow - \sigma_\downarrow O_\downarrow}{\sigma_\uparrow - \sigma_\downarrow}$ with the spin current $J_s = -(\sigma_\uparrow - \sigma_\downarrow) O \nabla T$.[56]

The spin Seebeck effect can even be present on an insulating magnetic material.[100] The spin Seebeck effect directly generates the spin potential by the thermal gradient on the magnetic insulator. The phenomena prove that the spin Seebeck effect can be generated on the magnetic material without the electron carriers. The spin current from the insulating magnetic material spin Seebeck effect, the spin current can be regarded as a pure magnonic current with angular momentum due to the abscent of the charge carrier, so this phenomenon is also called magnonic Seebeck effect.

1.8.3 The Spin transfer torque between magnons and domain wall

The ferromagnetic material used in this project is $Co_{68}B_{32}$, an electrically conducting alloy. Though the pure spin current is carried by charged particles when applying a thermal gradient on $Co_{68}B_{32}$, the spin current is usually regarded as a flow of pure angular momentum and there is no charge current because the system is in the open circuit. The quasi-particle magnons also possess angular momentum, so the magnonic current in the mathematical model can represent the spin current carried by charged

particles. Since the spin current will flow from the hot region to the cold region because of the spin Seebeck effect, the magnons can be regarded as flowing from the hotter region to the colder region because of the diffusion and present a magnonic current as well. With the presence of the pure magnonic spin current model, the spin transfer torque can explain the domain wall motion driven by the pure spin current on both conducting and insulating materials.[101–103]

Similar to the transmitted spin wave driven skyrmion model as mentioned in §1.7.3, if the magnons are fully transmitted across the domain wall, it will transfer $2\hbar$ of angular momentum, and the torque will drag the domain wall upstream towards the source of the magnonic current. Because the magnonic current generated by the thermal gradient will flow to the colder region, the transmitted magnons exert an STT on the domain wall, leading to the domain wall moving toward the hotter region. To completely absorb the spin transfer torque from the magnons, the domain wall needs to propagate with speed $\frac{-\rho^2 v_g}{2}$. Because $J_s = -A\rho^2 q$, the velocity of domains becomes $\frac{J_s}{2Aq} v_g$ and towards the hotter region.

Another way to estimate the domain wall motion is to use the LLG equation and calculate the magnetisation dynamic. The LLG equation can always describe the magnetic domains. By substituting the Walker ansatz into the Landau-Lifshitz-Gilbert equation Eq.1.1 and regarding the spin current as magnonic current:

$$M_s = -\gamma \mathbf{M} \times \mathbf{H}_{\text{eff}} + \alpha \frac{\mathbf{M}}{M_s} \times \frac{d\mathbf{M}}{dt} + \gamma \hbar J_s \left(\frac{\partial \mathbf{M}}{\partial x} - \beta \frac{\mathbf{M}}{M_s} \times \frac{\partial \mathbf{M}}{\partial x} \right), \tag{1.28}$$

where the J_s is the magnon current from the Seebeck effect, the β term is disspative correction term from the weak charge-current-indeced spin transfer. After derivation from Kovalev's published paper, $J_s = -\frac{k_B \nabla T}{6\pi^2 \lambda \alpha \hbar}$ [57, 104]. The ∇T term indicates the thermal gradient on the x-axis, showing that the current J_s is proportional to the heat gradient. The larger the heat gradient, the stronger the magnon current flow from the hot region to the cold region since the J_s is negative.

In conclusion, the tendency of the domain wall motion driven by spin transfer torque is the same as the analysis in the aspect of system entropy and free energy. Because of the SiO_x layer between the heater and magnetic layer, the exact thermal gradient is unmeasurable, and the precise domain wall motion can not be calculated. We can only discuss the domain displacement as proportional to the heat generated by the heat gradient, which will be discussed in Chapter 7.

Chapter 2

Methods

2.1 Introduction

This chapter will review the principles of the research methods I used. The overall aim of the project was to study the motion of skyrmion on a ferromagnetic track by both simulation and experiment. Different deposition methods were used to fabricate sheet film samples and patterned magnetic tracks to gain the asymmetric interaction (DMI interaction) from the interface between the heavy metal and magnetic layer. The magnetic material $Co_{68}B_{32}$ is used as the ferromagnetic layer. The properties of samples need to be determined. Multiple characterisation methods were used for the thin magnetic samples. XRR was used to find the thickness of each layer. Magneto-optic Kerr effect (MOKE) for the coercive field and the magnetic anisotropy orientation of samples. In order to quantitatively calculate the sample magnetic properties, the superconducting quantum interference device (SQUID) measurements with varying fields and temperatures were done. Kerr microscope helps image the domain bubble expansion or the size of maze domains to calculate sample DMI values. The magnetic properties are used in the micromagnetic simulation. The simulation software used for micromagnetic simulation is OOMMF [71].

In order to measure the skyrmion motion driven by the heat gradient, the narrow magnetic track and circuit connection for the heater that creates heat gradient need to be built and suitable for a unique sample holder under the Magnetic Force Microscopy (MFM) head. The sample fabrications for chip samples on the PCB were in the clean room by maskless alignment lithography equipment. The recipe of chemical solutions for electron beam lithography in the clean room is the same for the condensed matter physics group users and will be mentioned in the following section. The cryostat with a lock-in amplifier measured the resistances of different patterns under varying temperatures. Transport measurement for the insulator layer was done to avoid the current leaking when applying current on the Pt heater pattern. The magnetic domains or skyrmions are then imaged by MFM.

2.2 Sample preparation

2.2.1 Physical Vapour Deposition (PVD)

There are multiple ways to achieve the thin film coating on a single side polished Si wafer substrate. The PVD methods used for the project are DC magnetron sputtering, RF magnetron sputtering in the cleanroom and thermal evaporation. We used the DC sputtering to make the magnetic multilayer, the RF sputtering for the SiO_x layer and evaporation for contact leads of the chip.

The PVD equipment used for depositing metal material outside of the cleanroom during this project is a DC magnetron sputtering equipment named IVOR, built by the condensed matter physics group. The principle of the DC sputtering is shown in Fig. 2.1(a). The argon gas will be ionised to argon ions and electrons in the low gas pressure environment. The target acts as the cathode. The chamber and the traget sheilds are grounded and act as the anode. During the sputtering process, the bias field from the power resource and the magnetron will let the ions collide on the target and create a spray of the target atoms to the substrate. To trap electrons near the target surface, magnet ia placed under the target. The strongest magnetic lines form a closed racetrack near the surface of the target. The ionization of the Ar gas will be most intense along the racetrack. The appeared racetrack might cause non-uniform deposition and needs to be took care over time. The racetrack is a phenomenon associated with the magnetic field configuration used in magnetron sputtering systems to trap electrons near the target surface

The magnets located near the target surface are designed to confine the electrons in the plasma, enhancing the argon plasma density. The higher density of the plasma leads to higher sputtering rates and a more uniform deposition rate across the sample surface.

The IVOR equipment is shown schematically in Fig. 2.1(b). As a 'homemade' DC magnetron sputtering system, the IVOR chamber contains the liquid nitrogen Meissner trap to help reduce the water vapour from the air. Reducing the water can reduce the risk of a reaction between water and certain materials or special substrates such as titanium, aluminium and ITO [105–107]. Water also contains reactive oxygen, especially when cracked in a plasma, and so can lead to impure films [108]. The condensed water might lead to a rough surface while sputtering and affect the sample

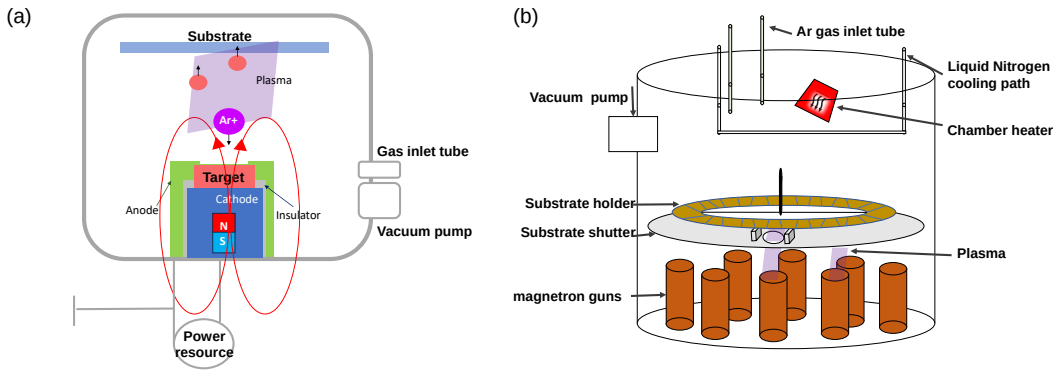

Figure 2.1: The schematic drawing of (a) DC Sputtering and (b) the structure of the IVOR chamber.

surface roughness and uniformity.

Compared to the PVD system without toroidal magnetrons, the magnetrons create a toroidal field to confine the plasma in a ring closely over the target. It also concentrates the plasma through the hole of the shutter and allows the higher density target atoms to spray on the substrate upon the hole with less arcing problem [109]. The holder wheel and sample wheel design allow the plasma of different guns to stay lit; the different materials and thickness of layers will grow on the substrate with stable sputtering speed. The heater in Fig. 2.1 (b) is not for sample heating. Before opening the chamber after sputtering, we need to wait until the chamber is back at room temperature, the heater will be used to reduce the waiting time.

Regarding RF sputtering, the principle is similar, but the sputtering power for RF sputtering will be replaced by the RF power to generate an electric field when the target is an insulator.

The RF sputtering process was on the PVD 75 from the Kurt J. Lesker Company. The schematic structure of the PVD 75 RF sputtering chamber is shown in Fig. 2.2. The system has a vacuum chamber and gas inlet system, allowing different gases to flow in the chamber during the deposition. The source holders have different power supplies; the radio-frequency (RF) power supply is designed to process non-conductive dielectric sources such as SiO_x. Compared to the DC sputtering, the Ar is ionised to energetic ions by the RF source. A matching network, including a blocking capacitor and inductor, can be adjusted to give impedance matching at the operating frequency of 13.56 MHz, shown in Fig. 2.2. The target material will be set up as the

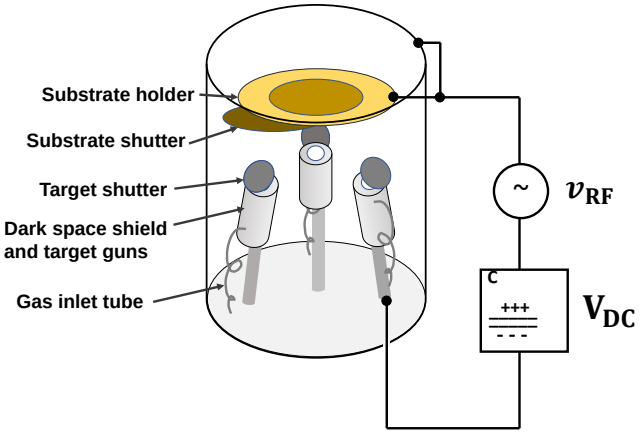

Figure 2.2: The structure of PVD 75 chamber with matching network and RF sputtering setting

negative cathode and the target shield as an anode, respectively. The Ar+ will be accelerated to the target, and the collision will eject an atom from the surface of the target material. The target surface is bombarded by the Ar ions, ejecting the target species; the target atoms will finally deposit on and cover the substrate. The Ar+ ions accumulate on the cathode target surface will cancel the negative potential of the target and discharge the target atom for coating, which means the sputtering would stop for a dc process. The RF power supply can alternate the potential of the target and substrate. The condensed positive ions will be removed, and the electrons from Ar gas ionisation take place the role to collide with the target and neutralise the target. The accumulation of ionised ions will raise the possibility of arcing. The discharge will lead to an unstable target atom spray and produce a non-uniform coating. So, the frequency of the RF supply is an important setting property to create a smooth thin film. The continuous discharge achieved by the positive and negative cycle of RF power over 1 MHz will allow continuous and stable sputtering. The frequency of the RF supply for the insulating target is fixed at 13.56 MHz, which is also the standard frequency for all RF sputtering equipment, which can be found in the major components sheet of KJLC RF03 Power Supply for PVD 75 [110].

The principle of thermal evaporation is simpler. A high current will heat a resistive heater, and the target inside the crucible will be evaporated. The evaporated targets will form a vapour plume above the evaporator source and be deposited on the substrate placed upon the target. The chamber structure of the thermal evaporator in the

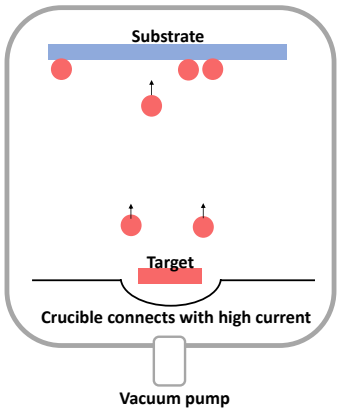

Figure 2.3: The schematic drawing of the thermal evaporation

cleanroom in Fig 2.3 looks like its principal schematic drawing but with an extra growth rate monitor installed to determine the thickness of the layer on the substrate and when to close the cap upon the crucible. The growth rate monitor can also display the estimated thickness of the material on the substrate. A shutter upon the crucible was used to stop the plume from reaching the substrate when the expected thickness of the material was gained. Because the growth rate is more than 10 angstrom per second for Ti and Au, which is much higher than that of DC sputtering, we used the thermal evaporator to grow 100 nm thick contact leads.

2.2.2 Photolithography and Maskless Lithography Aligner (MLA)

The normal sputtering process can provide multilayer sheet film samples, but to build lateral patterns on a wafer, photolithography is one of the main methods [111]. A photoresist is a necessary tool for lithography. It is a kind of light-sensitive material. Its changes in chemical properties after exposure to UV light allow it to be used for patterning. There are two kinds of photoresist. The exposed negative photoresist will remain on the substrate after exposure and development. The unexposed negative resist will be rinsed with deionised (DI) water. The exposed positive photoresist will be removed by DI water rincing after exposure and developing. The unexposed positive resist will react with the developer and remain on the substrate.

In this project, we used the positive photoresists from the S18 and LOR B series for exposure, developed with different concentrations of MF351 developer and developing

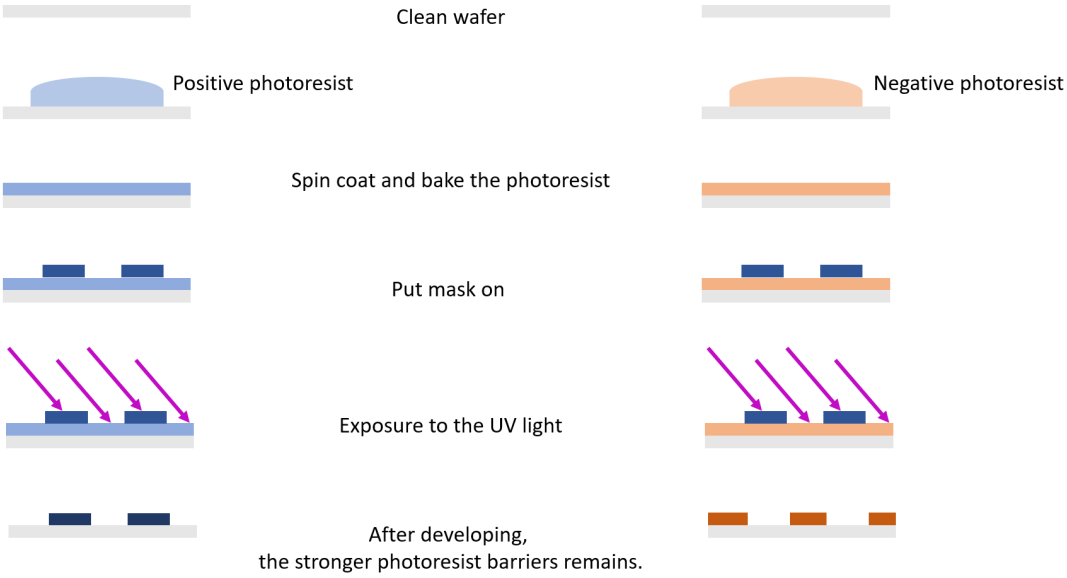

Figure 2.4: Process flow of positive (blue) and negative (orange) photoresist photolithography method

time. SVC14 is the positive photoresist stripper we used to lift off the layer built by deposition. The principle to build the photoresist barrier is presented in Fig. 2.4. The UV light will weaken the positive photoresist and create the same pattern as the mask. On the contrary, the negative photoresist will be strengthened and leave a reverse mask pattern. Since the photoresists we used were positive, the pattern we wanted to remain in the area that had the UV light exposure. The KLayout software [112] is a software that can design the pattern. The pattern drawn in the software is the pattern will remain. The design will be shown in §6.2.

By applying the material layer upon or under the photoresist, the remaining resist can be used as a barrier or etching cover, as shown in Fig. 2.5. The process flow on the left-hand side is the etching process; for the isotropic etchant, the undercut under the photoresist cover will appear. For example, to etch the SiO_2, hydrofluoric acid can be use to have uniformlly material removal.[113] Using the anisotropic etchant can reduce the undercut. For example, reactive ion etching uses ions and radicals generated in a plasma to etch materials selectively.[114] The right-hand-side process flow is the lift-off process; the photoresist stripper will remove the developed photoresist barriers and leave behind the reverse pattern on the material layer. However, fencing and crowning

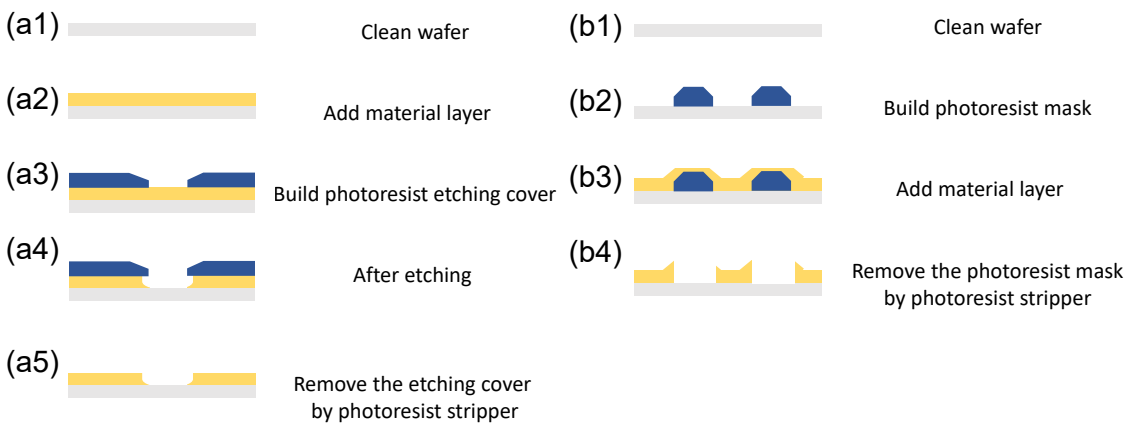

Figure 2.5: Process flow of (a1-a5) the etching and (b1-b4) the lift-off. The crowning and fencing are shown in (b3-b4).

issues are significant when using the single-layer photoresist [115, 116]. The fencing is due to the non-uniform deposited layer, which has more material accumulated around the edges of the developed photoresist patterns. This coverage will cause a blockage between the photoresist and its stripper like a 'fence', which will cause a complete lift-off, incomplete patterning or low resolution. The crowning is related to the top part of the photoresist; when the top part gets more development than the bottom part, the pattern edge will lift more or have an upward curve like the last step result of the lift-off process shown in Fig. 2.5. The crowning of the edge of the remaining material will affect the coverage and thickness of the next layer

Double photoresist coating can significantly reduce the crowning at the edges of the remaining pattern by having an undercut of the developed photoresist pattern [115] . The undercut from the bilayer photoresist layers are based on the different developing speed of the top and bottom layer; the slower developing speed of the top layer avoids the top layer shrinking more than the bottom layer, as shown in Fig. 2.6. The deposition of the material layer will be unidirectional with the bilayer photoresist barriers. In this case, step coverage is another important property that needs to be considered. The poor coverage will lead to the current leaking between layers or discontinuous of the patterns. For the evaporation layer, the atoms are directed in a straight line by heating up. For the sputtering layer, the atoms are scattered in all directions. With the undercut of the bilayered photoresist pattern, thermal evaporation can offer better

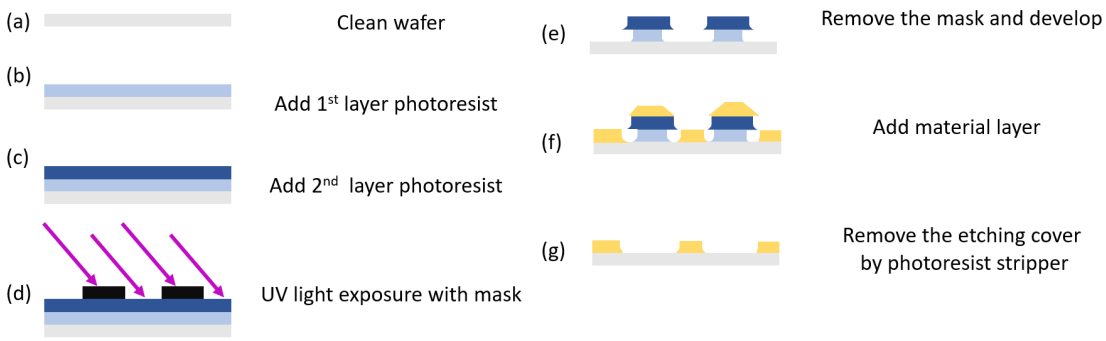

Figure 2.6: The process flow can create proper undercut resist and material pattern with less crowning.

step coverage than single-layer photoresist. The advantage of the evaporator in step coverage is more significant than the sputtering because of the more directional flux of atoms.

The substrates were cleaned in an ultrasonic bath for 2 minutes using acetone, IPA, and then water. The nitrogen gun was used to dry the liquid remaining on the substrates. The photoresists S1803 and LOR 3B were taken out from the refrigerator and warmed back to room temperature. To reduce the uncoated area or inhomogeneities in the resist film, we should avoid bubbles when applying the photoresist on the substrate and avoid taking the photoresist from the bottom of the bottle that might contain clots or particles. Disposable pipettes can also reduce the particles on the substrate after cleaning the substrate. The spinner was used to apply the photoresist on the substrate. The substrate got a spin coating of the first layer of the photoresist LOR 3B with a spin speed of 3000 RMP. The substrate with LOR 3B was then placed on the 185 °C hot plate for 3 minutes of baking. The second layer, S1803, was applied after cooling the substrate for at least 1 minute after baking. The spin speed was still 3000 rmp for S1813, the baking temperature changed to 115 °C, and the time length changed to 1 minute.

The energy and defocus of the laser for different photoresists and solutions also affect the exposure and developing result of the photoresist. To gain the pattern with designed details, different series of combinations of laser energy named 'Dose energy' in the software and 'Defocus' were tested, as shown in the §6.3. The developing time and developer solutions will affect the thickness of the remaining photoresist, which

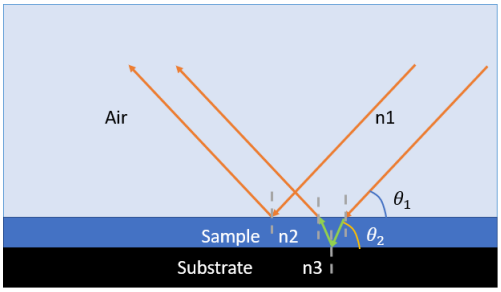

Figure 2.7: X-rays reflection from the air/sample and from the sample/substrate interfaces

should be removed and create different widths of the undercut.

2.3 Sample Characterization Techniques

2.3.1 X-ray Reflectometry (XRR)

X-ray reflectometry (XRR) was used to find out the thickness details of the samples.

In Snell's law, $n_1 \cos\theta_1 = n_2 \cos\theta_2$. The n_1 and n_2 are the refractive indicies of the materials, θ_1 and θ_2 are the angles between the light path and the plane of the materials as shown in Fig. 2.7. The light path is dependent on the refractive indices of the materials involved when transferring from one material to another. The refractive index is $n = 1 - \delta + i\iota$, where δ is the real part of the refractive index and ι imaginary part of the refractive index. δ corresponds to the phase shift of the X-rays as they penetrate the material, ι corresponds to absorption within the material. The X-ray refractive index of a material will slightly smaller than 1. So we will have total external reflection and the critical angle $\theta_c = \arccos\left(\sqrt{1-\delta_2}\right)$. The incident angle of the X-ray will affect the reflection of the X-ray. If the incident angle equal to θ_1 is smaller than the total reflection critical angle θ_c, all incident X-rays will be reflected. The critical angle showed in the Fig. 2.8 is around 1.2°.

If the X-ray is incident from the air to the metal with θ_1 larger than the θ_c, the X-ray will not experience total reflection at any angle. Because the X-ray wavelength is 1.54 angstrom, with a low angle difference, the thin layer thickness in the atom scale can be measured. The interference between the X-rays reflected from the top and bottom interfaces of a thin film on a substrate leads to the appearance of fringes or oscillations

in the X-ray intensity as the sample angle is varied. The principle of the XRR can be based on the Bragg equation $n\lambda = 2d\sin\theta$, where d is the distance between lattice layers and θ is the x-ray injected angle. Even if the material is noncrystalline, the x-ray will be completely reflected at a low angle because the difference in refractive index between air (n_1), solid sample(n_2) and substrate(n_3), which is shown in Fig. 2.7. Once the path $2d\sin\theta n_2$ difference between the two reflected X-rays from the top and bottom interfaces is an integer k times the X-ray wavelength, the interference will occur, and the X-ray intensity will show fringes. These fringes were first observed by Kiessig in 1931 [117]. The distance between the fringes represents the thickness of the film; the larger the distance, the thinner the film on the substrate. Including a correction for dynamical effects (refraction), the modified Bragg equation can be used to calculate the thickness of the sample. Using the maximum of the fringes, θ_i is the position of the maximum of the i_{th} fringe, n_i is the index of the observed Kiessig fringe maxima, $\Delta n = 0.5$ for maximum of the fringes and λ is the wavelength of the X-ray:

$$\sin{\theta_i}^2 = {\theta_c}^2 + \frac{(n_i + \Delta n)^2\lambda^2}{4d^2} \tag{2.1}$$

[118],

with the kinematical approximation, the thickness of the layer can be extracted from the Kiessig fringes. The kinematical approximation needs the low incident angle to be far away from the θ_c so that the dynamical effects can be ignored. The thickness of the layer t_{kf} is regarded as the d in Bragg's equation, the half of the angle between adjacent Kiessig fringes θ_{kf} is regarded as the θ. By applying the wavelength of X-ray to Bragg's equation, the thickness of layer $t_k = \frac{\lambda}{2\sin\theta_{kf}}$. For example, the θ in Fig. 2.8 is around 0.12° so we have thickness of Ta/[Pt/$Co_{68}B_{32}$/Ir]$_{20}$ sample around 36.8 nm.

These fringes can also contain information on the periodic multi-stack structures. The Laue oscillations will appear from incomplete destructive interference when the sample contains a periodic structure. The Laue oscillation acts as a high peak between smaller Kiessig fringes on XRR data, as shown in Fig. 2.8. The half of the angle between Laue oscillation peaks θ_{lo} can also be applied to the Bragg's equation to calculate the thickness of the periodic structure [119].

Then, the thicknesses of individual layers in the multilayer structure can be determined by analysing the interference fringes from all the layers. The thickness information can be manually calculated from the period of Kiessig fringes but is still not accurate, especially if the fringes are affected by the noise. The roughness of the

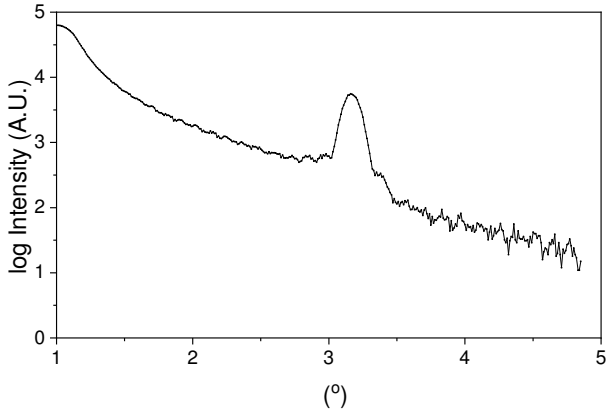

Figure 2.8: X-rays reflection data of 20 times periodic [Pt/CoB/Ir] sample. The critical angle is around 1.2°. A lot of small Kiessig fringes on between 1.5° to 3°, a Laue oscillation is at around 3.2°.

interface can also show in the fringes; the rougher sample will have dampened fringe amplitude.

GenX is a program designed by Andreas Viklund and developed by Matts Björck and Ivana Zizak that can simulate the XRR data of the set-up structure and fit with the experimental XRR data [120, 121]. After loading the experimental XRR data, the user manually set up a sample structure, and each layer's materials and estimated thickness roughness were set. The simulation's first step was done by calculating the provided information. The user can then set up the adjustable ranges of all the parameters for the fitting. The fitting involved iterative optimisation techniques to find the best-fit model that matches the experimental data. The default figure of merit (FOM) of GenX is the reduced chi-square statistic. A smaller FOM indicates a better fit. GenX filtered the changing parameter that led to a limited increase in the FOM to minimise the figure of merit.

2.3.2 Magneto-Optic Kerr Effect (MOKE)

To characterise the basic magnetic properties of samples, the magneto-optic Kerr effect (MOKE) was used to gain the hysteresis loop of magnetic samples. The interaction between the light and the magnetic moments in the material will change the polarised light angle. The changed polarisation angle is the Kerr rotation angle. The Kerr

rotation angle depends on the sample's magnetisation, so after passing through the fixed polarising film, the detector will detect different intensities of horizontal and vertical components when the sample is at different states. The varying reflected polarised light from the samples will be detected with various external magnetic fields. The varying intensity of the reflected polarised light through the polariser filter can be transferred to the normalised magnetic moment on the hysteresis loop.

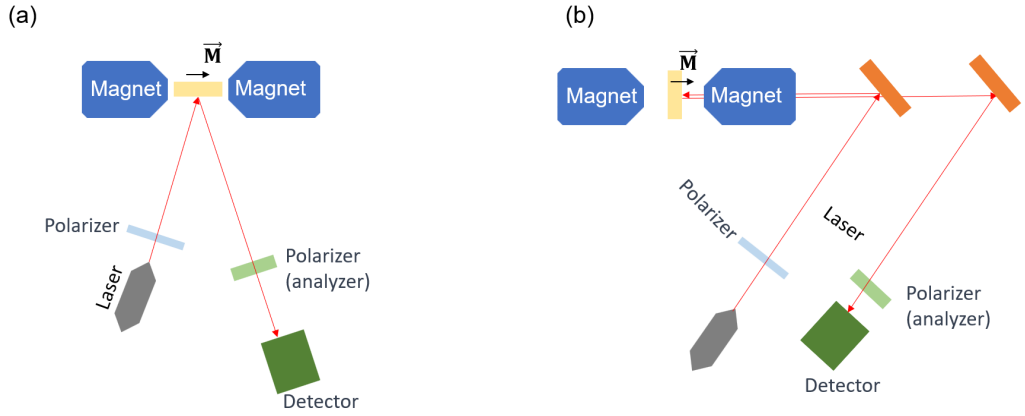

Figure 2.9: The basic optical experiment set up of (a) longitudinal MOKE and (b) polar MOKE.

The MOKE equipment contains four main parts, which are shown in Fig. 2.9, incident laser light path, reflect light path with set up polarising film and light detector, the sample holder and electromagnets.

In longitudinal MOKE, the orientation of the external magnetic field is parallel to the sample plane and lies in the plane of reflection. The p-polarised laser is used. The linear polarised light will then be incident on the in-plane magnetised sample. The reflected light will pass another polariser, also called an analyser. This analyser is used to analyse the polarisation angle of the reflected light. Photodiodes are a type of semiconductor-based photodetector which can transfer light intensity into an electric signal. By fixing the analyser angle and measuring the intensity of the passed light, the Kerr rotation angle can be detected.

In polar MOKE, the orientation of the external magnetic field is perpendicular to the sample plane. Though circularly polarised light are normally used, the linear polarised light was still used in our experiment. The same optics were used as the

longitudinal light.

2.3.3 Kerr microscope

The Kerr effect microscope is a technique to take images of the magnetisation or demagnetisation pattern of the sample.

The principle of the Kerr microscope is the same as the MOKE, but it can obtain images by capturing the sample surface and measuring the intensity of the reflected light for different positions and polarisation analyser angles. These images can show the magnetisation pattern of the sample surface in a greyscale.

The Kerr microscopy principle is based on the polarised angle rotation of the reflected polarised light. The magnetic sample is made of birefringent materials. The different refraction index is due to the anisotropy of the sample. Kerr contrast is a parameter to describe the contrast of the Kerr signal to domains with different magnetisation directions. Different types of polarised light will give different Kerr contrast to samples with different magnetic easy axes. As shown in Fig. 2.10, different polarised lasers will have different contrasts between the +z and -z axis magnetisation domain. If the +z and -z magnetisation domains are all shown in the same colour, the contrast of the OOP domains is not high enough.

The Kerr microscope needs to contain a light source, polarising optics, electromagnet, analyser and camera to show the magnetic textures of the sample. The polarising optics were used to provide polarised light to be reflected on the sample surface. The optics can switch to the conoscopic mode. The conoscopic mode is to exam birefringent materials which can produce interference figure of two different polarised light split by the materials. The built-in Bertrand lens lets the user observe the formation of isogyres (the dark bands in the conoscopic interference pattern) arising from the superposition of reflected polarised light from the sample. Since the polarisation state of the reflected light might change differently depending on the optical path, there's a spatial variation of the polarisation state in the conoscopic mode back focal plane.

After setting the magnets to provide the external field and the lens focusing on the sample surface, the polariser and the aperture slit need to be adjusted to give us polarised light and the needed Kerr contrast. The aperture slit is the spatial filter to select the specific angular components of the light. The adjustment was made in conoscopic mode. In the conoscopic mode, a specific optical configuration as compensator

and analyser (i.e. a quarter-wave plate) will be in the optical path. This special optical configuration will split the incident laser into two orthogonally polarised lights. The interference between the two reflected orthogonally polarised beams of light after their interaction with the sample creates the dark cross pattern as shown in Fig. 2.10 (a) below.

The dark cross needs to be significant by adjusting both the compensator and analyser if the cross is not well defined in the monoscopic image because the orientations of the magnetisation component parallel to the reflected lights will gain the highest Kerr contrast [122, 123]. Then the aperture slit needs to be adjusted to open a square window, which size and position should be similar to the green square in Fig. 2.10(b) to have pure polar sensitivity. In pure polar sensitivity, the incident laser is perpendicular to the sample surface, and the magnetisation component in two different directions parallel to the incident light will gain the highest contrast. If the aperture (green rectangles) was adjusted to open the window like the green rectangle in Fig. 2.10(c) or (d), the transverse Kerr effect with the orientation parallel to the incident lights vertical plane (or transverse sensitivity) will be set up in high sensitivity. Meanwhile, the contrast of different directions of the magnetisation component in out-of-plane direction will lose some contrast.

The magnetic textures obtained from the Kerr microscope are useful to calculate the D_{DMI}. Calculating the DMI of the sample has some methods, but most of them are based on the domain pattern of the samples. The sample prepared in this project contains repeated stacks. The domain pattern of those samples with a repeat number n larger than 2 will be like a maze rather than simple nucleated domains. The domain periodicity methods will be used to calculate D_{DMI}. These two methods will be discussed in §3.0.3 and §3.0.4.

2.3.4 Atomic Force Microscopy (AFM)

The Atomic Force Microscopy is based on the interaction between the sample surface and the AFM tip. The interaction strength can represent such as the sample phase difference between solid and liquid, the molecular fine topographical features on the substrate or the larger-scale roughness of the sample surface.

The set-up of the AFM device from Asylum company contains an AFM scanning head, piezoelectric scanners platform under the head, feedback control system, optical

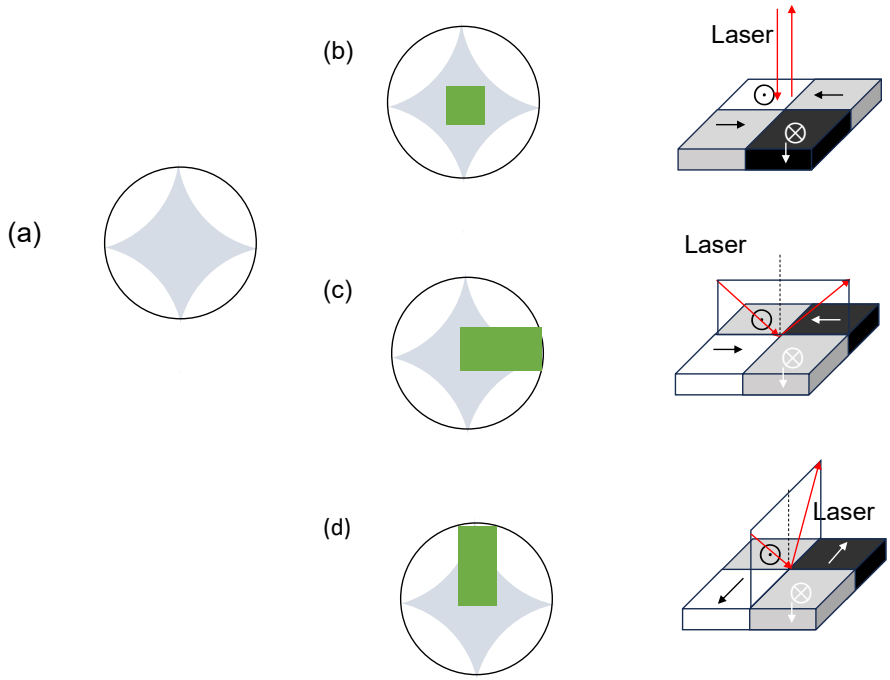

Figure 2.10: The aperture slit (green area) adjustment. (a)The cross needs to be set up after switching to the monoscopic mode, (b) the pure polar sensitivity Kerr effect aperture setting, (c, d) the transverse Kerr effect aperture setting.

system, computer and software as shown in Fig. 2.11. The cantilever and tip assembly will be loaded at the bottom to the AFM head as shown in the side view of the AFM head; the sharp tip needs to point to the sample surface. The AFM head also contains a photodetector system to gain the laser beam reflected by the tip, the deflection signal controller, the laser position adjustment system and the AFM head standing leg height adjustment system. The piezoelectric scanners are used to move the sample in two dimensions precisely; the scan size range is from 15 nm to 90 μm. The laser and light from the optical system will be captured by the camera so the user can align the laser position on the tip and locate the tip to the interested scanning area.

In the AFM, different types of scanning can be made. There are two typical modes: intermittent contact mode and contact mode, as shown in Fig. 2.12. In the contact mode, the tip makes continuous contact with the sample surface with a constant force defined by the user, so the red line in Fig. 2.12 (a) is aligned with the sample topographical shape. This mode is suitable for clean and hard samples; otherwise, the tip will change

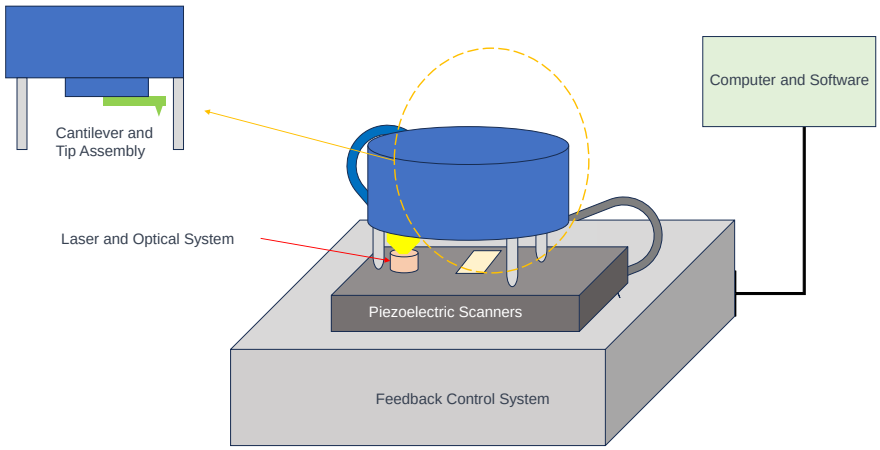

Figure 2.11: The scheme of the AFM equipment. The system contains AFM scanning head, piezoelectric scanners, feedback control system, optical system, computer and software.

the deformable sample or be destroyed by the 'lump' on the hard sample surface. In intermittent contact mode, the tip will continuously vibrate, relating to the 'drive amplitude' set up by the user, but touching the sample surface but not continuously. In Fig. 2.12 (b), only a few points of the zigzag tip track are on the sample surface. Because the tip will not scan through all the points of the scanning area on the surface, intermittent contact mode is more effective than contact mode. Also, the intermittent contact mode has less risk of friction that can wear out the tip and deform the sample, and it can measure soft material or samples with a large step height.

No matter whether the scanning modes need the vibration of the tip or not, the tip needs to be fine-tuned with the resonance frequency to check the stiffness and quality of the tip. If the tip is broken or contaminated, the resonance peak will shift and undistinct. Every tip has its own working resonance frequency; the feedback loop operates more effectively and is sensitive to the tip-sample interaction forces change when the tip vibrating frequency is closer to the resonance frequency. To ensure the reliable operation of the system and the reproducibility of the results, tip tuning is a critical step that needs to be done every time. The laser light is reflected off the back of the cantilever's reflective surface. The reflection angle changes as the cantilever deflects with the sample surface, so the reflected spot on the detector will change its

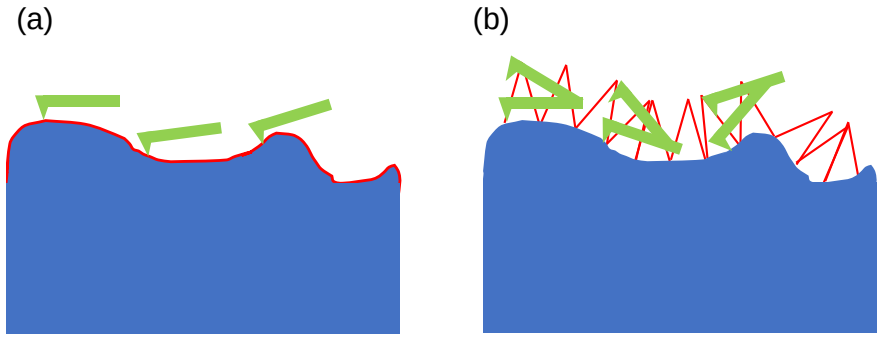

Figure 2.12: The tip track of (a) the contact mode and (b) the intermittent contact mode.

position. To tune the tip, firstly, the laser needs to be on the tip and closer to the end when the tip is away from the sample surface. Also, the tune will perform best when the cantilever is not bent, and most of the laser reflected from the cantilever is on the detector. For most of the manufacturers, the 'SUM signal' measures the total amount of spotlight on the detector. So, the 'SUM signal' of the system needs to be maximised. The 'Deflection' signal is from the photodetector detecting the deflection of the cantilever as it oscillates. When the cantilever is bent upward, the signal will be positive; when the cantilever is bent down, the signal will be negative. The mirror can adjust the 'Deflection' signal in the optical system and needs to be as close as 0 to maintain a balanced deflection.

The resonance peak should show when the measurement frequency range is close to the resonance frequency during tuning. The amplitude and frequency of the cantilever oscillation in imaging modes can be set up on the shown resonance peak. To reduce the effect of the tilted tip when the tip contacts the surface too hard, the tip oscillation frequency will be set slightly lower than the centre of the peak (position at around 90% of the peak maximum). The final step is adjusting the centre phase to maximise the signal difference when capturing the force.

After tuning the tip, we need to define the working distance between the tip and the sample surface in z-direction. The reflection laser intensity represents the equilibrium position for the cantilever when it's in contact. When the force between the tip and

sample is strong enough to affect the tip, the reflected and deflected laser intensity will change. Also, when the signal reaches the expected tip position and bending shape, it means the tip arrives at the sample surface.

For the equipment we used in this project, 'setpoint' is the name of the user-defined value of the expected strength of the signal when the cantilever contacts the surface. The smaller 'setpoint' is associated with harder contact because a smaller 'setpoint' means a less pronounced deflection when the cantilever is still close to its equilibrium position.

2.3.5 Magnetic Force Microscopy

The MFM was used to scan the sample surface to image the magnetic domains or skyrmions. The MFM scanning tips have a magnetic coating, so the magnetic interaction between the magnetic samples and tip will give information hidden in the phase shift wave we obtain. The tip will be raised later to extract the long-range magnetic force, and the interaction between the sample topographic surface and the tip can be reduced and even removed.

The intermittent contact mode mentioned in §2.3.4 is more common than the contact mode for MFM measurement because the intermittent contact mode will reduce the contribution of the AFM signal that might affect the MFM signal. Also, intermittent contact mode reduces the possibility of dragging the sample surface, which reduces the creation of defects on the sample and the alteration of domain structures.

When the tip starts intermittently contacting the sample, the rough sample provides van der Waals force information to the sharp tip. Since we can regard the tip-sample interaction as the interaction between a pair of atoms, we can use the Lennard-Jones model. The potential function of van der Waals force is $V_{\text{van}} = 4\epsilon[(\frac{\epsilon}{r})^{12} - (\frac{\epsilon}{r})^{6}]$, where the r is the distance between atoms, the ϵ is the depth of the potential well. Since the ϵ is the distance where both the potential energy and $\frac{\mathrm{d}V_{\text{van}}}{\mathrm{d}r}$ will be zero, ϵ is the equilibrium distance. The first term of the Lennard-Jones model represents the repulsive force between the atoms, while the second term represents the attractive force when two atoms are away from each other. [124] Because the van der Waals force was unwanted during the MFM measurement. The repulsive potential term is what we are concerned about.

Comparing to the power law for magnetostatics, $\mathbf{B}(\mathbf{r}) = \frac{\mu_0}{4\pi}\frac{3(\mathbf{m}\cdot\hat{r})\hat{r} - \mathbf{m}}{r^3}$, where $\mathbf{B}$ is the

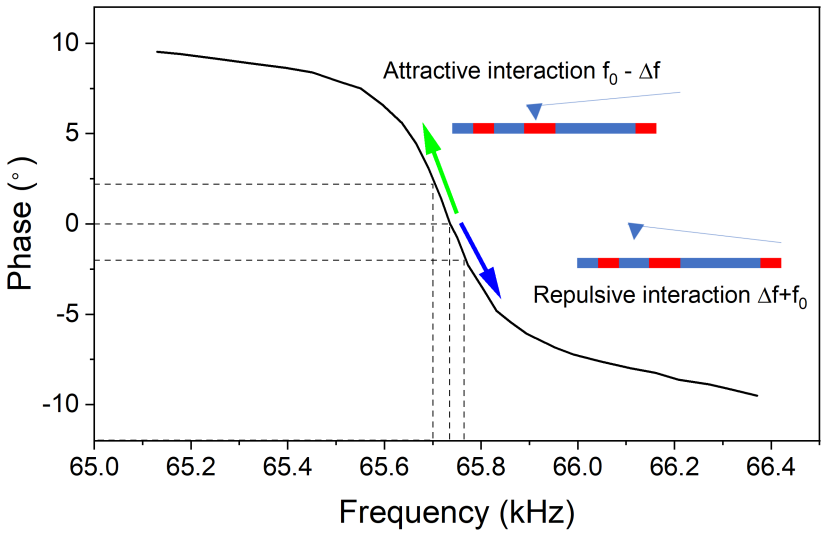

Figure 2.13: The phase value as a function of the resonance frequency. The Phase value will be set as 0 during the tuning.

magnetic field due to a point magnetic dipole moment $\mathbf{m}$ and $\hat{r}$ is the unit vector in the direction from the source to the observation point. The potential associated with the magnetostatics decays as $\frac{1}{r^2}$, compared to the $\frac{1}{r^6}$ of the attractive van der Waals potential term. So, in the second scan, the force due to magnetisation between the tip and sample can be obtained without the background of the van der Waals force. The magnetic domain picture can appear by removing the surface characterisation. The second scan is called lift mode. By interacting with the magnetic domains, the cantilever will bend or deflect. The frequency of the cantilever oscillation will increase when the cantilever gets repulsive force from the domains. On the contrary, the frequency will shift to a lower value when the domain attracts the cantilever. The frequency shift causes the amplitude or phase change of the reflected laser. The changes of the phase shift allow the user to observe the magnetic texture in the MFM phase channel. The frequency-dependent phase value is shown in Fig. 2.13. The two different MFM modes are shown in Fig. 2.14.

The interaction between the stray field from the sample and the magnetic tip gives rise to the MFM signal. The stray field from the MFM tip can interfere with the sample's magnetic domain structure and lead to distorted or erroneous measurements

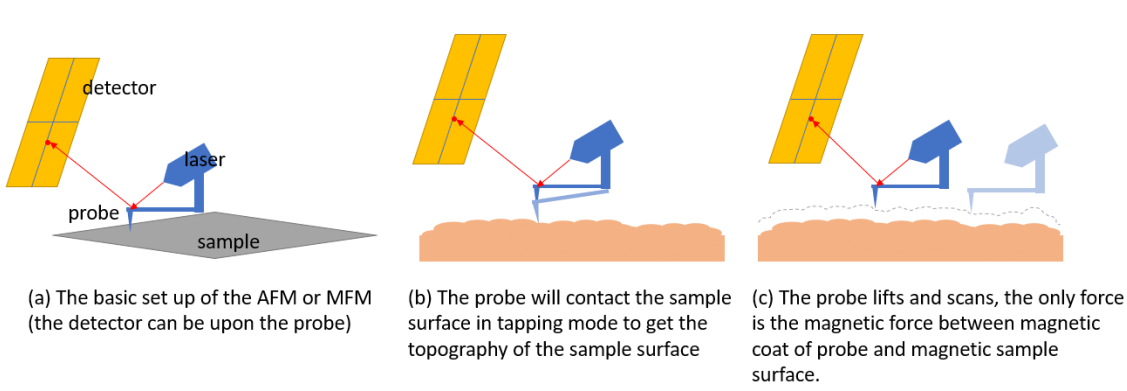

(a) The basic set up of the AFM or MFM (the detector can be upon the probe)

(b) The probe will contact the sample surface in tapping mode to get the topography of the sample surface

(c) The probe lifts and scans, the only force is the magnetic force between magnetic coat of probe and magnetic sample surface.

Figure 2.14: (a) The basic AFM or MFM measurement set-up. (b) The intermittent contact mode is the first AFM scan, and (c) the MFM parallel scan upon the sample surface.

[125]. The influence of the tip stray field remains negligible by using a sharp tip to minimise the tip's magnetic moment. The different coatings material on the silicon tips provide different magnetic moments. The MESP-LM-V2 tips from Bruker have Co-Cr coating, which provides low moment: 0.3×10^{-13} emu. The ASYLMFM-LC-R2 tips from Oxford Research have permalloy coating, which provides medium to low moment: 1×10^{-13} emu. A low moment tip is needed when we want to minimize disturbance from the magnetic tip to the magnetic structure of the sample. To optimise the MFM measurement, we need to choose an appropriate MFM tip with suitable magnetic properties and a proper scan lift height to minimise the tip-sample surface interactions and maximise the MFM signal-to-noise ratio. This will be discussed in more detail in Chapter 5.

2.3.6 SQUID-VSM

When a magnetised sample vibrates in a coil, the magnetic flux in the coils will change, and a magnetic induction voltage will be produced. The principle of the vibrating sample magnetometers (VSM) is Faraday's law of induction. It tells that induced electromotive force will be related to the vibration frequency and the change of the magnetic flux, $E = \frac{-d\Phi}{dt}$, Φ is the magnetic flux in a certain area.

The superconducting quantum interference device (SQUID) can detect the flux in the coils, which results in an AC voltage across the SQUID's Josephson junctions. As

shown in Fig. 2.15, two Josephson junctions connect in parallel. The current through point A will be two times the current through points B and C when there is no phase difference between two currents, $I_C = I_B$. The phase difference between point B and C is $\Phi_A - \Phi_D = \delta_b + \frac{2q_e}{\hbar}\int \mathbf{Ads} = \delta_c + \frac{2q_e}{\hbar}\int \mathbf{Ads}$ and $\delta_b - \delta_c = \frac{2q_e}{\hbar}\Phi$, where q_e is the charge of the electron, δ_a and δ_b are the additional phase differences of superconductors, **A** is the magnetic vector potential, $\int \mathbf{Ads}$ is an area integral of A.

So $I_C + I_B = I_0[\sin\left(\delta_0 + \frac{q_e}{\hbar\Phi}\right) + \sin\left(\delta_0 - \frac{q_e}{\hbar\Phi}\right)]$. The magnetic flux in a certain area Φ of a SQUID loop is proportional to the magnetic moment of the sample, $\Delta\Phi = \mu_0 M$. The interaction between the sample's magnetic moment and the external magnetic field leads to changes in the magnetic flux within the SQUID loop, which can be detected and measured by the SQUID. $\mathbf{M} = \frac{1}{\mu_0} V\mathbf{B}$, where **M** is the magnetic moment of a sample, **B** is the flux density inside the material, and V is the volume of the sample. The SQUID-VSM device will calculate the moment with its setting parameters, like the area of the coils, and directly give the *M*-*H* loop.

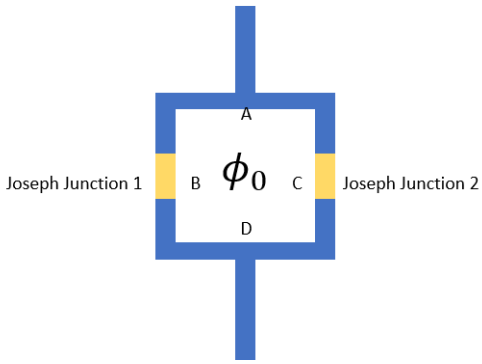

Figure 2.15: The DC SQUID and its two parallel connected Josephson junctions

The SQUID system of our group is from Quantum Design. It allows the temperature range from 1.8 K to 400 K and the external field from 0 to 70000 Oe. The magnetic field changing resolution: 0.33 Oe and the temperature accuracy is smaller than 0.5 K.[126] As shown in Fig. 2.16 (a), the system contains a computer control system, linear motor and SQUID sensor in the dewar. The superconducting magnet wound in a solenoidal configuration provides the external field [127]. The superconducting detection coil has four coils, the upper and bottom coils are single-turn wound clockwise, and the centre coil is two turns wound counter-clockwise. The detection coil is installed at the centre of the superconducting magnet. The gradiometer configuration of coils was

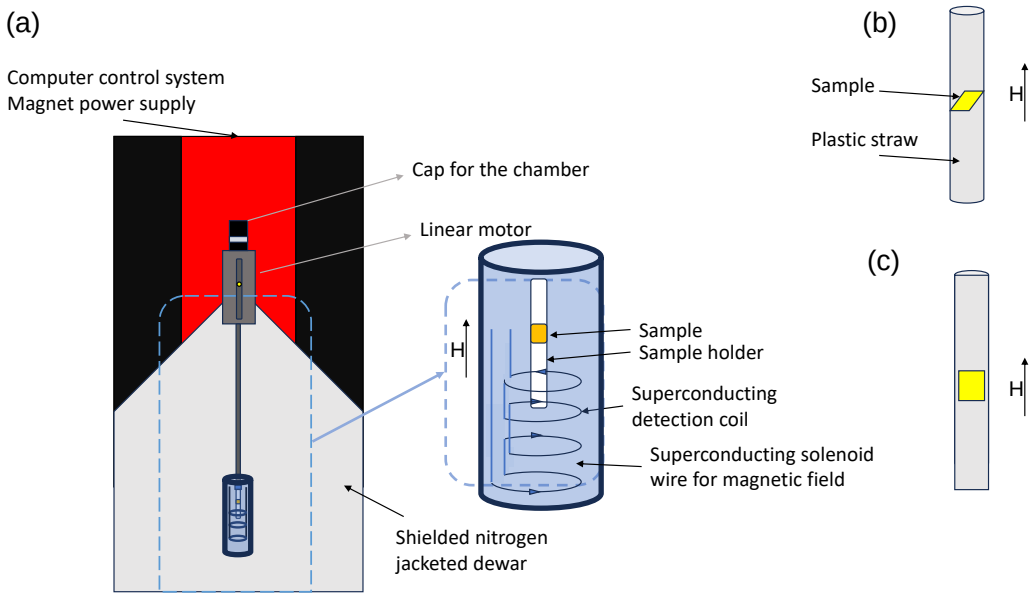

Figure 2.16: (a)The SQUID scheme and its (b) out-of-plane sample loading and (c) in-plane sample loading.

used to reduce noise from the fluctuation in the large external magnetic field. When the large applied magnetic field changed, the clockwise and counter-clockwise coils would get opposite induced voltage, and the subtraction of the voltage helps reduce the common-mode noise [128].

Two ways of loading the sample are designed to achieve the measurement for measuring the sample properties with an in-plane or out-of-plane magnetic field. To load the sample out of the plane, the traditional straw loading is applied to the sample as shown in Fig. 2.16 (b). To load the sample for in-plane measurement, the sample will be glued onto a quartz paddle sample holder as shown in Fig. 2.16 (c) [128, 129].

The sample position needs to be calibrated before the measurement. For calibration measurement, the sample is stopped at several positions, and the SQUID voltage will be collected. The stop positions versus output of the SQUID voltage will be plotted to find the position of the sample as shown in Fig. 2.17, the SQUID induced voltage V_{SQUID} with external field set to 1500 Oe as a function of sample position is modelled as a single point dipole [130]:

$$V_{\mathrm{SQUID}} = P_1 + P_2 z + P_3\{2[R^2+(z+P_4)^3]^{\frac{-3}{2}}] - [R^2+(\Lambda+z+P_4)^3]^{\frac{-3}{2}}] - [R^2+(-\Lambda+z+P_4)^3]^{\frac{-3}{2}}]\}, \tag{2.2}$$

where the parameters Λ and R refer to the longitudinal coil separation and longitudinal radius, respectively. z is the sample position. P1, P2, P3, and P4 are the four fit parameters of the dipole model. P1 is a constant offset voltage. P2 is a linear offset to account for electronic drift in the SQUIDs from data collection. P3 is the amplitude of the induced voltage, the sample magnetic moment = $\frac{P_3}{\text{device dependent factors}}$. P4 is the shift of the sample along the axis of the magnet [131]. The centre of the Gaussian fitting peak is the centre position of the sheet sample. The sample position needs to be within [63 mm, 69mm] to sit around the centre of the detection coils and gain a good signal-to-noise ratio.

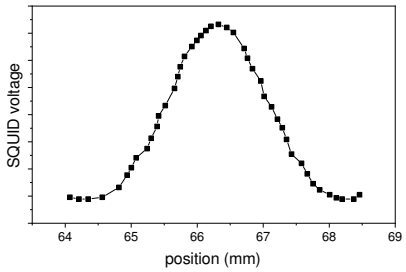

Figure 2.17: The output of SQUID $[Pt/Co_{62}B_{38}/Ir]_{20}$ sheet sample position detection of at room temperature with 1500 Oe magnetic field applied.

2.4 Micromagnetism Tool (OOMMF)

OOMMF (Object Oriented Micromagnetic Framework) was built by M. Donahue and his team [71]. As mentioned in the Theory part, the LLG equation is used to do micromagnetism simulation. The total energy used in the OOMMF is[49]:

$$\begin{aligned} E = \mathrm{A}[\nabla(\frac{\mathbf{M}}{M_\mathrm{s}})]^2 - K\frac{(\mathbf{n}\cdot\mathbf{M})^2}{{M_\mathrm{s}}^2} - \mu_0\mathbf{M}\cdot\mathbf{H} - \frac{\mu_0}{\mathbf{2}}\mathbf{M}\cdot\mathbf{H_d}(\mathbf{M}) + \\ \frac{D_{\mathrm{DMI}}}{M_\mathrm{s}^2}(M_z\nabla\frac{\partial M_x}{\partial x} - M_x\nabla\frac{\partial M_z}{\partial x} + M_z\nabla\frac{\partial M_y}{\partial y} - M_y\nabla\frac{\partial M_z}{\partial y}), \end{aligned} \tag{2.3}$$

where the first two terms are the exchange and anisotropy energy, the third term is applied field, and the fourth term demagnetisation field energy, and the rest of the equation presents the DMI energy.

OOMMF uses an object-oriented approach; the sample properties, such as the energies of different interactions, become modular and extensible. To build up the sample configuration, the coding in the software is based on Tcl/TK or C++ language. The sample properties were defined in a .mif file. Then, the .mif file was read and run by the OOMMF 3D solver interactive interface Oxsii.

The micromagnetic solver used by OOMMF is the finite difference method (FDM). The FDM simulation started with setting the size of the whole sample and each layer and then discretize them into rectangular-shaped small cells. Each cell can have finite difference of material parameters and will be set as a magnetization state. The state can react with the neighbour cells. The discretized LLG equation is used.[132] If the sample had a multilayer, then setting the sub-region in the .mif file is necessary because the demagnetization energy in OOMMF depends on the shape and size of each layer; the error can not be ignored if we regarded the multilayer samples as single-layer samples. Also, the cells must be smaller than the exchange length $l_{ex} = \sqrt{\frac{2A}{\mu_0 M_s}}$. The l_{ex} scales the length of the alignment of elementary magnets due to exchange interactions. If the size of cells is larger than l_{ex}, the details of the magnetic textures at the nanoscale will be missing. The error will be large because the size of the domain wall is not correct, and the domain displacement in the simulation will always be different from the actual displacement.

Another type of the micromagnetic solver is based on the finite-element method (FEM). The FEM will discrete the sample into different shapes of elements, the magnetization of these element will be discrete at the node points of the elements. This solver will show advantage when the sample has complex geometry or varying magnetic properties within an domain.[133] To update the simulated magnetisation configuration from one step to the next, the evolvers controlled by drivers need to be set up in the code. The Oxs SpinXferEvolve time evolver tracks Landau-Lifshitz-Gilbert dynamics [134]:

$$d\mathbf{M}/dt = -|\gamma|\mathbf{M} \times \mathbf{H}_{\text{eff}} + \frac{\alpha}{\mathbf{M_s}}(\mathbf{M} \times \frac{\mathbf{dM}}{\mathbf{dt}}), \tag{2.4}$$

and the simulation can be stopped at setting up the simulation time. The defult implementation method of this time evolver is Runge Kutta Fehlberg Method (RKF)

54. One of the key difference between the Runge Kutta Fourth method (RK4) which might be used in other evoler is the time step size. The RK4 uses a fixed time step for intergration while the time step of RKF 54 ia adaptive. The adaption of the time step is based on the estimated error of solution, so the result can remain a high level of the accuracy.[135]

The OOMMF represents the total energy of a magnetic system as a function of the magnetisation configuration in 3D. The energy minimisation evolver is controlled by minimisation drivers located local minima in the surface of the total energy. Refering to the LLG equation, $\mathbf{H_{eff}} = -\frac{1}{mu_0 \mathrm{M_s}} \frac{dE}{d\mathbf{M}}$ represents the system energy, the $\mathbf{m} \times \mathbf{H_{eff}}$ defines the torque on the magnetization. To minimize the free energy of the system, the magnetization prefers aligning with the effective field. So when the torque is zero, the energy is minimized. The simulation will stop when the $\mathbf{m} \times \mathbf{H_{eff}}/\mathrm{M_s}$ decrease to the set-up value. The initial state can be the state from the same sample affected by other interactions at any time by taking the MIF file from a specific time.

Chapter 3

Sample Characterization Data Analysis

The magnetic properties of the DMI constant D_{DMI}, the anisotropy coefficient K and exchange stiffness A are necessary for all kinds of micromagnetization models. The D_{DMI}, A and K can be obtained from the information provided by the *M-H* hysteresis loop and the Kerr microscope measurement. In this chapter, the calculation process for the $[Pt/Co_{68}B_{32}/Ir]_n$ samples magnetic properties are showed. The samples were fabricated by the DC sputtering in the IVOR. The results are also used for the simulation work in this project.

3.0.1 SQUID and Anisotropy

The anisotropy coefficient can use the magnetisation method to be obtained. The IP and OOP *M-H* loop will show the saturation magnetisation moment M_{s} and the value of anisotropy field H_{s}. The anisotropy field is obtained from the hard axis loop as shown in Fig. 3.1 and $H_{\mathrm{s}} = \frac{2K_{\mathrm{eff}}}{\mu_0 M_{\mathrm{s}}}$. The magnetocrystalline anisotropy constant $K_{\mathrm{u}} = K_{\mathrm{eff}} + \frac{\mu_0 {M_{\mathrm{s}}}^2}{2}$. The K_{u} is the uniaxial anisotropy arises from the magnetocrystalline and considered in the simulation by the anisotropy energy term. K_{eff} unlikes the magnetocrystalline anisotropy, is called shape anisotropy. The Stoner-Wohlfarth model explained that the shape anisotropy is due to the demagnetizing fields due to its shape. Assuming the total energy of the system is $E = K\sin(\theta)^2 - HM_{\mathrm{s}}\cos\big(\theta - \phi\big)$, where θ is the angle between **M** and easy axis and ϕ is the angle between the external field and easy axis. A single domain ferromagnetic material with finite size contains the energy related to the demagnetization factors $N_i j$ $(i, j = x, y, z)$. The energy term now is $E = K\sin(\theta)^2 + 2\pi(N_{xx}M_x^2 + N_{yy}M_y^2 + N_{zz}M_z^2) - HM_{\mathrm{s}}\cos\big(\theta - \phi\big)$. Thus $K_{\mathrm{eff}} = K_{\mathrm{u}} - \frac{\mu_0 {M_{\mathrm{s}}}^2}{2}$.[136, 137]

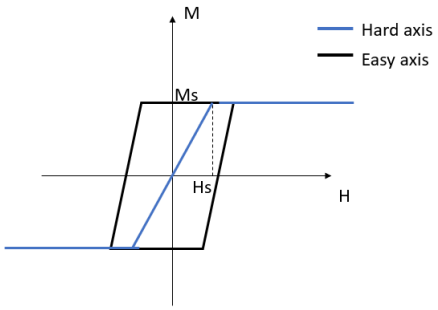

Figure 3.1: *M-H* loop with perpendicular magnetic easy axis

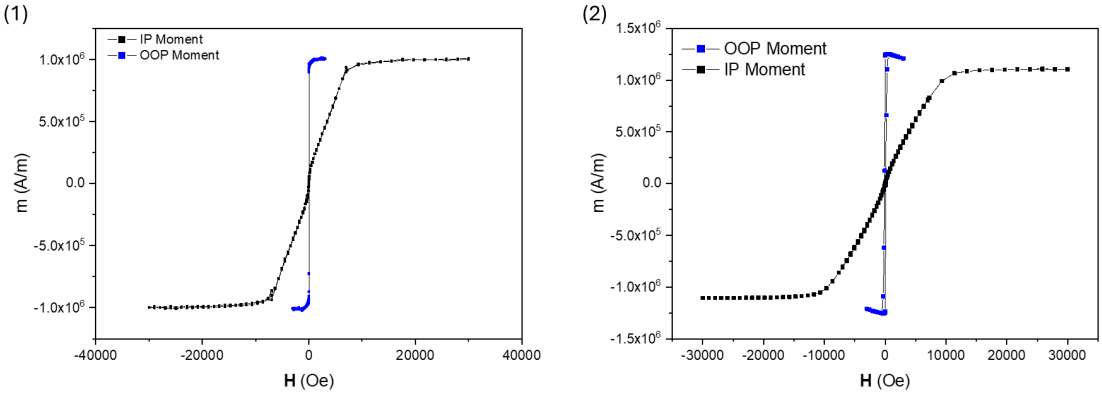

Figure 3.2: The *M*-*H* loop of (1) n=1 sample and (2) n=10 sample.

The IP and small field OOP *M*-*H* loops of [Pt/$Co_{68}B_{32}$/Ir] and [Pt/$Co_{68}B_{32}$/Ir]$_{10}$ are shown below in Fig. 3.2. When there is a prefectly isotropic magnetic film, its M_s given by the IP and OOP measurement would be the same. If they drift between each other, it is because the crystalline anisotropiy and the interfacial anisotropy from the multilayer structure. A stronger OOP anisotropy will let the sample have a high M_s in OOP measurement. To reduce the error from the system background, a well-known thick material of the same size can be the calibration sample. By measuring the calibration sample, we can know the factor that causes errors in the SQUID dynamic system, such as sample positioning or sample contamination. If the M_{scal} (the measured saturation moment of the calibration sample) of the calibration sample is smaller than the known value $M_{scaltheory}$ (the saturation moment of the calibration sample in theory), then the M_s of the same size of the samples measured from that system should multiply with $\frac{M_{scaltheory}}{M_{scal}}$.

The saturation magetization error is from the moment. The errors are large because the thickness of the CoB layer is almost 10% of the CoB thickness. And the $M_s = \frac{M}{V_{mag}}$, where V_{mag} is the volume of the magnetic layer. The error of the V_{mag} is the area of the sample times the thickness error, the M_s error ΔM_s is $M_s \cdot \frac{\Delta V_{mag}}{V_{mag}}$. But we can tell that the M_s of same material $Co_{68}B_{32}$ is around 1100 ±100 emu/cc without considering the magnetization from the polarised Pt.

The proximity to the magnetic order of the adjacent layer between Pt and $Co_{68}B_{32}$ will cause the Pt polarisation. Because lack of SQUID data from varying thickness of the $Co_{68}B_{32}$ layer to compare with the bulk magnetisation of $Co_{68}B_{32}$, I refer to the toy

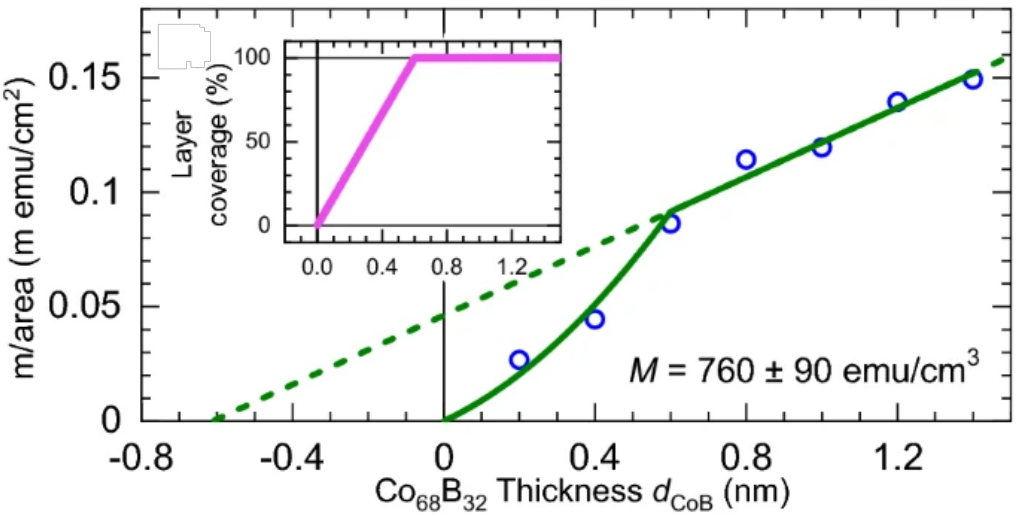

Figure 3.3: The magnetization data of different $Co_{68}B_{32}$ thickness.[138]

model published from a member of our group who use the same $Co_{68}B_{32}$ target. In Nathan's paper, he mentioned the polarised Pt is 46 $\pm 9 \mu$emu/cm^2 from the y-intercept of the fitting line for thick magnetic layer samples as shown in Fig. 3.3.[138] The relation between the repetition of the [Pt(0.7nm)/$Co_{68}B_{32}$(0.8nm)/Ir(0.5nm)]$_n$ samples and their M_s is plotted below in Fig. 3.4(a).

The relation between the repetition of the [Pt/$Co_{68}B_{32}$/Ir]$_n$ samples and their K_{eff} is plotted below in Fig. 3.4(b). The error is from the M_s, $\Delta K_{eff} = \frac{1}{2} H_s \cdot \mu_0 \cdot \Delta M_s$. The higher repetition seems to have larger anisotropy. The $K_u = K_{eff} + \frac{1}{2}\mu_0 M_s^2$, due to it being mostly based on the M_s, so the tendency will be the same as the M_s and K_{eff}. The K_u and K_{eff} of [Pt/CoB/Ir]*5 sample is smaller than the expected value might be due to the small thickness of CoB and large error. The overlap errors of the n = 1 sample and n = 5 sample give the possibility that K_{eff} of n = 1 sample can be smaller than n = 5 sample. Since the CoB target used in the sputtering was same for all the samples, the M_s should be same for every sample. In that case, the anisotropy energy should slightly increase with increasing repetition n because of the increasing magnetic layer volume.

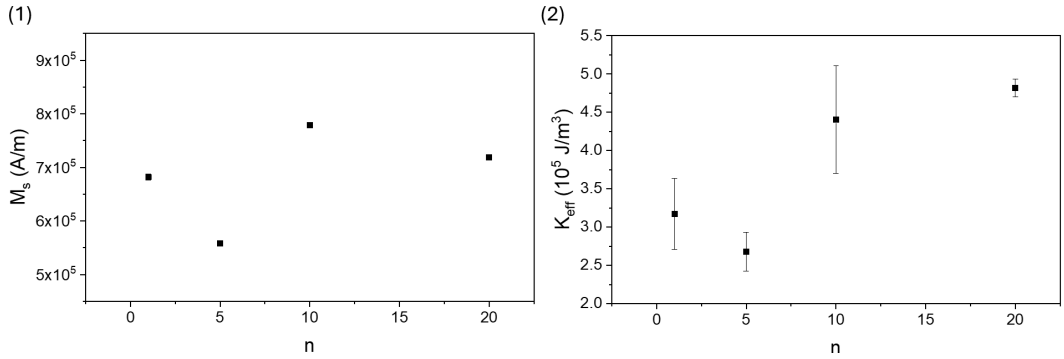

Figure 3.4: (a)The saturation fields of $[Pt/Co_{68}B_{32}/Ir]_n$ samples and (b) the $[Pt/Co_{68}B_{32}/Ir]_n$ samples K_{eff} after the correction of the polarisation of Pt.

3.0.2 SQUID and Exchange stiffness

The exchange stiffness can be calculated from the Bloch law theoretically. The Bloch law predicted that $\frac{M_s(T)}{M_s(0K)}$ is propotional to the $1-\alpha T^{\frac{3}{2}}$.[73]. Because the SQUID VSM can hardly provide a measurement lower than 3K, the M_s in 0 K must first be predicted. Then the $M_s(0K)$ will be used to fit the formula: $\frac{M_s(T)}{M_s(0K)} = 1-\alpha T^{\frac{3}{2}}$, where α is just the slope of the fitting curve of data,

$$\frac{M_s(T)}{M_s(0K)} = 1 - 0.0587\sqrt{Qs}\left[\frac{k_B T}{2A(T)a}\right]^{\frac{3}{2}},$$

where Q is the number of the neighbouring atoms, a is the lattice constant (e.g. a for FCC Co is 3.54 angstroms), spin quantum number $s = \frac{M_s(0K)a^3}{Qg\mu_B}$ and g is g-factor which is around 2. But the sample contain $Co_{68}B_{32}$ is amorphous material which does not have lattice constant. So, the amorphous Bloch law will be used. In amorphous Bloch law, $\alpha = 2.612\frac{g\mu_B}{M_s(0K)}(\frac{k_B}{4\pi C})^{\frac{3}{2}}$, where $A = \frac{M_s(0K)C}{2g\mu_B}$ [139]. The exchange stiffness is $A = \frac{C\rho s}{2g\mu_B}$, where C is the spin wave stiffness constant and $\rho = \frac{100}{\frac{68}{\rho_{Co}}+\frac{32}{\rho_B}}$ is the density of the magnetic layer. The constant 2.612 is from the Riemann's Zeta-functions that indicated $\zeta(3/2) = 2.612$, which relates to the order of the temperature T [140].

The exchange stiffness A is related to the $M_s(0)$ and the slope of the function $\frac{M_s(T)}{M_s(0K)} = 1-\alpha T^{\frac{3}{2}}$, the error of the exchange stiffness A will arise from the error of M_s and the error of fitting slope. As an example, the saturation part of the n=1 sample *M-H* loop and the figure of M_s versus $T^{\frac{3}{2}}$ are below in Fig. 3.5 (a). As shown in Fig. 3.5, most of the M_s can be found obeying the rules that higher temperature will have lower

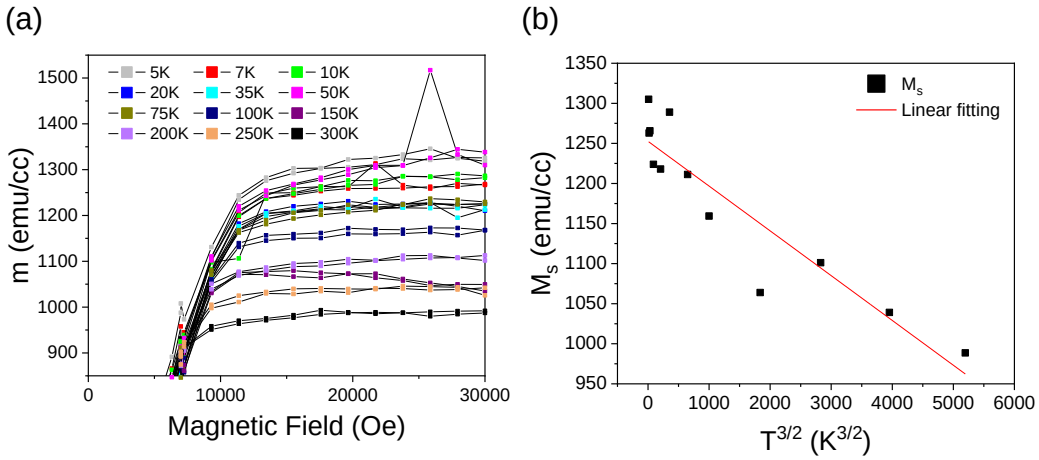

Figure 3.5: (a) The n=1 sample M_s raw data in varying temperature and (b) the n=1 sample $M_s(0)$ and Bloch law fitting

M_s, but M_s with T= 50K, 200K show a much higher value than the expected value. The fitting equation of Fig. 3.5 is $M_s = 1250 - 0.056T^{\frac{3}{2}}$. In Bloch model, $\frac{M_s(T)}{M_s(0K)} = 1 - \alpha T^{\frac{3}{2}}$ and the intercept is 1, so the intercept of the fitting equation is the predicted $M_s(0K)$, the slope that used to calculate spin wave stiffness and exchange stiffness is the ratio of the slope and the intercept of the fitting equation. As mention before, the raw data of the SQUID measurement need to be corrected with the consideraion of Pt polarisation. So the $M_s(0K)$ after correction is 928 emu/cc. With the equation that $\alpha = 2.612\frac{g\mu_B}{M_s(0K)}(\frac{k_B}{4\pi C})^{\frac{3}{2}}$, the error of the C is $\Delta C = C \cdot \frac{4\pi}{k_B}\frac{-2}{3} \cdot (\frac{1}{2.612 g\mu_B})^{\frac{-2}{3}} \sqrt{(\frac{\Delta M_s(0K)}{M_s(0K)})^2 + (\frac{\Delta\alpha}{\alpha})^2}$. The error bar of the intercept ±20 emu/cc is regarded as the $\Delta M_s(0K)$, so the spinwave stiffness C of n=1 sample is 0.99 ± 0.13 (10^{-40}J/m^2).

The exchange stiffness A then can be obtained from C with $\Delta A = A \cdot \frac{1}{2g\mu_B}\sqrt{(\frac{\Delta C}{C})^2 + (\frac{\Delta M_s(0K)^2}{M_s(0K)})}$. The exchange stiffness A of the n=1 sample is 2.5 ± 0.1 pJ/m. The exchange stiffness versus the repetition of the samples in Fig. 3.6 can show that the exchange stiffness has a similar changing pattern of the M_s in 300K. The exchange stiffness will not change with the increasing stack repetition. It only depends on the M_s as they are all the magnetic material $Co_{68}B_{32}$ properties and will not be affected by the interlayer energies.

The paper from Knoc shows that the Co_xB_{100-x} has a component percentage sens-

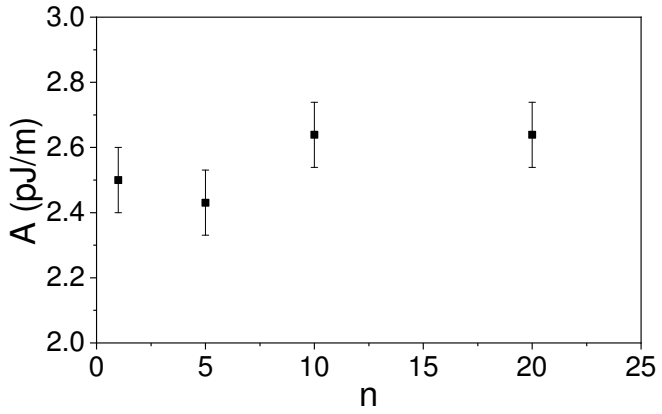

Figure 3.6: The $[Pt/Co_{68}B_{32}/Ir]_n$ samples set exchange stiffness

itive dependence of exchange stiffness.[141] When x drops from 80 to 20, the exchange stiffness drops from 9.8 pJ/m to 3.4 pJ/m. The values of A of $Co_{68}B_{32}$ around 2.4 to 2.7 pJ/m are smaller than the literatures about bulk samples but close to the estimation (1.7 pJ/m and 2.4 pJ/m) of 5 and 6 angstroms $Co_{68}B_{32}$ thin film from other researcher.[142] If using the parameters of Co to estimate, $A = \frac{NC}{2a^3}$, where N= 4 for FCC. The rough estimated result will be 4.5 pJ/m for n=1 sample.[143] Since the K_{eff} and A both have the same changing pattern except the K_{eff} in the n=20 sample is slightly larger than the one of n=10, the DMI calculation result might be strict in a small range.

The ferromagnetic resonance (FMR) is another way to obtain the spin wave stiffness, which does not require Bloch law fitting. The frequency of the resonance and the known anisotropy of the material can give the spin wave stiffness. Refering to $A = \frac{M_s(0K)C}{2g\mu_B} =$, the exchange stiffness can be obtained more straight forward and considerable in the future work.[144]

3.0.3 D_{DMI} from Bubble Expansion Method for Repeat Stacks Less Than 2

The bubble expansion method is based on the effect of the different directions and amplitudes of IP fields applied to the nucleated domain. The bubble expansion will not be suitable for n<2 samples because it is hard to find a nucleated domain which will not touch the others after expanding. To get the image of nucleated domains for the bubble domain expansion, a magnetic field that can fully saturate the sample in an out-of-plane direction will be applied with a 1-2-second pulse. This pulse helps align the

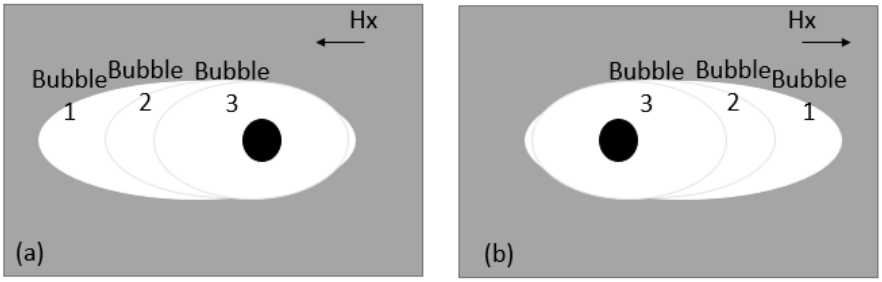

Figure 3.7: (a)DW bubbles 1, 2 and 3 overlapped comparison with Hx points to left-hand side ($H_{x3} > H_{x2} > H_{x1}$) (b)DW bubbles 1, 2 and 3 overlapped comparison with Hx points to the right-hand side ($H_{x3} < H_{x2} < H_{x1}$)

majority of magnetic moments within the sample in the same direction. This alignment will allow the Kerr microscope to capture the response of the magnetic pattern to the next applied field, especially enhancing the contrast of the domain with the opposite magnetisation direction. After that, an opposite direction with an amplitude smaller than the saturation field as a nucleation magnetic field will be applied. Take the image as the background and remove it with Kerr microscope software; if another magnetic field was applied to the sample again, the comparison between the new domain and the nucleated domain would be shown. The new domain will be dark, and the nucleated domain will be the bright part in the middle of the black domain.

Fig. 3.7 shows the mode of the velocity antisymmetry that the domain wall expansion velocity will be faster along the direction same as the IP field. Hrabec tried to explain the antisymmetry domain movement caused by the IP field. He suggested that the magnetic sample will have Néel type domain walls but not Bloch type when it has a high DMI. The strong DMI will maintain the rotational system, so the bubbles will remain symmetry when the external field only contains the component parallel to the easy axis.The IP field makes the moment in the direction of the IP field being antiparallel and breaks the symmetry [145]. The in-plane field rised a force on the domain wall which competes with the effective field fro DMI. When the force between DMI and in-plane field is balanced, the velocity of the DW will be minimized. So, the velocity of the DW versus the amplitude of the IP field will give us the H_{DMI}, where is the location of the lowest velocity. The DMI constant D can be calculated by the equation $D_{\mathrm{DMI}} = \mu_0 H_{DMI} M_{\mathrm{s}} \Delta$, where $\Delta = \pi \sqrt{A/K_0}$, A is the exchange stiffness,

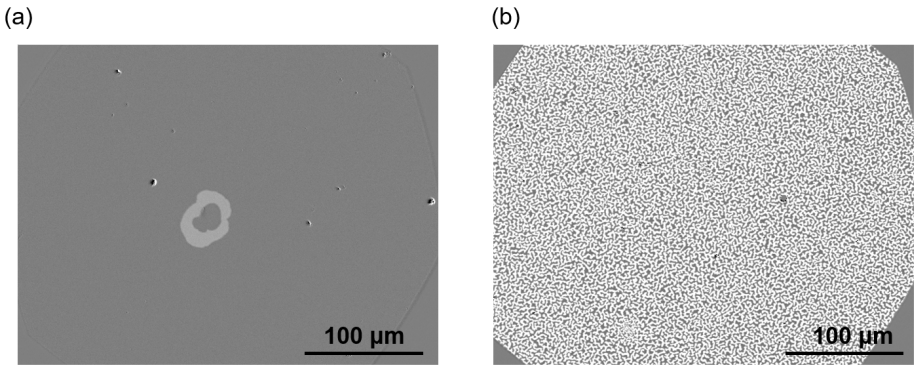

Figure 3.8: (a) The difference image of nucleated domain of n= 1 sample with IP field 225 Oe and expansion field 6 Oe, (b) The n= 5 sample maze demagnetization pattern.

$K_0 = 2K_{\text{eff}} - K_{\text{u}}$, K_{eff} is the effective anisotropy coefficient and K_{u} is the unidirectional anisotropy energy density related to the demagnetization.

The Kerr microscope was used to measure the domain images of samples. The domain pattern images of $[Pt/Co_{68}B_{32}/Ir]_n$ samples with n= 1 and n=5 are in Fig/ 3.8 (a) and (b) which are the typical domain images for n=1 sample and n>2 samples, respectively. So, the bubble expansion method was used to calculate the DMI of the n=1 sample. The black bubble is the first nucleated domain, and the white bubble is the expansion of the nucleated domain with a short OOP field (6Oe) pulse and an IP field. The sign of IP represents the orientation of the field; '+' means pointing to the left, and '-' means pointing to the right. In Fig. 3.9, the bubble has a larger expanding velocity along the direction of H_{x}. Two possible reasons will cause the error and bring unreliable results: the nucleation pulse is not fixed at the second time and the IP field is not parallel to the sample surface. They cause the error because the bubble will keep growing all the time and might stop at an unknown point, with an unexpected z-axis magnetic field component accompanies by the in-plane magnetic field pulse. To avoid the first problem, the sum of nucleation field pulse width and delay pulse width must be 1-2s smaller than the total pulse width in order to let the computer and software control the power of coils well. The second problem is because of the wrong alignment of the IP coils, so manually adjusting the coil and measuring the size of the bubble to let the bubble expands the same distance in both hand side (symmetrically with respect to the centre of the original bubble) is necessary.

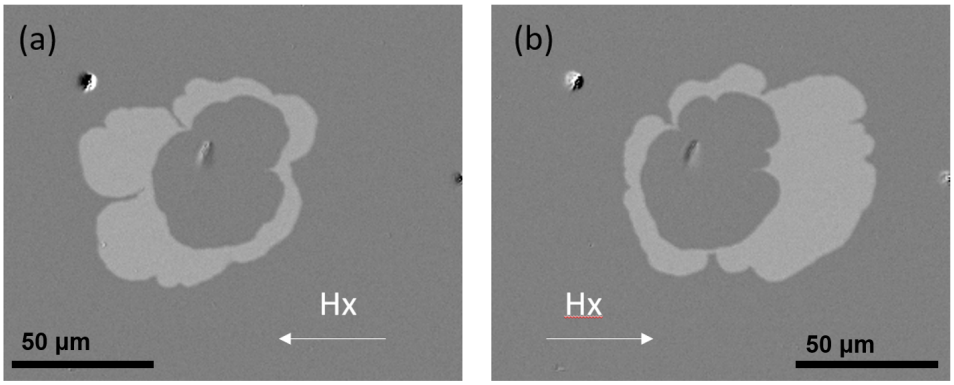

Figure 3.9: DW movement with (a) 660 Oe and (b)-690 Oe Hx

Results from bubble expansion of left and right domain walls are shown in Fig. 3.10. The H_{DMI} is the location of the minimum of v, for n=1 sample, H_{DMI} = 48.4 ± 0.1 mT.

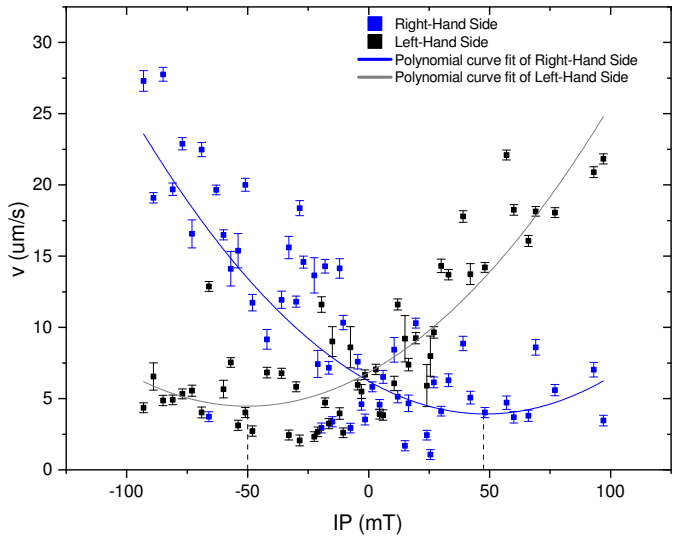

Figure 3.10: DW velocity versus IP of the left-hand (black) domain wall and right-hand (blue) domain wall

So the DMI constant D_{DMI} is 0.35 ± 0.1 mJ/m^2.

3.0.4 D_{DMI} from Demagnetisation Pattern Calculation for Repeat Stacks More Than 2

The Kerr microscope can also provide the demagnetisation pattern of the sample. A quick $M-H$ loop will be scanned to find the full saturation field of the sample. The switching point H_{switch} where the moment increases sharply with the increasing external field. To image the demagnetisation pattern, the sample will be fully saturated, and the background will be taken and removed without any external field. Then, an AC field, which will decay to 0 mT with an initial amplitude of H_{switch}, is applied to give a demagnetisation pattern of the sample. For the maze demagnetisation pattern, the period with length unit is related to the DMI constant. The period can be obtained from the fast Fourier transform because the peak location of the power density spectrum gives $\frac{1}{\lambda}$. The Lemesh model is mostly used in DMI research. He assumed the system only has a single domain first and then calculated the DW energy [146]. To obtain the equilibrium domain width (which is assumed to be half of the Domain period), the DW energy E_{DW} equation needs to be minimised, respected to the domain width W. The condition is the partial derivation result of the E_{DW}/W. Here,

$$E_{DW} = \frac{1}{W}[2\Delta K_{\mathrm{u}} + \frac{2A}{\Delta} + \pi D_{\mathrm{DMI}} \sin\psi + E_{ds}^{ij} + E_{dv}^{ij}], \tag{3.1}$$

where E_{ds}^{ij} and E_{dv}^{ij} is the surface and the volume stray field energies per domain wall area, i is the number of the DW and j is the repeat number n. In a single domain wall model, i and j are all equal to 1. The condition to minimize the E_{DW} is:

$$\frac{\partial E_{dv}^{ij}/W}{\partial W} + \frac{\partial E_{ds}^{ij}/W}{\partial W} = \frac{2\Delta K_{\mathrm{u}} + \frac{2A}{\Delta} + \pi D_{\mathrm{DMI}} \sin\psi}{W^2}. \tag{3.2}$$

The $E_{ds}^{\infty 1}$ and $E_{dv}^{\infty 1}$:

$$E_{ds}^{\infty 1} = \frac{\mu_0 M_{\mathrm{s}}^2}{2}(1 - \frac{2W}{\lambda})^2 + \frac{2\pi\mu_0 {M_{\mathrm{s}}}^2 \Delta^2}{\lambda d} \times \sum_{n=1}^{\infty} \frac{\sin\frac{\pi n W}{\lambda}^2}{\sinh\frac{\pi^2 n\Delta}{\lambda}^2} \frac{1 - \exp\left(-\frac{2\pi n d}{\lambda}\right)}{n} \tag{3.3}$$

$$E_{dv}^{\infty 1} = \frac{2\mu_0 M_{\mathrm{s}}^2 \Delta^2 \sin\psi^2}{2} \times \sum_{n=1}^{\infty} \frac{\sin\frac{\pi n W}{\lambda}^2}{\cosh\frac{\pi^2 n\Delta}{\lambda}^2} \frac{\exp\left(-\frac{2\pi n d}{\lambda}\right) + \frac{2\pi n d}{\lambda} - 1}{n}, \tag{3.4}$$

where d is the film thickness, ψ is the DW angle. Because the j will not be 1 when using the model to calculate multi-stack samples, factor f transfers the parameters from multi-stack samples to non-repeat samples, $f = d_{\mathrm{m}}/P$, d_{m} is the thickness of the

magnetic layer in the stacks, and P is the period of DW. Then $A_n = fA$, $D_n = fD$, it can also apply to other parameters [147].

Meier and his team pointed to another model, which is more direct and simple without a summation function [148]. They calculated the domain width W with one unknown independent variable Δ,

$$W = \frac{\pi}{2} l_{eq} \exp\left(\frac{4\pi A}{\Omega l_{eq}} - \frac{\pi k \Delta}{2}\right), \tag{3.5}$$

$$l_{eq} = \sqrt{\frac{A}{K_{\text{eff}}} + \frac{\Omega^2}{16\pi^2 {K_{\text{eff}}}^2}} - \frac{\Omega}{4\pi K_{\text{eff}}}, \tag{3.6}$$

where $\Omega = \mu_0 M_s^2$ is the energy of the dipole interaction, l_{eq} is domain parameter in equilibrium state and Δ is the domain shape parameter. Different domain wall types will have different Δ. When DW is Bloch type, $\Delta = 0$; when DW is canted wall, $\delta = (\frac{\pi D_{\text{DMI}}}{k\Omega})^2$ and $\frac{\pi D_{\text{DMI}}}{k\Omega} < 1$. The DW is always Néel type in Pt/CoB/Ir samples, which has

$$\delta = (\frac{2}{k\Omega})(\pi |D_{\text{DMI}}| - \frac{1}{2} k\Omega), \quad \frac{\pi D_{\text{DMI}}}{k\Omega} > 1. \tag{3.7}$$

The type of DWs need not be confirmed before using the Meier model because the Néel Δ will definitely be larger than 1, and canted DW will have Δ smaller than 1 because the defined Δ equation [148].

For sample with n larger than 2, it is hard to find a nucleated domain, so the periodicity of the demagnetisation pattern is concerned. To obtain the period of the domain λ, the fast Fourier Transform(FFT) is applied to the image. The peak location of the power Density Spectrum can give the information of λ, which is assumed to be 2W. Fig. 3.11 shows the original image used to apply FFT, the FFT figure and its PDS. In the FFT image, the corners are the high-frequency regions, and the centre of the image is the low-frequency region. The intensity of the pixels is the Power Spectral Density (PSD) intensity. The peak location of the PDS is $\frac{1}{\lambda} = \frac{2}{W}$. λ and W will be put in the Lemesh model to obtain the DMI constant D_{DMI}. The λ, K_{eff}, A and other parameters to calculate the DMI constant are shown in the table 3.1 below, the DMI constant of n=1 sample is not calculated from the Lemesh method but put in that cell to compare with the others.

The DMI constants calculated from two different methods are plotted in Fig. 3.12. In low repetition samples, the results from both methods are almost the same with

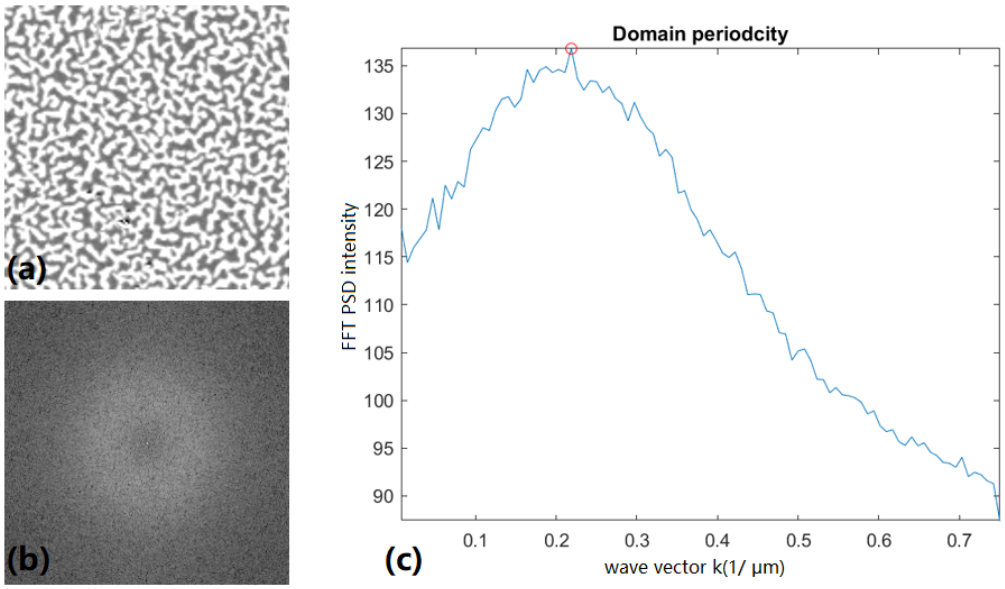

Figure 3.11: (a)The maze demagnetisation pattern of n=5 sample and (b) its FFT figure and (c) the power density spectrum

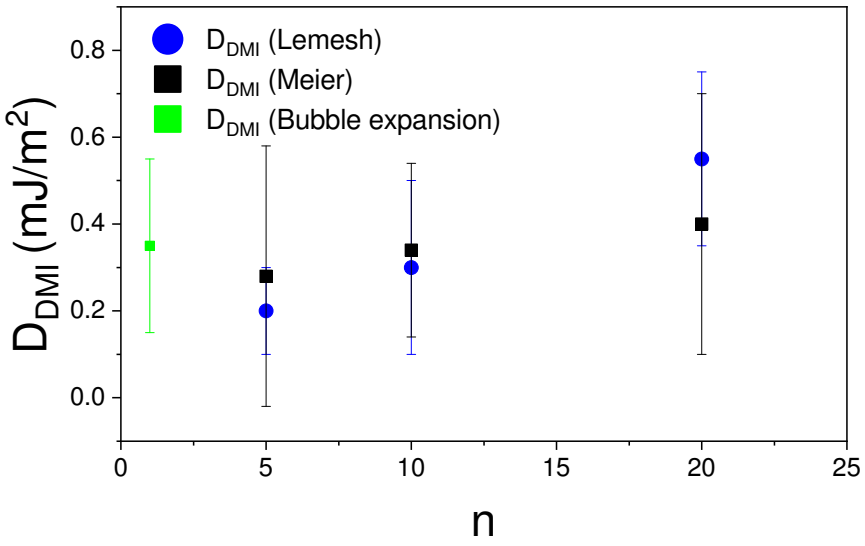

Figure 3.12: The DMI constant of varies repetition N from Lemesh and Meier method.

a difference smaller than 0.1mJ/m^2. However, in high repetition sample n=20, the Meier method gave a smaller value because the factor of demagnetising energy and

n	λ (μm)	K_{eff} (MJ/m^3)	A (pJ/M)	$\frac{d_{\text{m}}}{\text{d}_{\text{stack}}}$	D_{DMI}(Lemesh) (mJ/m^2)	D_{DMI} (Meier) (mJ/m^2)
1	-	0.32± 0.05	2.5± 0.1	0.21	0.35 ± 0.2	
5	4.57	0.27± 0.03	2.4± 0.1	0.23	0.2± 0.1	0.3± 0.3
10	0.63	0.44± 0.07	2.6± 0.1	0.25	0.3± 0.2	0.3± 0.2
20	0.74	0.48± 0.01	2.6± 0.1	0.22	0.6 ±0.2	0.4 ± 0.3

Table 3.1: The magnetic properties of $[Pt/Co_{68}B_{32}/Ir]_n$ samples, where d_{stack} is the sickness of the repeated stack.

repetition is not considered in the original Meier method.

Since the simulation based on the n=1 properties was done, D_{DMI}=0.7mJ/m^2 can stabilise a skyrmion with an external field over 100 mT. So, the DMI constant value of n=20 is above 1 mJ/m^2, which can be reliable and strong enough to stabilise a skyrmion in the simulation with an smaller external field than n=1 sample. Though the DMI constants of other samples are small, it is still worth studying whether it can hold the skyrmion with an external field or pin the skyrmion by using random distribution magnetic parameters like Zeissler et al. did before [149].

Chapter 4

Simulation of the motion of spin wave-driven skyrmions in magnetic nanotracks

OOMMF software can realise the simulation of the motion of a skyrmion driven by propagating spin waves (SWs) in a thin film track. The numerical micromagnetic simulations were done with interfacial perpendicular magnetic anisotropy and Dzyaloshinskii-Moriya interaction.

Numerical micromagnetic simulations are well-suited to studying skyrmion dynamics driven by the SW, and there are many recent examples, in most of which the track for the skyrmions is narrower than 100 nm or not larger than 4 times the skyrmion diameter [42, 49, 50, 68–70]. By studying the skyrmion motion in tracks of different width, we can predict the skyrmion motion in an experimentally achievable sample. We also study the SW-driven skyrmion motion as a function of varying the Gilbert damping constant.

At long simulation times, the skyrmion is found that always moves in the direction of the spin wave propagation. At shorter times, rather than observing skyrmion motion in a single direction, the skyrmion shows transient retrograde motion when the track width is wider than 50 nm (for Gilbert damping $\alpha = 0.02$) or $\alpha < 0.06$ (for a track width of 100 nm).

4.1 Simulation Setup

We have performed numerical micromagnetic simulations using the Oommf package [71]. The simulation cell dimensions were set to [1 nm, 1 nm, 0.4 nm]. The magnetic track thickness $d_m = 0.8$ nm. We simulated wires with a length of 1000 nm and variable width w, in the range 40 to 100 nm. The track geometry is depicted in Fig. 4.1. The value of α was selected for each sample from the range [0.02, 0.06], but in the regions close to the ends of the track we set $\alpha = 1$ so the SWs are not reflected back along the track. The materials parameters used are based on the representative magnetic properties of a [Ta/Pt/$Co_{68}B_{32}$/Ir/Pt] sheet film prepared in our laboratory, the parameters can be found in §3.0.4. We successfully stablized the skyrmion with $D_{DMI} = 0.7$ mJ/m^2 in the early simulation. To make the skyrmion can be more stable in an external field smaller than the SW excitation field, we change the simulation sample D_{DMI} to 1.5 mJ/m^2, the simulated magnetic properties are shown in Table 4.1.

The initial magnetization was fully saturated normal to the x-y plane. The spin waves were excited by applying a time-dependent magnetic field $H_0 \sin(2\pi f t)$, direc-

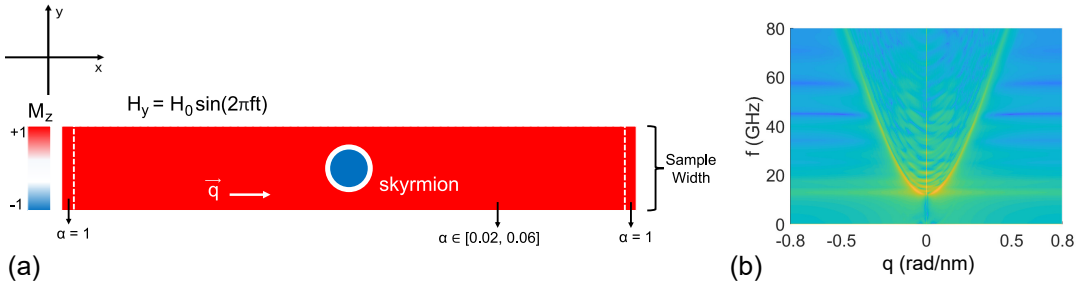

Figure 4.1: Spin wave excitation in a magnetic track. (a) The sample geometry simulated in OOMMF, with a red-blue color scheme used to depict the z-component of the magnetization. The track is 1000 nm long and of variable width w. The damping constant α is set to 1 in 10 nm long regions at the ends of the track to avoid spin wave reflections and takes variable values in the range 0.02-0.06 in the main part of the track for different simulations. A skyrmion, shown schematically, is initialized at the center of the track at $x = 0$ nm. The spin wave excitation field is localized at a position $x = -150$ nm with time dependence $\mathbf{H}_y = H_0 \sin(2\pi f t)\hat{\mathbf{y}}$. (b) The dispersion relation f(q) for spin waves in the 100 nm width and $\alpha = 0.03$ nano track, showing the expected parabolic form.

Table 4.1: Micromagnetic parameters representing typical values for an experimental sample.

Parameter	Symbol	Value	Unit
Saturation Magnetization	M_s	1.004	MA/m
Exchange Stiffness	A_{ex}	3.6	pJ/m
Anisotropy Constant	K_u	1.0	MJ/m^3
DMI Constant	D_{DMI}	1.5	mJ/m^2

ted along the y-axis, where $\mu_0 H_0 = 800$ mT is the amplitude of the exciting field and $f = 80$ GHz is the frequency. The frequency of the SWs will be the same as the exciting field. The excitation field is localized to one column of cells located at $x = -150$ nm.

To obtain the dispersion relation $f(q)$ of the SWs, shown in Fig. 4.1(b), sinc pulses $\sin(\frac{\omega t}{t})$ of varying frequency were applied to the track which was in a static saturating field of $\mu_0 H_z = 100$ mT. The magnetization data was used as the input signal to a

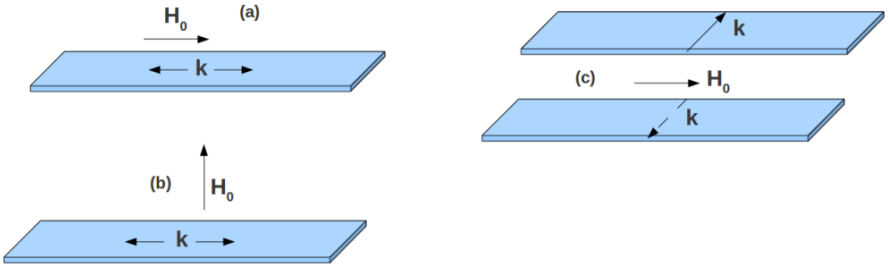

Figure 4.2: The spin wave excitation geometries: (a) backward volume, (b) forward volume and (c) surface spin waves.[150]

discrete Fourier transform process to obtain the wave vector k. [150] The Fourier transform of a sinc function is a rectangular (hat) function, which makes sinc pulses an useful tool for exciting a finite bandwidth frequency spectrum. The signal after FFT is easy to be seperated from noise. The magnon mass calculated from this spin wave dispersion relation is $m = 2.41\times10^{-29}$ kg [83]. The angular frequency $\omega = \omega_0 + \lambda_{ex}\omega_M q^2$, where $\lambda_{ex} = \frac{2A}{\mu_0 M_s^2}$, ω_0 is the zero-wavevector angular frequency and $\omega_M = \gamma_0\mu_0 M_s$, the quadratic relationship between frequency and wavevector showed in Fig. 4.1(b) obeys the dispersion relation.[150] In this project, the simulated spin wave is excited in the forward volume mode as shown in Fig. 4.2 (b), where the external field is perpendicular to both the wavevector and the sample surface. There are also other spin wave geometries showed in Fig. 4.2 (a) backward volume and Fig. 4.2 (c) surface spin waves. In the backward volume wave configuration, the vector of the magnetic field is parallel to and aligned with the wavevector. The surface wave configuration has the external field perpendicular to the wavevector but also lies in the plane of the sample surface.

To study SW-driven skyrmion motion, I firstly stabilized a skyrmion spin texture. A static external field H_z is applied on the whole sample along the z-axis. A Néel-type skyrmion was nucleated and relaxed at the center of the track where $x = 0$. The equilibrium diameter found after this procedure is 17 nm. The SW excitation was then switched on with $f = 80$ GHz. Spin waves propagate away from the excitation region along the x-direction, driving the motion of the skyrmion when they reach it.

4.2 Simulation Results

4.2.1 Retrograde Motion of Skyrmions in Wide Track

A spin wave propagating along the x-axis induces skyrmion motion, shown in Fig. 4.3(a). Fig. 4.3 (b) and (c) show the skyrmion displacement along the x- direction and the y-direction as a function of simulation time with different track widths in the range w = 40-100 nm and a 0.1 ns timestep. These simulations were carried out with the Gilbert damping set to $\alpha = 0.02$. When the track is narrow, $w \lesssim 50$ nm, the skyrmion is driven along the propagation direction of SW as shown in the $w = 40$ nm example of Fig. 4.3 (a). In this case, the x-component of the skyrmion velocity is always positive.

For wider tracks, the motion is more complex as shown for the $w = 90$ nm example depicted in Fig. 4.3(a). The skyrmion shows negative initial velocity along x. The skyrmion also has a y-component of velocity, since the gyrotropic motion will also lead to the skyrmion moving toward the upper edge, as seen in the 90 nm track width example shown in Fig. 4.3(a) and (c) [79, 151]. The transient retrograde motion stops when the skyrmion approaches the track edge after a few tens of ns, and the skyrmion then begins moving along the edge in the positive x direction. The skyrmions will have to move up further to reach the track edge before changing direction for the wider tracks, as shown in Fig. 4.3 (b) and (c). As the theory based on the SW scattering on skyrmion shows in Eq. 1.8 and 1.15, $\mathbf{f}_{\text{scatter}}$ always drives the skyrmion towards the SW source on a borderless sample. The skyrmions all move towards the top edge until the distance between the skyrmion center and the upper edge is around 25 nm before starting to have positive velocity on the x-axis.

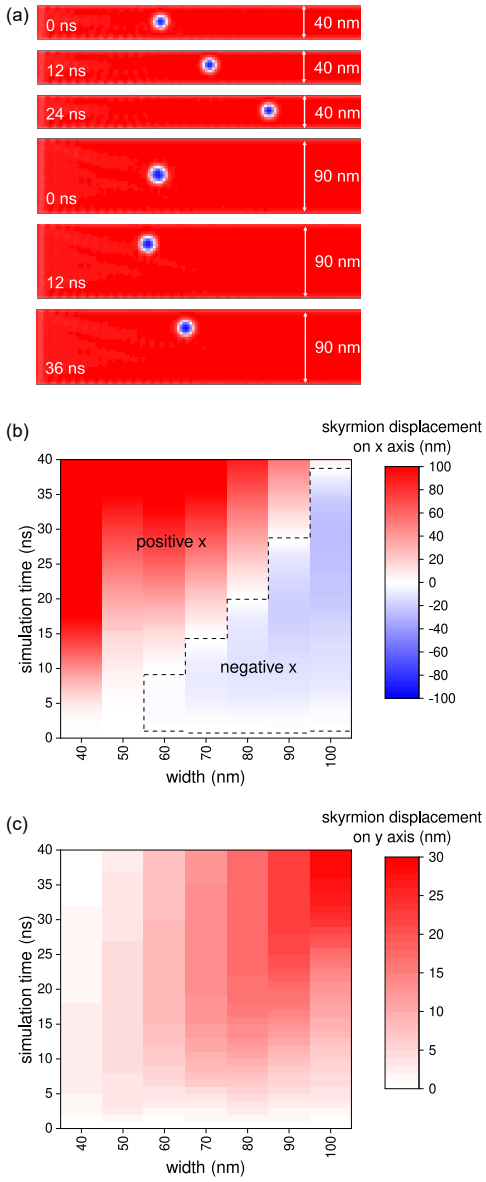

Figure 4.3: Spin wave-driven skyrmion motion. (a) Snapshots at different simulation times of samples with track widths = 40 nm and 90 nm. Time-dependent skyrmion displacement on the (b) x-direction and (c) y-direction for various magnetic track widths in the range 40-100 nm. The region enclosed by the dashed line in (b) is where the skyrmion x-displacement is negative w.r.t. the starting position.

Close to the sample edges, the presence of D_{DMI} gives rise to a twist in the magnetiz-

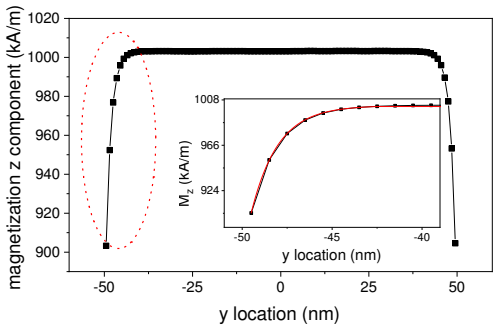

Figure 4.4: Out-of-plane component of magnetization M_z across the track width direction (y-axis) for the $w = 100$ nm wide track. The inset graph shows that the z-component of magnetization depends exponentially on distance from the edge, with a fit to $M_z = M_s - M_c \exp\left[-(x - \frac{w}{2})/L_{edge}\right]$ in the range [−50 nm, −40 nm] region, where M_c is half the largest difference between the twisted magnetization and the saturation magnetization.

ation away from the z-axis [72]. As an example, the z-component of the magnetization for the 100 nm width sample in the notionally uniform state (i.e. without a skyrmion) is shown in Fig. 4.4. A canting away from the z-direction is visible that extends for a few nm into the track from its edge. This twisting gives rise to the edge force $\mathbf{f}_{edge}$ discussed in §1.5 above, with the twist extending in from the edge by a distance L_{edge}. A value of $L_{edge} = 2.4$ nm is calculated from D_{DMI}, A_{ex} and the other magnetic properties of track using Eq. 1.11 and 1.13 [82]. The OOMMF simulation results also give a magnetization that depends exponentially on position, shown in Fig. 4.4, with the fit in the inset of that figure yielding $L_{edge} = 1.5$ nm, which is of the same order of magnitude. The small difference can be accounted for by the fact that demagnetizing effects are properly accounted for in the numerical simulation but neglected in the analytical formulae.

The sum of the radius of the skyrmion and L_{edge} is close to 10 nm. This means when the distance between the skyrmion center and track edge is smaller than ∼ 10 nm, the skyrmion starts to feel the influence of $\mathbf{f}_{edge}$. This force acts in the y-direction and so we see that the edge force will give rise to a positive term in v_x as given by Eq. 1.8. If this additional force is large enough it will overcome $\mathbf{f}_{transmit}$ (similarly to what is shown in Fig. 1.5(a) and (b)) and hence the skyrmion will start moving forward once

it reaches the track edge [152]. In a wider track, the skyrmion will take more time to reach the edge region where this force can be active, so we can expect a larger transient retrograde motion of the skyrmion towards the SW source before the forward motion sets in.

4.2.2 Retrograde Motion of Skyrmion with Enhanced Damping

Fixing the sample width at $w = 100$ nm, we ran a similar series of simulations in which we varied the value of α in the range [0.02, 0.06] with a 0.1 ns timestep. The resulting skyrmion displacements in the x-direction as a function of simulation time with varying damping constant are shown in Fig. 4.5 (a). When $\alpha = 0.02$, 0.03, or 0.04, we again see that the skyrmion initially moves backwards against the SW direction. The skyrmion only has a positive initial velocity when the track has $\alpha \geq 0.05$. As shown in Fig. 4.5 (b), the skyrmions still have a velocity in the y-direction due to the skyrmion Hall effect. The distance between the skyrmion and the edge when the skyrmion moves away from the SW source is smaller when α is stronger.

Assuming the skyrmion has the same R and T at the same position of each simulation, the strength of $\mathbf{f}_x$ only depends on the amplitude of the SWs. A larger value of α leads to stronger attenuation of the spin-waves owing to the shortening of L_{mag}, as described by Eq. 1.17. This reduces the force arising from the SW magnons for a fixed given distance between the skyrmion location and the SW source. Thus, it is easier for $\mathbf{f}_{\text{edge}}$ to overcome the negative terms of the $\mathbf{v}_x$ when the skyrmion is in a sample with larger α. Though a lot of micromagnetic simulations prefer to use the damping constant of CoFeB for CoB sample.[153–155] In the real experiment, the skyrmion will be expected to show a simple forward motion because α of real thin cobalt alloy samples is usually much larger than 0.05 [156]

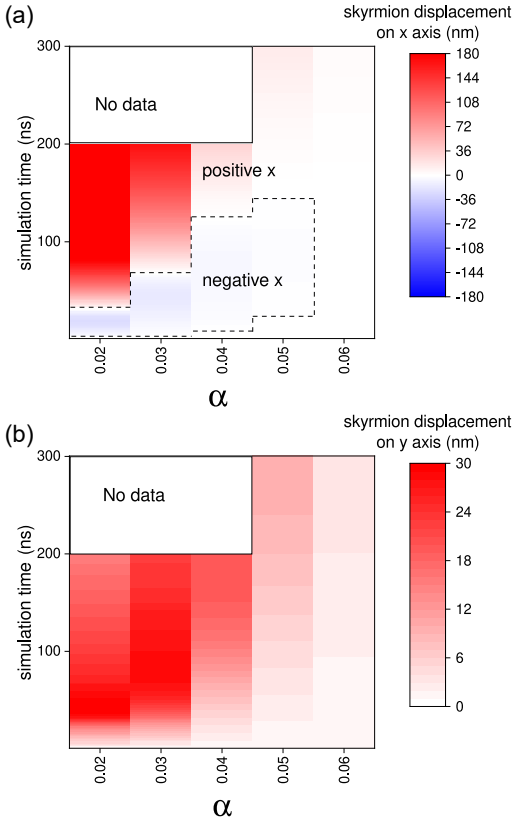

Figure 4.5: Time-dependent (a) x-direction and (b) y-direction skyrmion displacement in a $w = 100$ nm track for various values of the Gilbert damping constant in the range $\alpha = 0.02$-0.06. The region enclosed by the dashed line in (b) is where the skyrmion x-displacement is negative and the region enclosed by the black line doesn't have data since no simulations were done for those ranges of parameters.

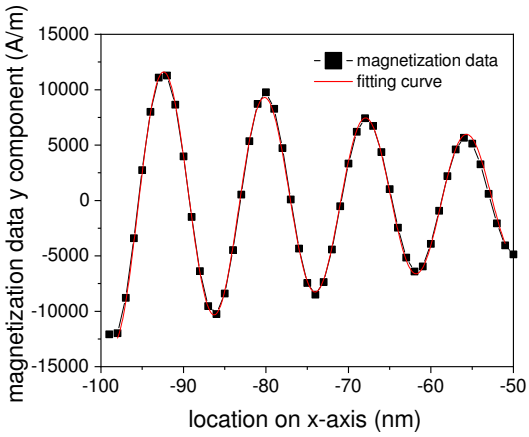

Figure 4.6: The y-component of magnetization at $[x_s - r_s, y_s]$ of skyrmion during an interval of 0.05 ns shows the spin wave along the propagation direction, the difference of magnetization data with and without skyrmion is the reflected spin wave.

4.3 Data Analysis and Results Discussion

4.3.1 The Magnetization Information from Data File

In order to determine the amplitudes of the SWs that are propagating in the track we simulated, we analyzed the data arrays output at each 5 ps timestep of the simulation, which contains the three components of the magnetization within each [1 nm, 1 nm, 0.4 nm] cell. An example of plotting the y-component of magnetization as a function of x was already given in Fig. 4.6, showing a damped sine wave. Simulations of the SW propagation both with and without the skyrmion on the track were carried out.

Analysis of the former yields the coordinates of the skyrmion location in the track as $[x_s, y_s]$. The y-component magnetization data from 50 nm long regions which have the same y location as the skyrmion but are 100 nm downstream from it, i.e. from x_s+100 nm to x_s+150 nm, were fitted with damped sine functions $M_y = M_{y_0} + I\exp\left(-x/L_{\text{mag}}\right)\sin(q(x - x_0))$, where I is the amplitude of the SW at the location [x_s+100 nm, y_s], q is the SW wavenumber, M_{y_0} is the amplitude offset and x_0 is a phase shift. The ratio between the values of I with and without the skyrmion is the transmission coefficient T.

Determining the reflection coefficient R required a different approach since plotting the spatial dependence on the waveform upstream of the skyrmion yields a complex

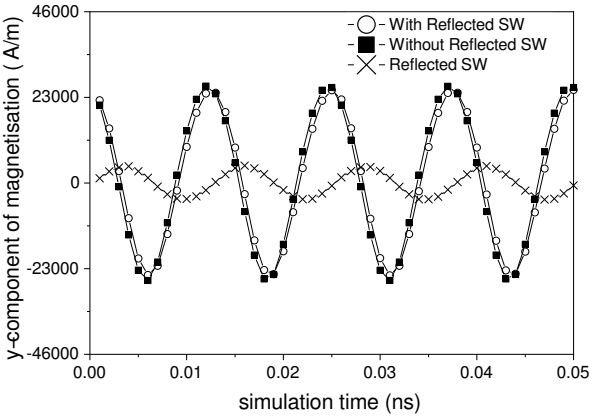

Figure 4.7: The y-component of magnetization at $[x_s - r_s, y_s]$ of skyrmion during an interval of 0.05 ns shows the spin wave along the propagation direction, the difference of magnetization data with and without skyrmion is the reflected spin wave.

interference pattern between the incident and reflected waves. We, therefore, select a point in space at location $[x_s(t) - r_s(t), y_s(t)]$, where r_s is the skyrmion radius, and the variation of the y-component of magnetization for a 1 ns time interval (200 data points) determined, again for the system with and without the skyrmion. An example is shown in Fig. 4.7. The spin wave propagation along the magnetic track without skyrmion initiation were simulated and set as pure incident waveform. From the simulation with skyrmion at the centre of the magentic track, the magnetization information obtained in the upstream area of the skyrmion contained pure incident wave and the reflected wave. So, by subtracting the pure incident waveform from the combined wave, we can yield the reflected wave. Both the reflected SW and SW without skyrmion on the track are fitted with sine functions $a\sin(\omega t + \theta)e^{-t/\epsilon}$ to yield their amplitudes a. The ratio between the amplitudes of the reflected SW and the incident SW yields the reflection coefficient R.

The relationship between the transmission coefficient T, reflection coefficient R and the distance between skyrmion and the sample edge d_{se} was shown in Fig. 4.12. In here, we provide plots of T, R, A_{sw} and skyrmion velocity as a function of simulation time for the first 60 ns simulation time in Fig. 4.8. We define the absorption $A_{sw} = 1 - T - R$.

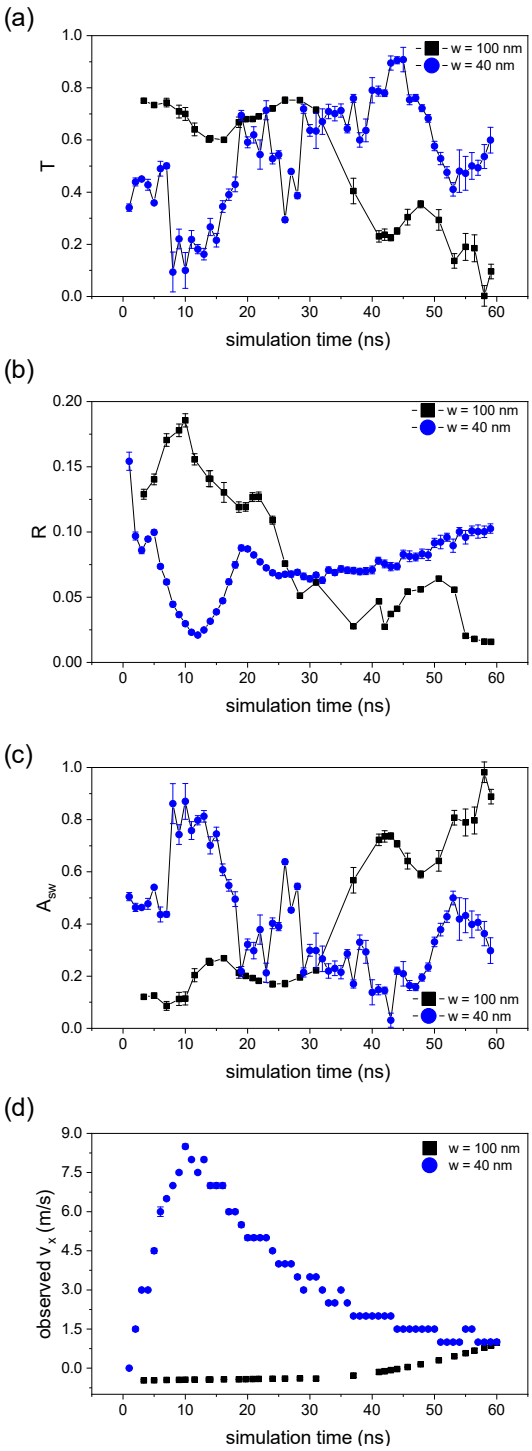

Figure 4.8: The time-dependent (a) transmission coefficient T, (b) reflection coefficient R and the absorption coefficient $A_{\mathrm{sw}} = 1-T-R$ for tracks with 40 nm and 100 nm width. (d) The observed skyrmion velocity from simulation as a function of the simulation time.

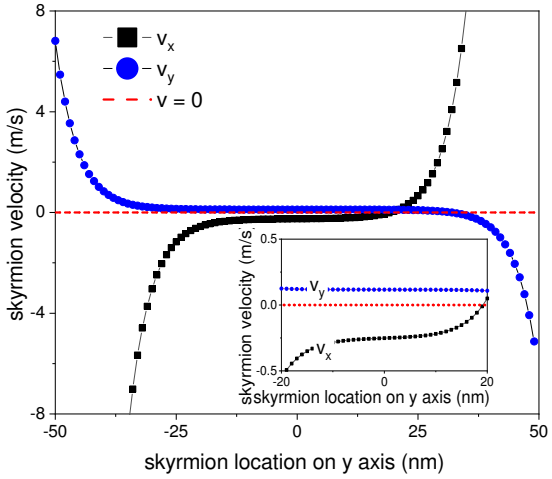

Figure 4.9: Initial skyrmion velocity decomposed into x and y components for different initial positions on the y-axis across a 100 nm wide track. Spin waves are propagating in the $+x$ direction along the track. Note that the initial velocity in the down track direction x depends on which half of the track the skyrmion starts in. The inset is a magnification of the central region of the main plot.

4.3.2 The Force Model of the SW Driven Skyrmion

As mentioned in the Section §1.6 and Eq. 1.8 above, When $|\alpha \mathbb{D} f_{\text{ref}} R| > |\alpha \mathbb{D} f_{\text{transmit}\|} T|$, then $f_x > 0$. So, $-4\pi f_y = -4\pi(T f_{\text{transmit}\perp} + f_{\text{edge}})$ will be more likely be positive when approaching the upper edge, and the longitudinal component of the skyrmion velocity will be $v_x > 0$. When the transmission of SWs is reduced, or the reflection of SW or α grows, the skyrmion will be more likely to move along the SW propagation direction.

In the work we present, the x component of the force on the skyrmion becomes

$$|f_x| = |(T f_{\text{transmit}\|} + R f_{\text{ref}}) e^{\frac{-x}{L_{\text{mag}}}}|. \tag{4.1}$$

Assuming that $\mathbf{f}_{\text{mag}}$ is fixed at a given x-axis location, the initial x and y components of the skyrmion velocity, calculated using Eq. 1.8 and 1.9, are shown in Fig. 4.9 for different starting positions across a 100 nm wide track, with values based on the simulation parameters described in Table 4.1 in the next section and fixed representative values of $R = 0.2$ and $T = 0.8$.

The results illustrate the importance of the gyrotropic motion and edge forces. For starting positions closer to the upper edge of the track (larger positive y), the stronger

the edge repulsion force pointing in the $-y$ direction will be on the skyrmion, and so the gyrotropic effect on skyrmion will lead to the skyrmion moving along the SW propagation direction $+x$. On the other hand, the closer to the lower edge, the stronger the edge repulsion force pointing in the $+y$ direction skyrmion will be, causing the skyrmion to move against the SW propagation in the $-x$ direction.

When skyrmion is initially located at $y = 20$ nm, the initial skyrmion velocity $v_x = 0$, whilst v_y is positive. Once the skyrmion moves on the y-axis, the balance between gyrotropic and dissipative terms is broken and the skyrmion will have a finite velocity on the x-axis.

For starting positions close to the top edge, the skyrmion has a negative velocity on y-axis arising from the strong repulsive force from the edge, but it will still have positive velocity on the x-axis. In the simulations we shall present in the following sections, the initial skyrmion locations are all set to be 0 nm, the center of the track, where initial motion is towards the upper edge. Thus we only ever observe the skyrmion going down and forward in narrow track after long simulation times after the skyrmion has been travelling along the upper edge for some time. As mentioned in Section §1.7.5, the way that spin waves interact with the skyrmion can also be described in terms of transmission (T) and reflection (R) coefficients. We found that these quantities will change with time as the skyrmion moves, so we can expect that the force from SWs is not only based on the spin wave amplitude but also these changing interactions of the SW with the skyrmion: we can expect that $\mathbf{f}_{\text{scatter}}$ should depend on T and R. We repeated the simulation in Fig. 4.5 with a finer timestep of 5 ps for $w = 40$ nm and $w = 100$ nm, set $\alpha = 0.03$, to study the spin wave transmission through and reflection from the skyrmion as a function of time.

As shown by the expression for the scattering force Eq. 1.15, the amplitude of the SW will exponentially decay along the track. The spin wave can be represented by picking out an in-plane component of the magnetization–here we use the y-component–which yields a damped sine function in space, an example of which is plotted in Fig. 4.10. The expected damping length is $L_{\text{mag}} \approx 139$ nm, based on a calculation using Eq. 1.17, close to the value of 101.7 nm obtained by fitting a damped sine wave to the M_y data.

In a similar manner, by extracting the in-plane magnetization data from the simulations (see §4.3.1 for details), and fitting a damped sine wave to them we can obtain the spin wave amplitude for any given region in the track. By selecting appropriate

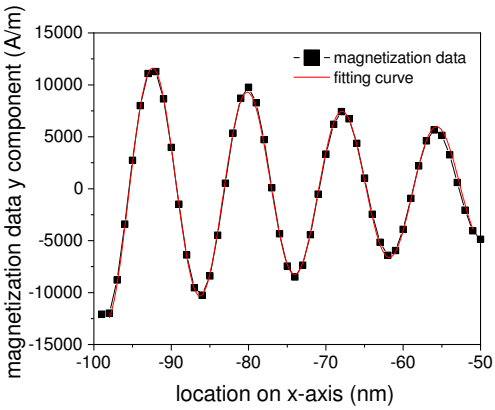

Figure 4.10: The y-component of magnetization shows a damped spin wave along the propagation direction. The red line is the result of fitting a damped sine wave of the form $M_y = M_{y_0} + I\exp\left(-x/L_{\text{mag}}\right)\sin(q(x - x_0))$, where I is an amplitude and x_0 is a spatial phase. The fit returns a value $L_{\text{mag}} = 101.7$ nm and wave vector $q = 0.52$ rad/nm. The range of x-axis locations shown here is in the area of the spin wave source at $x = -150$ nm and the starting position of the skyrmion at $x = 0$.

regions of the track, we have done this for three cases: the transmitted spin wave that has passed through the skyrmion, the spin wave reflected from the skyrmion, and, for comparison, the same frequency spin wave in the same region in an empty–i.e. no skyrmion–track. The attenuation caused by L_{mag} depends on the distance between the data collection region and the source of the spin waves. By comparing the transmitted SW amplitude in the presence of the skyrmion with that in an empty track we can obtain the transmission coefficient (T). Similarly, we can determine the reflection coefficient (R) for spin waves by comparing the amplitudes with and without the skyrmion in the region before the SWs reach it. Each process can be done at a certain simulation time.

In our simulations the skyrmion starts in the center of the track and so always moves toward to the sample upper edge because of the skyrmion Hall effect (see Fig. 4.9). We define the distance between the skyrmion center and the sample upper edge $d_{\text{se}} = \frac{w}{2} - y$. (This distance determines the exponential edge force term related to the top edge in Eq. 1.10, represented by the orange gradient in Fig. 4.11.) We show the time dependence of d_{se} for both the $w = 40$ nm and $w = 100$ nm track is shown in the

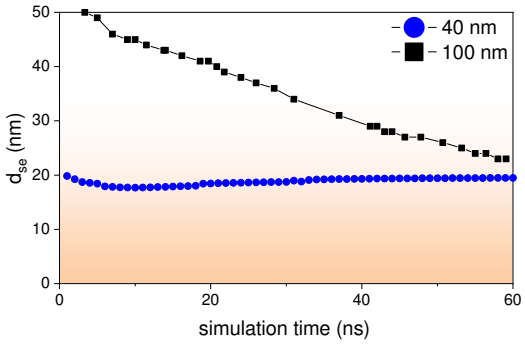

Figure 4.11: Time dependence of the distance between skyrmion center and the upper edge d_{se} for the $w = 40$ nm and $w = 100$ nm simulations. The orange gradient represents the region in which the skyrmion starts to experience a noticeable repulsive force from the upper edge.

Fig. 4.11. We find that the repulsion becomes too strong for the skyrmion to ever get closer than $d_{se} \sim 17$ nm to the edge. This leads to an effectively 'forbidden region' for the skyrmion for $d_{se} < 17$ nm, which we subsequently show with red shading.

Both T and R vary during the simulation because they correlate with d_{se}, as shown in Fig. 4.12. Only the data related to the skyrmions' first approach to the sample edge is plotted. (At longer times they rebound slightly from the edge, seen here for the $w = 40$ nm trace in Fig. 4.11.) As d_{se} shrinks, a drop in both (a) T and (b) R are seen. The inset graph shows a zoom of the $w = 40$ nm trace. For the $w = 100$ nm case, T initially takes a high value of ~ 0.7, and starts to drop once d_{se} falls below about 35 nm. Presumably owing to the proximity to the edge, T for the $w = 40$ nm case starts at a lower value ~ 0.5, but also drops rapidly as the edge is approached. T eventually falls to almost zero in both cases. Although not starting at such a high level, there is a similar finding for R, which also drops and reaches a value close to zero as the skyrmion comes to its point of closest approach to the edge.

These changes in the way that spin waves interact with the skyrmion suggest that it is not a perfectly rigid object with unchanging properties. To probe this further, we have measured the skyrmion diameter during each of our simulations, with the results shown in Fig. 4.13. Here we define the diameter as the distance between the extrema of the spatial derivative of M_z, as shown in the inset of Fig. 4.13. We can see that the skyrmion diameter shrinks as the edge is approached, presumably under the influence

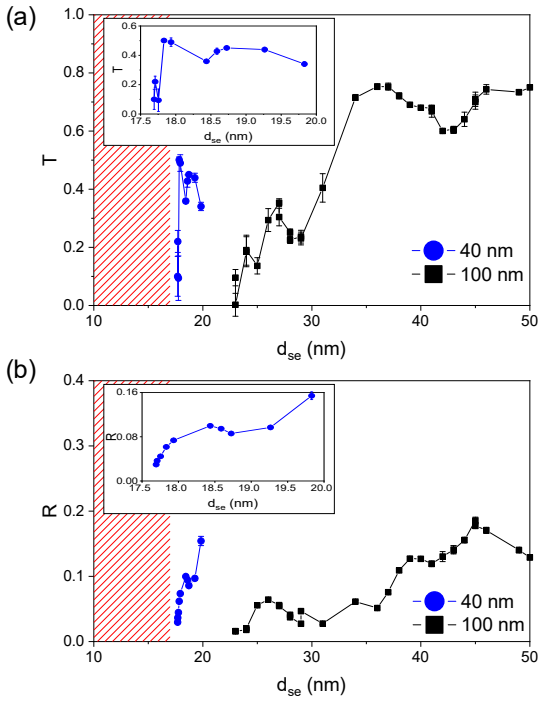

Figure 4.12: (a) T and (b) R of spin waves as a function of d_{se} for a simulation with w = 100 nm and w = 40 nm. The shaded red region is where the skyrmion cannot overcome the repulsive force edge force and so is effectively 'forbidden' in these simulations.

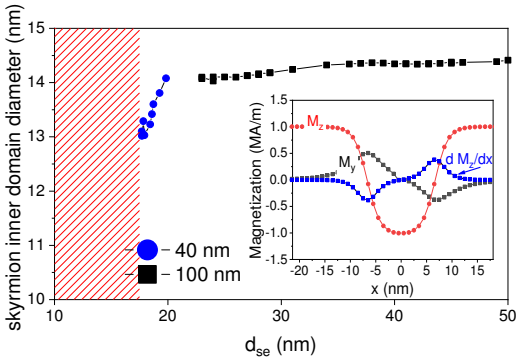

Figure 4.13: Skyrmion inner domain diameter as a function of d_{se} on 100 nm and 40 nm wide sample. The inner domain size is defined as the distance between the two extrema of $\frac{dM_z}{dx}$, as shown in the inset. The shaded red region is where the skyrmion cannot overcome the repulsive force edge force and so is effectively 'forbidden' in these simulations.

of the edge force. This change in skyrmion geometry could account for the change in the values of T and R.

We can see from Eq. 4.1 that the force f_x on the skyrmion is expected to have a term that is $\propto -T$ and another that is $\propto R$. Thus we expect these changes in the way that the skyrmion affects spin waves to lead to changes in its dynamics. In the insets of Fig. 4.14 we show the time dependence of v_x for each of our two simulations as red solid circles.

As shown in the inset graph of Fig. 4.14(b), for the w = 40 nm track, the skyrmion initially accelerates as it approaches the upper edge before 10 ns and later its velocity drops again as it moves away from that edge, based on the d_{se} data shown in the Fig. 4.11. In this case, the value of T drops when d_{se} is smaller than 18 nm as that edge is most closely approached. R also decreases similarly. Nevertheless, the skyrmion is is always in the region that has strong f_{edge}, owing to the narrowness of this track, which means it always moves away from the spin wave source with positive v_x.

Meanwhile, for the w = 100 nm track, from Fig. 4.5 and Fig. 4.14(a) we can see that the skyrmion's initial backwards velocity starts to drop at around 30 ns. The skyrmion then begins to move in the forward direction at 43 ns, corresponding to the time that d_{se} is $\sim$ 35 nm as shown in Fig. 4.11 and the drop in T takes place as shown in Fig. 4.12(a). The Thiele equation Eq. 1.8 and 4.1 shows that the transmission of spin waves will

give rise to a force that pulls the skyrmion towards the spin wave source owing to the transfer of angular momentum.

On the other hand, the force owing to linear momentum transfer from reflected spin wave magnons can give rise to motion along the spin wave propagation direction as shown in Eq. 4.1. Surprisingly, the reflection coefficient R is not equal to $1 - T$, and it has a similar time dependence to T. For 100 nm wide track, R starts at a value of $R \approx 0.2$ before declining quickly once d_{se} is less than 40 nm, as shown in Fig. 4.12 (b). Thus, this change in R cannot explain the change in direction of the skyrmion in 100 nm wide track, since R would need to rise in order to push the skyrmion away from the spin wave source by linear momentum transfer.

So far, in § 1.6 and Eq. 1.8, when $4\pi Q\mathbf{f}_{\text{edge}} + \alpha\mathbb{D}\mathbf{f}_x > 0$, $v_x > 0$. To compare this analytical prediction with our numerical simulation results, we insert Eq. 4.1 into Eq. 1.8 to obtain

$$v_x = \frac{4\pi Q(f_{\text{edge}} + T f_{\text{transmit}\perp}) + \alpha\mathbb{D}f_x}{(\alpha\mathbb{D})^2 + G^2}. \tag{4.2}$$

We then input the time-dependent values of T and R into the Thiele equation calculation and plot the results as black solid squares as a function of time in the insets of that figure.

We calculated the prefactor $\mathbf{f}_0$ of $\mathbf{f}_{\text{edge}}$ to be 2977 m/s by using Eq. 1.12, and $f_{\text{scatter}\perp}$ without any SW damping factor to be around 274 m/s. $L_{\text{edge}} = 2.5$ nm and $L_{\text{mag}} = 139$ nm, by using Eq. 1.13, and Eq. 1.17, respectively. $\mathbb{D} = \frac{d\pi^3}{2\gamma_{\text{DW}}}$[79], in which d is the skyrmion diameter and γ_{DW} is the domain wall width at the skyrmion edge.

The observed skyrmion velocity in the 100 nm wide track rises rapidly time, with a very good fit to an exponential (green line) for times before about 25 ns and after 45 ns, as shown in Fig. 4.14 (a). $\mathbf{f}_{\text{ref}}$ and $\mathbf{f}_{\text{transmit}}$ decay after 30 ns as the skyrmion has a velocity on the y-axis towards to the upper edge because of the gyrotropic effect from f_x, as shown in Fig. 4.9 and Fig 4.11. Since $\mathbf{f}_{\text{edge}}$ is exponential in skyrmion position y according to Eq. 1.10, the strongest force term in the Thiele equation is the exponentially growing $\mathbf{f}_{\text{edge}}$, which leads to exponential growth in the velocity along x through Eq. 1.8.

These predicted velocities based Eq. 4.2 are plotted against those directly observed in the simulations in the main panels of Fig. 4.14. The black scatter data are generally in good agreement with a line of unity slope, drawn in red: overall the predictions of inserting T and R into the Thiele formalism compare well with the velocity taken

directly from the simulation.

In Fig. 4.14 (a), there is excellent agreement between the two data sets for two regimes: (i) when the skyrmion is undergoing its initial retrograde motion for $v_x \sim -0.5$ m/s up to a simulation time of ~ 25 ns, and (ii) when the skyrmion is undergoing acceleration along the track edge at long simulation times after ~ 45 ns, when $v_x \gtrsim 0.4$ m/s. This shows that the underlying physical picture for v_{x1}, which only considers the strength of T and R on $\mathbf{f}_x$, gives a good description in these regimes. The agreement is poorer, but still fair, for intervening data points around the point where the skyrmion reverses direction, and potentially other physics may be at play there.

This leads us to propose a form for $f_x = T f_{\text{transmit}\parallel} + R f_{\text{ref}}$ and $f_y = f_{\text{edge}} + T f_{\text{transmit}\perp}$ that replaces f_{scatter}. However, using Eq. (1.8) to predict the skyrmion velocity means that the terms for the force arising from the absorption of spin waves are neglected since it is challenging to get a precise energy for skyrmion motion from the total absorbed SW energy. So, before 50 ns, the calculated result does not work well when the skyrmion is still far away from the edge and close to the SW source. When the skyrmion is close to the edge, $\mathbf{f}_{\text{edge}}$ is much stronger than the SW force in terms of its effect on the skyrmion velocity, and the calculated results are in good agreement with the ones extracted directly from the numerical simulation.

In Fig. 4.14 (b), there is also an excellent agreement between the two data sets. This is the case both when the skyrmion is accelerating and moving away from the spin wave source because of the short distance between skyrmion and upper edge in the initial state, and also when the skyrmion velocity is decreasing as it is pushed away from the upper edge. In the latter case, the skyrmion is gaining less $\mathbf{f}_{\text{edge}}$ and force from the spin wave because of the longer distances involved, and so the force balance leads a stable velocity of skyrmion.

Initially, the spin wave absorption coefficient $A_{\text{sw}} = 1 - T - R$ is small, but it rises markedly when T and R drop at the point where the skyrmion approaches the track edge. As shown in Fig. 4.13, the skyrmion size shrinks because of the repulsion from the edge [157]. Without the energy from the absorbed SW, the edge of the track causes the deformation of the skyrmion [158]. Also, the edge of the track might absorb the SW which presents the low transmitted SW amplitude at the downstream region of the skyrmion. The growing absorption coefficient is a promising candidate to fill the gap of the total force on skyrmion and reconcile the results of the Thiele equation calculation

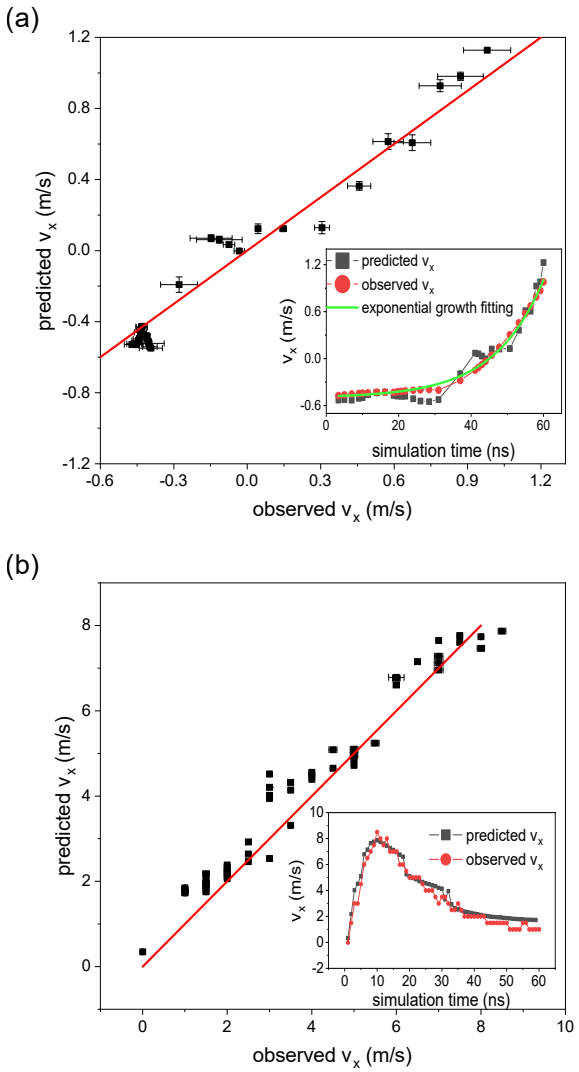

Figure 4.14: The relationship between skyrmion velocity predicted by the Thiele equation and the velocity observed in the numerical simulation of (a) 100 nm wide track and (b) 40 nm wide track. The data points can be compared with the red line of unity slope. Insets show the two velocity datasets each as a function of simulation time. The velocity observed in the w = 100nm numerical simulation was fitted with an exponential of the form $v_x = v_0 + v_t e^{(t-t_0)/\tau}$ shown as a solid green line. Here, v_0 is the initial velocity, v_t is a velocity prefactor for the time dependent part, and τ is a characteristic timescale.

with the actual velocity. The amount of absorbed spin wave magnon for changing skyrmion size and changing skyrmion motion cannot be calculated precisely, but the reflection and transmission of spin waves and the interaction between skyrmion and the sample edge are enough to explain the transient retrograde motion of skyrmion.

If the damping constant is larger than 0.03, the SW amplitude will attenuate more rapidly and the term f_y in Eq. 1.8 will more easily overcome the negative term of f_x. This fact can explain the shape of the contour of α dependent skyrmion displacement in Fig. 4.5. For wider samples, the skyrmion will need a longer time to reach the region where the edge forces are significant, and so further negative displacement will show up in the contour plot of the sample width-dependent skyrmion displacement in Fig. 4.3.

4.4 Conclusion

In conclusion, we have studied the spin-wave driven motion of skyrmions in a nano-scale track by means of time-dependent micromagnetic simulations and found a range of conditions where there is a transient retrograde motion of the skyrmion. Our results show that the skyrmion will have retrograde motion towards the spin wave source at the onset of its movement when the track has a large enough width and a low damping constant, but the skyrmion always moves away from the SW source at long simulation times. We cross-checked the simulated skyrmion velocity with the results of the Thiele equation and find qualitatively similar skyrmion motion from the calculation, but also find that only using reflection and transmission data cannot give a fully quantitative relationship between calculated velocity and simulated velocity. The gyrotropic term in the Thiele equation is not negligible, and the repulsive force from the sample edge also affects the skyrmion velocity by this means. We suggest that also considering the absorption of spin wave magnons is a possible way forward in the future.

The simulation results give a possible motion of skyrmion that might be observed in future experiments. The force from the track edge is a potential means to adjust the skyrmion motion. A higher damping sample (e.g a CoB alloy thin film [156]) will have a shorter retrograde distance than a low damping sample ($\alpha < 0.05$ for simulation magnetic properties), as can be seen from Fig. 4.5. Moreover, if the initial position of a skyrmion in y is not well-controlled then the motion along the x-direction will not be

deterministic, since the time taken for the skyrmion to reach the near-edge region and experience the edge forces will be unpredictable.

The work in this chapter has been published [159].

Chapter 5

Experimental Observation of Domains and Skyrmions Generated by Varying OOP Magnetic Field with Magnetic Force Microscopy

5.1 Introduction

In the experimental part of this project, MFM is the primary characterisation method to measure the inital and final states of the magnetic texture dynamics. The phase channel of Magnetic Force Microscope parallel scan can represent the force between the magnetic domains and the magnetic covered tip by the reflection or deflection of the laser on the tip [160]. This chapter shows the optimisation methods to obtain MFM signals. Different out-of-plane magnetic fields can generate magnetic textures from both the sheet and narrow track samples. Also, skyrmions can be formed by the out-of-plane magnetic fields close to the saturation field. In the first step, we must ensure the MFM can observe the magnetic texture clearly before we start the other fabrications for another layer on the chip for the printed circuit board.

5.2 MFM Measurement with Different Lift Height, Drive Amplitude and Scan Orientation

To let the tip work with good performance, it needs to be tuned once the laser sitting on centre of it with maximized reflection signal.The drive frequency and drive amplitude obtained from the tuning will affect the vibration of the tip and the strength of the AFM signal. This step was discussed in Section §2.3.4 and §2.3.5. After tuning the magnetic tip, the MFM signal will present in the phase channel of the second parallel scan, which is also the Nap mode for Asylum AFM instrument of Asylum Research Oxford instrument company, during the measurement. The Phase channel is selected to show the MFM signal because the phase channel primarily represents the changes in the phase of the tip oscillation due to the interactions between the magnetic domains and the tip. Meanwhile, the amplitude channel represents the amplitude of the tip vibration. The Nap Height (the distance between the first AFM tapping measurement and the second parallel scan, or lifting height for generic pieces of equipment.) of the Asylum system is the main parameter that needs to be adjusted to obtain a good MFM signal and noise ratio.

$[Pt/Co_{68}B_{32}/Ir]_5$ sample is a good calibration sample. Because of the demagnetization pattern shown in Fig. 3.8, maze or lower-density worm-like domains are expected in different out-of-plane fields. Adjusting the parameters of MFM measurement can

improve the quality of MFM figures. As shown in Fig. 5.1 (a), when the Nap Height is 100 nm, the Nap Phase channel still presents the $Pt/Co_{68}B_{32}/Ir_{10}$ sheet sample surface's topographic structures. The dark areas in Fig. 5.1 (a) are the structural defects on the surface and the broken part caused by the metal tweezer. According to the power law of the AFM, the tip-sample force is nonlinear:

$$F_{\mathrm{ts}} = -\frac{\iota}{d_{\mathrm{ts}}{}^{\varkappa}}, \tag{5.1}$$

where ι is the magnitude of the interaction phenomena such as van der Waals forces, d_{ts} is the tip-sample distance, the power $\varkappa$ is the profile of the force. In Lai's paper, the power law dependence of the force on distance is proven by the AFM force [161, 162]. Comparing Fig. 5.1 (a) to (c), with the increasing Nap Height, the AFM signal from the structural defects on the sample decreases, and the area of the dark structural defects decreases. Also, the decreasing of data ranges from Fig. 5.1 (a) to (f) is nonlinear. The comparison between Fig. 5.1 (a) and (d), the data scale drops from [61.9°, -18.0°] to [0.29°, -0.68°] and the MFM signal starts to appear. The magnetic texture did not look like the maze domain that fully covered the area we measured. This might because this sample got some scratches in three years usage and the pattern cause the rectangular shape of the area of domains. The changing of the data scale shows that the AFM signal is strong but short-range, as expected for van der Waals forces. Meanwhile, the MFM signal is long-range and only has a good signal and noise ratio when the tip is high enough. Different samples with different roughness will need different Nap Height settings. The stronger magnetic interaction between the tip and sample will allow the tip to go higher in the second parallel scan. From the comparison between Fig. 5.1 (d) and (f), the edge of the domains gets blurred with the increasing Nap Height. So, we also need to maintain the balance between the distance that can have an MFM signal apart from the AFM signal and the distance that is too far away to have a large enough MFM signal.

The drive amplitude is another parameter that will affect the distance between the tip and the sample surface. The drive amplitude sets the initial amplitude of the vibration of the tip; a larger drive amplitude results in a larger tip vibration amplitude, so the lowest point of the parallel scan will be closer to the sample surface when the Nap Height is fixed.

In Fig. 5.2 (a) and (b), both of the images show the MFM signal. The clear MFM signal will appear when the smallest distance between the vibrating tip and the sample

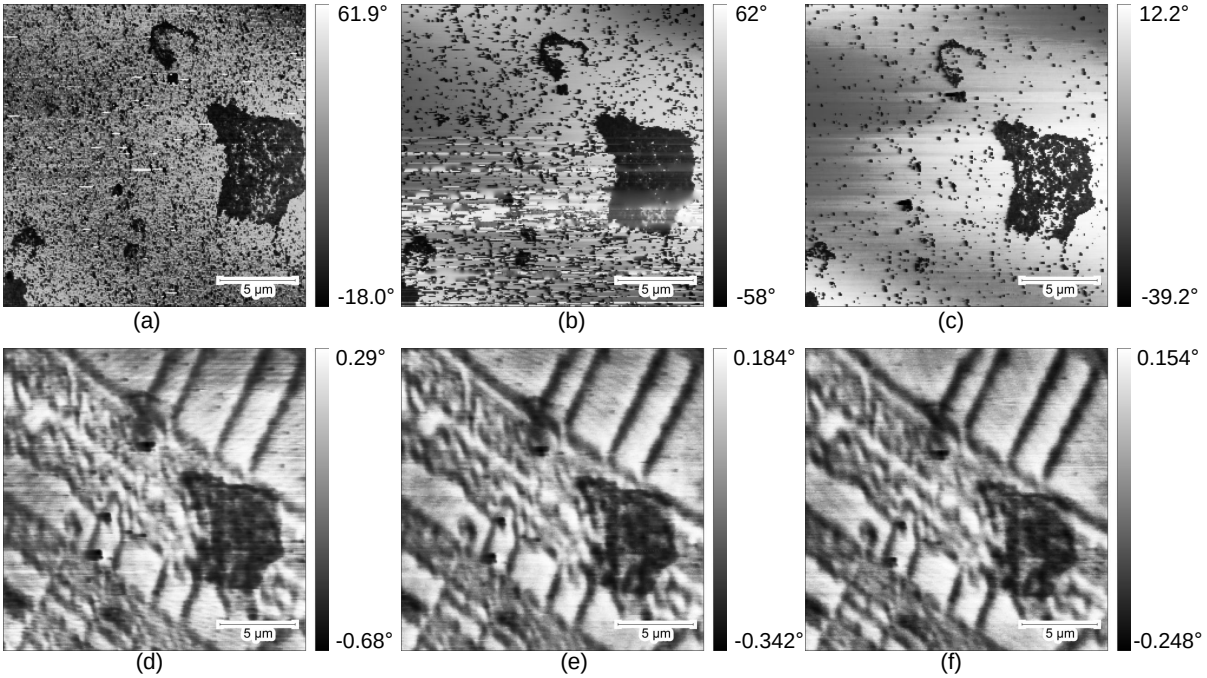

Figure 5.1: The Nap Phase images of the magnetic $[Pt/Co_{68}B_{32}/Ir]_5$ sample in the same area but increasing lift height for the parallel scans: (a) 100 nm, (b) 130 nm, (c) 160 nm, (d) 190 nm, (e) 220 nm, (f) 250 nm.

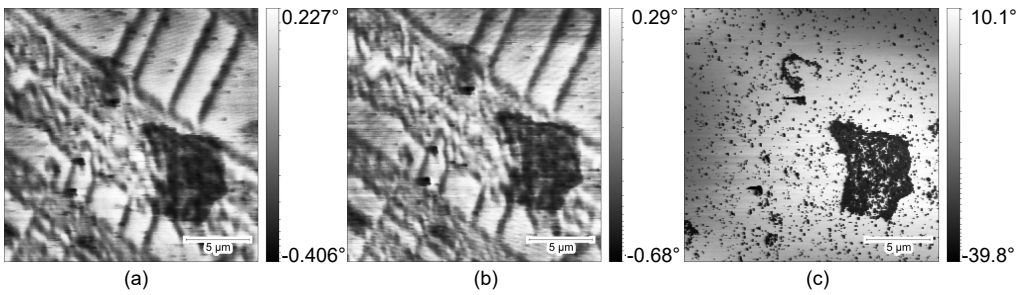

Figure 5.2: The Nap Phase images of the magnetic sample in the same area and fixed Nap Height but increasing driving amplitude: (a) 360 mV, (b) 400 mV, (c) 440 mV.

surface remains within [190 nm, 250 nm]. When the amplitude grows to 440 mV, the lowest point of the vibrating tip goes down to the point that the AFM signal is too strong to let the MFM signal have high contrast in a small data range.

As mentioned in the beginning, the drive frequency is also important to the meas-

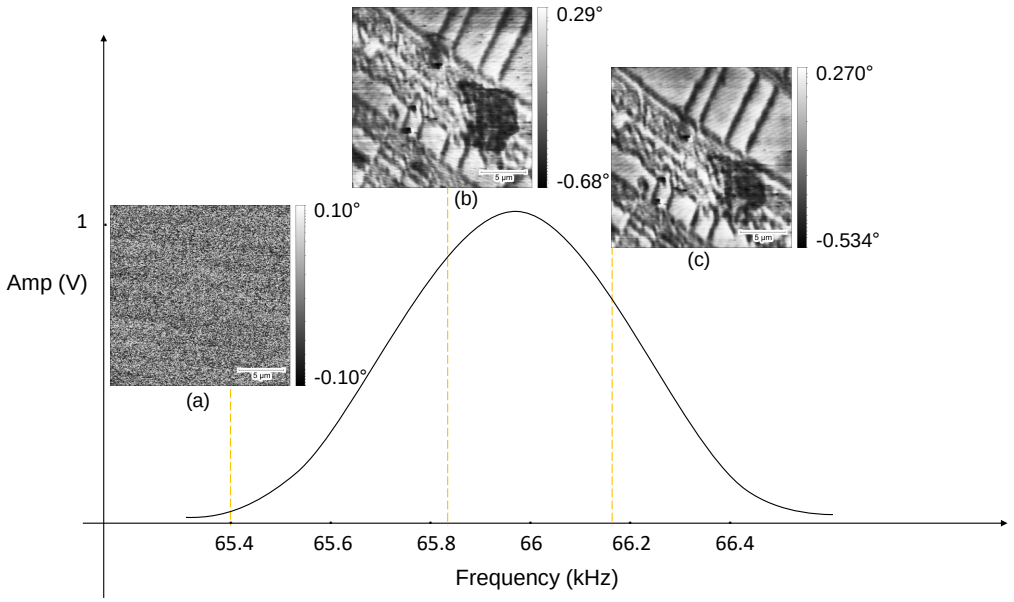

Figure 5.3: The Nap Phase images of the magnetic sample in the same area and fixed Nap Height and Drive Amplitude but different driving frequency on the sketch of typical tuning result: (a) 65.40 kHz, (b) 65.82 kHz and (c) 66.18 kHz.

urement. The reason we have the drive amplitude offset from the central peak amplitude is to optimise the stability and quality of the imaging process. But if we have a frequency far away from the tip resonance frequency, such as Fig. 5.3 (a), we can only obtain noise. Both Fig. 5.3 (b) and (c) can show the MFM signal because the offset value is reasonable.

5.3 Calibration for MFM Measurement with Varying Field

The VFM section is a small stage that can be mounted on the normal AFM scanner. The varying field strength is generated by a rotatable rare earth magnet, and the magnetic flux is generated by the soft iron armatures and pole pieces perpendicular to the sample surface.

As shown in Fig. 5.4(a), when the angle of the permanent magnet is 0° or 180°,most of the magnet's flux will be directed to the sample surface and the field applied on the sample is minimum. When the magnet angle is 90°, the most magnet flux will be generated to the sample surface, and the strength of the OOP field is maximum [163].

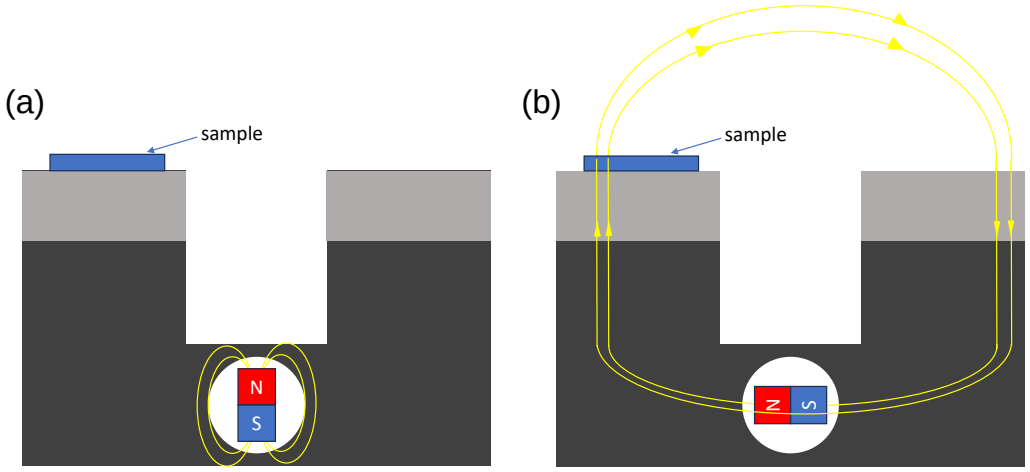

Figure 5.4: Schematic of side view when the angle of the magnet is (a) 0° or 180° and (b) 90° or 270°.

During the setup, we found the VFM section had a non-uniform offset out-of-plane field when both the power supply and the control signal box of the VFM section were not connected. The non-uniform offset still existed when all the cables were connected, and the power supply was on. With a few tests of the magnetic field ramping from 200 Oe to 0 Oe, the offset field when the sensor showed 0 Oe was fixed at the same position. So, a calibration measurement for the offset field is necessary every time before the measurement. By sticking the Gaussmeter sensor in the middle of the magnetic pole piece and parallel to the MFM stage, the actual field can be measured. As shown in Fig. 5.5, there is a -200 Oe field offset when the field setting and computer sensor record is 0 Oe. However, the relationship between the setup field on the computer and the actual field is linear with an offset. If we placed the sample on the other pole piece, the the slope of the linear fitting will be negative since the field is antiparallel on the other pole piece, as shown in Fig. 5.4 (b).

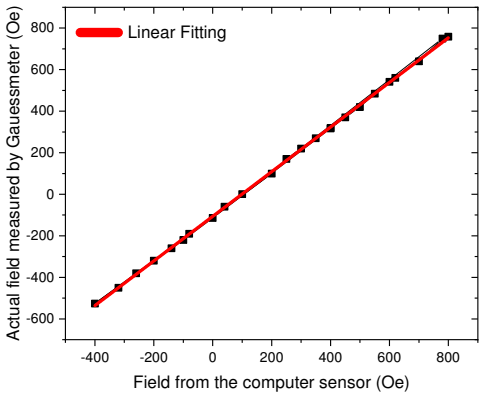

Figure 5.5: The linear relationship between the actual field and the field recorded by the computer sensor.

5.4 MFM Measurement with Varying Fields on Both Sheet Sample and Track Sample

5.4.1 MFM Measurement with Varying Field on Sheet Sample

Since the maze domains can be observed from n=5 sample by the Kerr microscope in §3.0.4, the sample with 20 [Pt/CoB/Ir] repeat stacks was used as a calibration sample since it can also provide maze domain pattern. The magnetic field tuning within the sample hysteresis loop is expected to tune the density of the maze domains or even stabilise isolated domains or skyrmions [37, 65].

Fig. 5.6 shows a series of MFM images collected from part of the hysteresis loop of a $[Pt/CoB/Ir]_{20}$ sample, with the largest out-of-plane magnetic field value being 250 Oe. The first image at 0 Oe field at the bottom left corner of Fig. 5.6 shows the maze domain because of the magnetostatic flux closure and the natural tendency to reduce magnetostatic energy [164]. With the increasing out-of-plane field applied on the sample surface, the maze domain density will decrease. The domain magnetisation is opposite to the applied field, so when the sample is fully saturated, we should only see the structural defects on the sample and bright background compared to the dark magnetic patterns. Before the saturation, the domains will break into fragments because some spins align with the perpendicular orientation by the stronger and

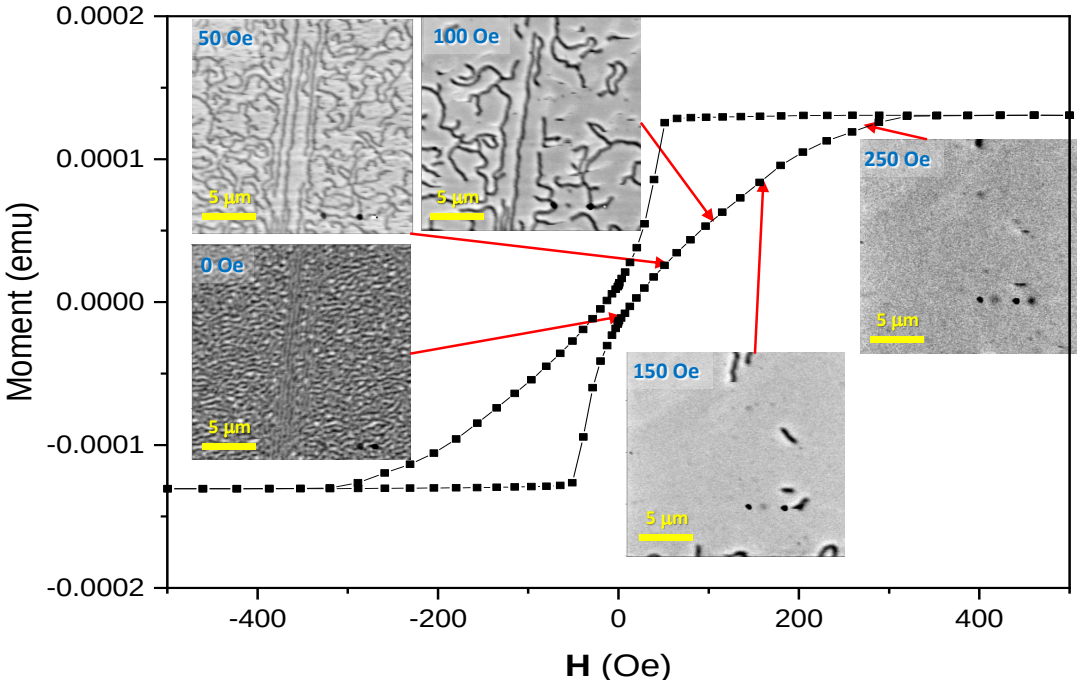

Figure 5.6: The MFM figures of $[Pt/CoB/Ir]_{20}$ sheet sample on the sample hysteresis loop, the measurements started from 0 Oe to 250 Oe.

stronger applied field, as shown in the subfigure of 100 Oe of Fig. 5.6. Continuing the increase of the field, the length and size of domains will go down to worm-like domains as shown in the subfigure of 150 Oe of Fig. 5.6. Just before the applied field reaches M_s, the worm-like domains decrease in length and diameter or collapse into some skyrmions or disappear as shown in subfigure of 250 Oe of Fig. 5.6.

5.4.2 MFM Measurement with Varying Field on Track Sample

In this project, we focus on the motion of the domains and skyrmions on the narrow track, so the MFM images acquired as the sample is taken around part of its hysteresis loop of $[Pt/CoB/Ir]_{20}$ narrow track are also collected before the sample is stuck on the printed circuit board (PCB).

Similarly, as the out-of-plane magnetic field increases, the maze domain density decreases and eventually deforms into worm-like domains until shrinking into skyrmions, as shown in the subplots on the right-hand side of the hysteresis loop in Fig. 5.7.

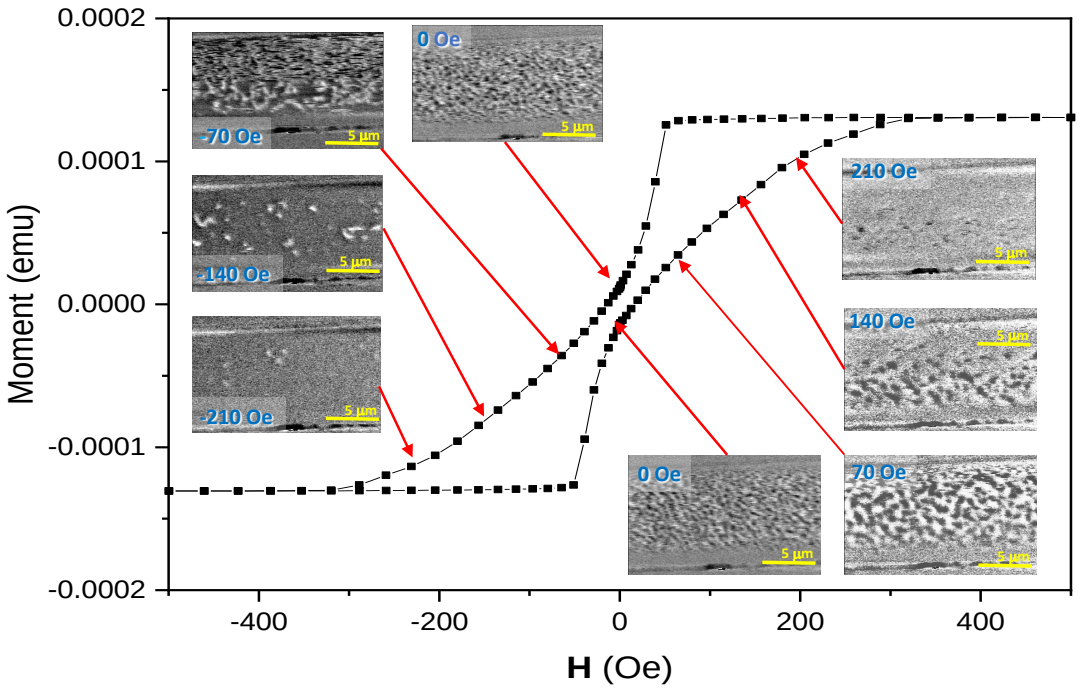

Figure 5.7: The MFM figures of [Pt / $Co_{68}B_{32}$ / Ir]$_{20}$ narrow track sample on the sample hysteresis loop, the measurements started from 0 Oe to 210 Oe then dropped to 0 Oe to -210 Oe.

The sample will be magnetised in the opposite direction when the strong anti-parallel out-of-plane field is applied. The domains which have the opposite spin magnetisation direction to the magnetisation of the sample during [-210 Oe, 0 Oe] measurement will be shown as bright white maze domains in left-hand-side subplots of Fig. 5.7 when the magnetisation of the tip is same as the domain magnetisation during [0 Oe, 210 Oe] measurement.

Unfortunately, we failed to observed similar magnetic texture on the samples after some fabrication steps accompanied with heating. During the fabrication of the sample, the diffusion of thin $Co_{68}B_{32}$ with few angstroms thickness after the process in the thermal evaporator or RF sputtering because of over 40 minutes of evaporation over 80°C is strongly suspected, which can be regarded as an annealing diffusion [165, 166]. In this case, the difference between the magnetic layer thickness of each stack will decrease the sample MFM signal amplitude and coercive field, which makes the measurement contrast not good as the Fig. 5.7 and Fig. 5.6. Also, after sticking the

sample on the PCB and connecting it to the breakout box to provide current into the Pt heater, the mechanical noise from the wires dragging or vibration from the building was greater and still needs to be reduced. The methods to optimise the MFM signal during and after MFM measurement will be discussed in Chapter 5 Section §5.5. The step will affect the MFM measurement from sample fabrication will be discussed in Chapter 6 Section §6.5. The magnetic characteristics of materials will change within a temperature range from room temperature to the Curie temperature. Both theoretical simulation and experimental observation pointed out that the hysteresis loops of identical samples show variations at different temperatures due to the demagnetization energy change. The saturation magnetisation and coercivity decrease when the temperature increases as shown in Fig. 3.5.[167, 168] Also, the magnetic texture will be affected by the temperature, with the higher temperature, the skyrmion nucleation field will be smaller.[168–170] If the temperature is non-uniform on the sample, different phases of the magnetic texture can show at the same time with the same external magnetic field applied. Since the heaters were built at the end of the track in this project, the MFM measure area should be close to the heater to have seperated domains or even skyrmions with smaller field. The domains renucleation field with different temperature gradient application will be different.

5.5 Optimisation of the MFM Measurement

5.5.1 MFM Measurement with Different Magnetic Coated Tips

As mentioned in the last section, the magnetic signal will decrease after the high-temperature sample fabrication processes. High temperatures can cause magnetic domains to become more disordered, which may result in lower coercivity. We found the magnetically covered tip with a hard magnetically coated layer might affect the spins of the edge of the opposite magnetisation domains, which shows blurred domains. To minimise the magnetic interactions between the MFM tip and the sample that will cause the domain shape morphing, the Asylum Research special designed low-coercivity tips are recommended.

The low coercivity tip is designed for a low coercivity sample and covered by a low coercivity magnetic layer. Low coercivity tips magnetization direction prefers to align with the external magnetic field. At the same time, the low coercivity sample

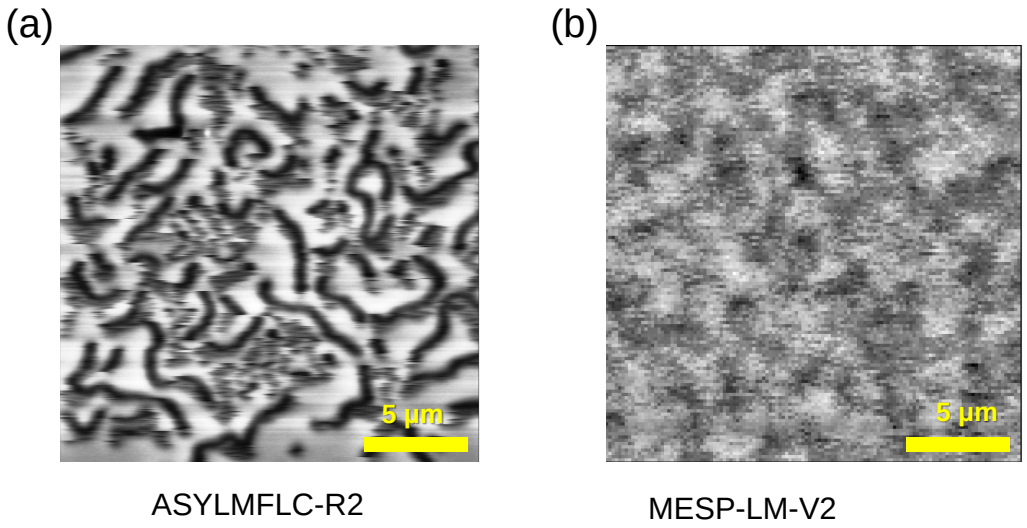

Figure 5.8: The MFM measurement of sample at remanence with magnetic field around 70 Oe after SiO_x sputtering with (a) ASYLMLC-R2 and (b) MESP-LM-V2 tip.

requires low magnetic field measurement. These ensure that the magnetization state of the tip stays the same during the MFM measurement process, which could otherwise affect the accuracy and reliability of the data. Low coercivity tips are more sensitive to weak magnetic interactions. The less interaction between the domains and the tip can provide a more accurate magnetic pattern [171]. In Fig. 5.8 (a), the tip model ASYLMLC-R2 is from the Asylum company, the tip is covered by the permalloy with the coercive field around 10 Oe and magnetic moment of 1×10^{-13} emu. A medium magnetic moment in the tip is advantageous because it provides sufficient sensitivity to detect the magnetic fields from the sample without being so strong that it disturbs the sample's own magnetic state. The tip from Bruker company model MESP-LM-V2 provides blurred domains as shown in Fig. 5.8 (b). MESP-LM-V2 tip has a nominal coercivity less than 400 Oe but not as small as 10 Oe; its magnetic moment is 3×10^{-14} emu. The images show that the tip designed for low coercivity samples can have better performance and reduce the risk that unwanted magnetic interactions will 'wipe away' the magnetic texture, as could occur by using magnetically harder coated tips [172, 173]. The magnetic textures in Fig. 5.8 (a) and (b) have different densities and sizes because the measured area is not precisely the same after changing the tips; the magnetic field

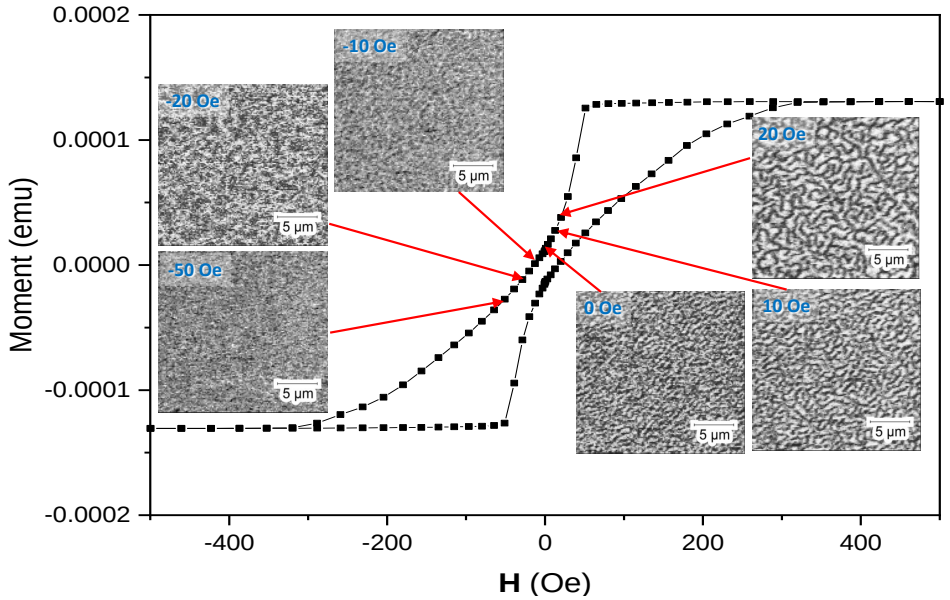

Figure 5.9: The MFM figures of $[Pt/CoB/Ir]_{20}$ sheet sample, the measurements by LM-V2 MFM tip started from 20 Oe to -50 Oe.

is non-uniform on the sample, so the texture will not be similar but still showing the maze domains.

5.5.2 MFM Measurement with Opposite Magnetisation

Sometimes the sample magnetic pattern might not be as clear as Fig. 5.7 when the magnetisation of the tip is the same as the worm-like domain magnetisation direction by using the standard MESP-LM-V2 MFM tip (which properties are mentioned in §5.5.1) for measurement or the magnetic layer on the tip becomes worn because touching structural defects so many times. In Fig. 5.9, the measurement of the sample in 10 Oe and 20 Oe is clear. The tip is not magnetised on opposite direction by the flipped magnetic field -20 Oe since the tip coercivity field is larger than that. When the field is close to the tip coercivity field, the magnetic moment of the tip is close to 0 emu, so the white magnetic pattern has a low contrast to the background as shown in Fig. 5.9 because the interaction between the tip and the magnetic layer is not strong enough to represent the vibration of the tip like Fig. 5.7.

In order to have high contrast MFM images with negative field applied, the tip needs to be remagnetized and have large enough moment. We set the out-of-plane

field large enough to saturate the sample which also happens to flip the magnetisation of the tip as the 400 Oe in Fig. 5.10. Then, the magnetisation orientation of the tip and the domains are opposite to each other, so the domains are dark in the background as shown in Fig. 5.10 and more apparent than the bright white domains Fig. 5.9.

The tip needs to be tuned after loading every time. The retuning will change the defined drive amplitude and drive frequency, affecting the tip performance. Reloading the tip also means the user needs to find the interested area again on microscale patterned sample, which is hard on the sample without a unique structural mark or pattern. In this section, we suggest remagnetizing the tip with a strong and direction-alternative magnetic field from the VFM section instead of the default magnetizer, which needs to unload the tip. This allows the user to observe high-contrast MFM images from different magnetized direction samples with standard coercivity tips.

5.5.3 MFM Measurement with Different Parameters and Noise Cancellation

As mentioned in §5.4.2, the unstable PCB on the VFM section will affect the signal-to-noise ratio since the interaction from the lab environment will transfer from the cables to the PCB. The motion of the PCB causes the lift height of the MFM measurement to always change. The unstable lift height will give rise to the noise during the measurement. The PCB is stuck by double-sided tape on the pole piece, as shown in Fig. 5.11 (a). To reduce the noise from the environment and avoid the sample being dragged by the cables and the breakout box, the cables are as thin and flexible as possible but strong enough to be soldered and twisted into a spiral.

In most AFM systems, a feedback loop keeps the tip and sample interaction fixed during the scan. The interaction signal amplitude will be observed and compared with the user-defined amplitude setpoint. The difference between measured amplitude and setpoint is referred to as the error. This error is scaled by the gain and controlling the feedback loop by changing the distance between the tip and sample. When the gain value is small, the feedback loop system will not respond fast to change along with changes in the sample topography. In this case, the motion of PCB will not be a concern and reacted too much to the system when the gain is small. Meanwhile, the amplitude of the noise of PCB motion will be decreased and the MFM signal can be more significant in the result.

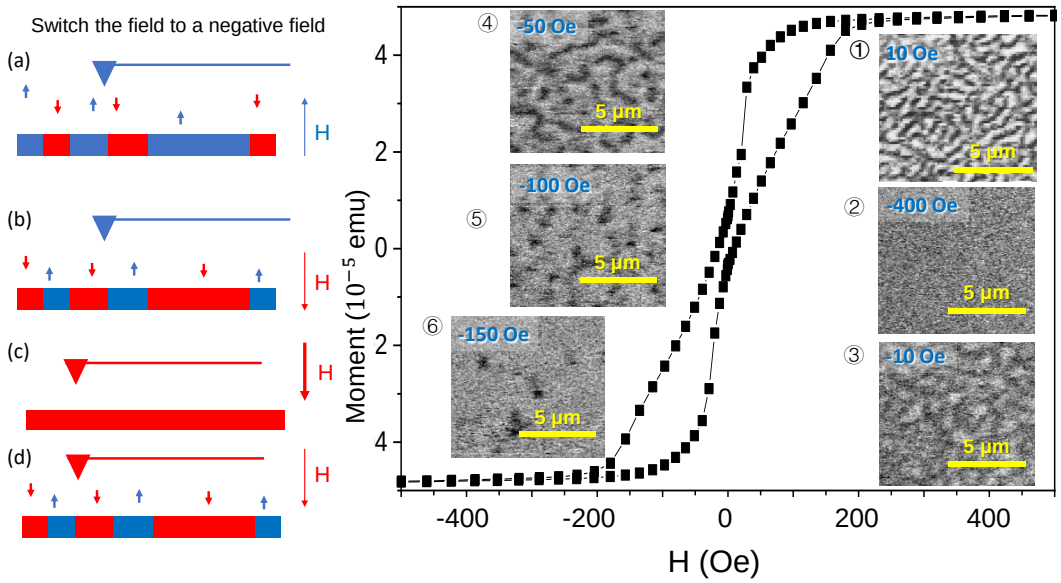

Figure 5.10: The MESP-LM-V2 tip magnetization direction (a) aligns with the positive OOP field, which can have images similar to subplot ①. (b) The negative magnetic field is not large enough to flip the magnetization of the tip. (c) The strong negative field saturates the sample and changes the magnetization of the tip, and the MFM image is similar to subplot ②. (d) The tip stays in its magnetization state with a reduced negative field. The domains appear again, the MFM images are similar to subplot ③ – ⑥. The *M-H* loop was not measured as the process of VFM measurement, the information it provides is about the coercivity of the sample.

A larger gain will be more sensitive to sources of noise. In Fig. 5.11 (b-d), the smaller gain value will allow the measurement result to have a smaller ratio between the noise signal from the vibration of the PCB and the MFM signal from the domains.

The setpoint is the deflection signal amplitude the user wants to maintain during scanning. When the user increases the setpoint during the scan, the contact between the tip and sample is softer than a small value. The user must manually adjust the tip-sample distance to maintain the desired signal. The drive amplitude needs to be increased to obtain a large enough signal, or the lift height of the parallel scan needs to be decreased to maintain the updated desired signal. The larger setpoint will make the system exert a larger drive amplitude. At the same time, the MFM system becomes less sensitive to small fluctuations in the environment. So, in Fig. 5.11 (e-g) the figure

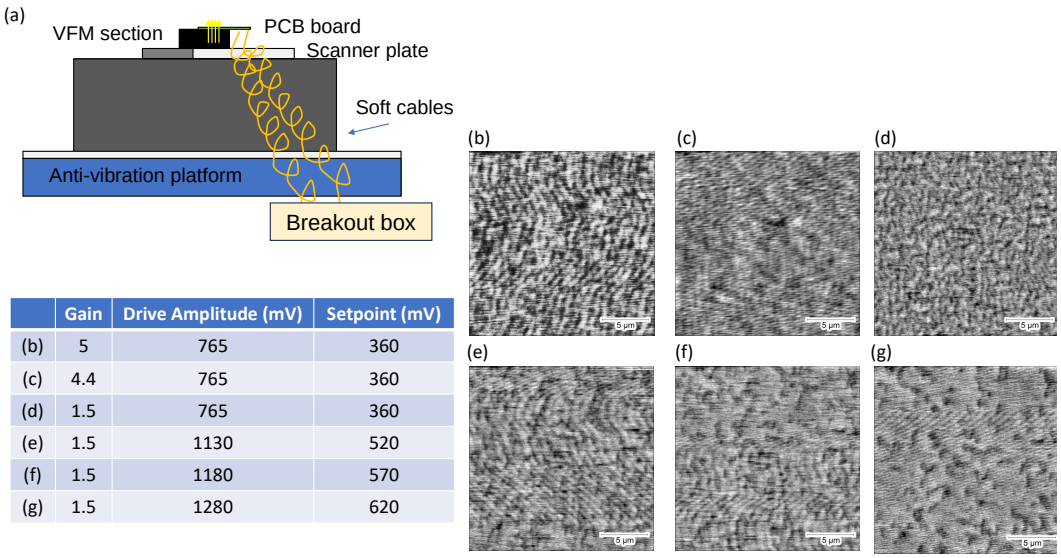

	Gain	Drive Amplitude (mV)	Setpoint (mV)
(b)	5	765	360
(c)	4.4	765	360
(d)	1.5	765	360
(e)	1.5	1130	520
(f)	1.5	1180	570
(g)	1.5	1280	620

Figure 5.11: (a) The side view of the equipment with PCB attached. (b)-(d) The MFM images were measured with decreasing Gain value. (e)-(g) The MFM images which are measured with decreasing Setpoint and growing Drive Amplitude.

has less noise with larger setpoint. Fig. 5.11 (g) is where the magnetic texture can really be seen.

Another way to partially remove the noise from the environment is using the fast Fourier Transform (FFT) and setting a filter to block the high-frequency noise. The noise has a quite well defined spatial frequency and so this is likely to be an effective strategy. The FFT image of Fig. 5.11 (e) is shown in Fig. 5.12 (b). To reduce the stripe noise in Fig. 5.12 (a), the FFT is applied, and the black part of (c) is the channel will be blocked in (b). The structure of the filter in (c) is obtained by taking the high-frequency part in the FFT image. The higher frequency pixels have brighter colour in grey scale images. The wanted grey values on the grey scale image can be picked up by the threshold adjustment function built into the software ImageJ. The reverse FFT result of (b) after blocking the noise channel is shown in (d). After blocking the noise channel, the Fig. 5.12 (d) looks similar to the Fig. 5.11 (g) which has less noise than Fig. 5.11 (e). This method helps us reduce the noise when the adjustment of parameters can not improve the signal and noise ratio significantly.

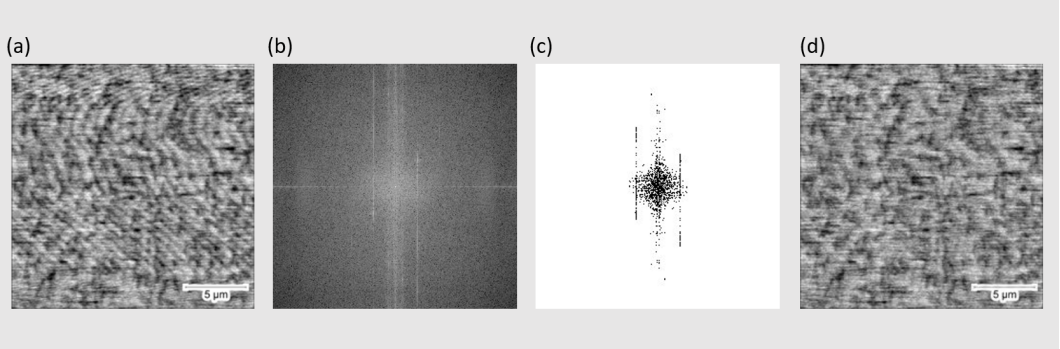

Figure 5.12: (a) Original MFM image. (b) Fast Fourier Transform of the original MFM image. (c) The filter blocks the noise channel. (d) The MFM image after the noise filtering process.

5.6 Conclusion

The performance of the MFM measurement highly relies on precise tuning the magnetic tip to its resonance frequency and set the parallel scan height can balance the long range magnetic force and van der Waals forces. Different magnetic tips can achieve different contrast of the domains from different samples. The tip model for low coercivity magnetic sample is recommended to use once the low frequency model fails to detect the magnetic signal. After all, MFM is still a reliable method to measure small size magnetic textures but need optimisation from both measurement parameters, MFM tips and data analysis. The formation of the skyrmion would be difficult to observe after the heat treatment of the samples but the displacements of larger domains are still measureable since the size is larger than the width of the noise.

Chapter 6

Chip fabrication

6.1 Introduction

As mentioned in §5.5.3, the magnetic track was attached to a PCB and then stuck on the VFM section. §2.2.2 mentioned the lithography technique MLA to fabricate the chip pattern. Each layer has its function, and its performance will limit the allowed current applied on the chip. In this chapter, the chip design and layer functions and the characterisation of the patterns are described. This chapter will also present the method and results of optimising the layers.

6.2 Chip Pattern Design

The experiment aims to measure the motion of a magnetic texture driven by a thermal gradient, so two thermometers and a magnetic track are the basic pieces needed on the chip. The pattern design for the 2 cm × 2 cm Si wafer is shown in Fig. 6.1 (a). The red part is the first layer, and the groups of crosses are the alignment crosses for the next layer. The alignment crosses separate four regions; three of them will be 7 mm × 7 mm chips, which will be attached to the PCB; the remaining region contains a large red square is the sheet sample, which will be the sheet sample for SQUID measurement. The size of the chip will allow the AFM cantilever holder clamp to move in both the x and y directions without crashing and destroying the wire bonding.

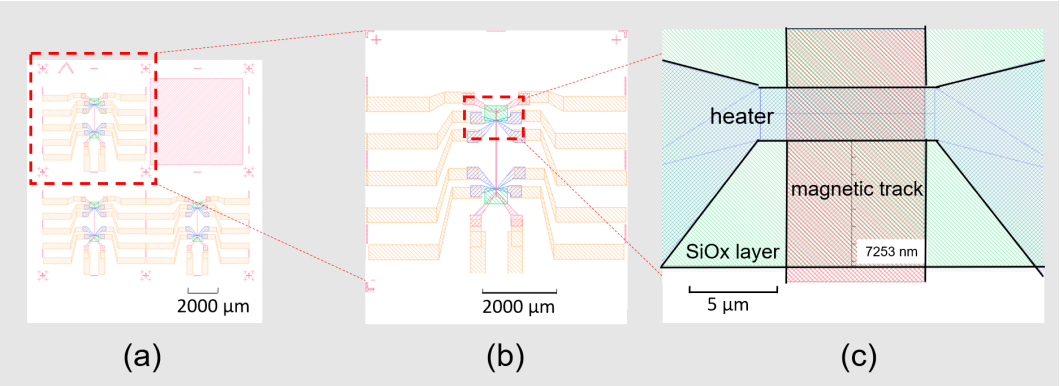

Figure 6.1: The design for (a) the 2 cm × 2 cm wafer and (b) remaining design on the chip after sawing. (c) The distance measurement between the SiO_x layer edge and the heater edge.

The wafer after sawing looks like Fig. 6.1 (b). The red pattern in the middle is the

magnetic track. The blue layer is the pattern of the Pt heater. We expect the Pt heater to have a large resistance to generate a larger range of the thermal gradient on the magnetic track. So, the Pt pattern is located on the magnetic track (red wire) and has a tiny width (3 μm). The four contact pads will allow the dc and ac current connection simultaneously to measure the heater's resistance while heating up. This allows us to use it as a thermometer as well as a heater.

The magnonic current is the only effect we considered in our theory of thermal-gradient-driven magnetic texture. Because we have a Pt cap at the top of the tracks and the CoB is not an insulating alloy, an insulator layer is necessary between the magnetic track and the Pt heater to avoid electrical current leaking into the magnetic track. The insulator layer (with around 100 nm thickness) is marked with green colour, which is made by RF sputtering SiO_x. The generated heat from the Pt heater will be partly absorbed by the SiO_x. The range of the thermal gradient is short along the $Co_{68}B_{32}$. Also, considering the roughness of the SiO_x layer and the MFM parallel measurement lift height upon the SiO_x layer, we want the MFM measurements to be done directly on the magnetic track but as close to the heater as possible. To achieve these requirements, the designed distance between the SiO_x edge and the heater edge is small (7253 nm on the software measurement). In the actual structure, the distance is micron precision and around 7 μm. The final layer is the Ti (5 nm) / Au (40 nm) layer to extend the connection of the Pt heaters and magnetic tracks to the chip's edge for the wire bonding preparation.

As shown in Fig. 6.2, to stick the chip on the PCB, the PCB has a 7.5 mm × 7.5 mm square depression area for the chip loading. We stuck the chip with both double-sided tape and permanent glue. The MFM measurements on the chip stuck by the permanent glue had less noise. It is high risk when the chip surface is lower than the contact pad because the wire might touch the underlying substrate or another adjacent wire. Before the sputtering process, the single-side polished Si wafer is $530 \pm 30 \mu m$. To achieve reliable wire bonding, the depth of the depression area is 400.0 μm.

6.3 The Optimisation of SiO_x Layer Performance

The insulation layer aims to avoid the leakage of the electrical current from the heater into the magnetic track. The STT from electronic and magnonic currents have the

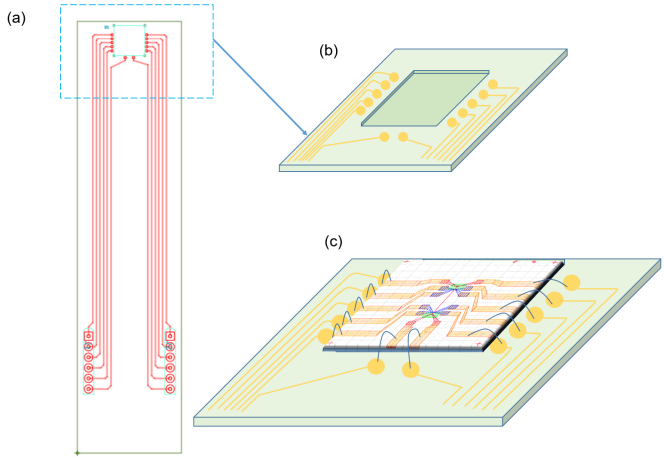

Figure 6.2: (a) The design of PCB and (b) the square depression area and wire bonding area without chip. (c) Wire bonding area after loading the chip and wire bonding.

opposite sign that will make the force model more complicated. The substrates used in this project are thermally oxidised silicon (100) wafers, the 100 nm thermal oxide is an electrical insulator. As the side view of the chip shown in Fig. 6.3 (a), the chip can also be regarded as a (b) parallel circuit with the Pt heater which thickness is around 250 nm and SiO_x layer. Most of the current is expected to flow through the Pt heater, but Pt heater and magnetic multilayer if SiOx is leaky. To test the performance of the SiO_x layer, we apply a voltage on SiO_x layer by using the contact pads of the Pt heater and magnetic track and measure the current. The compliance current was set to be 1 μA.

The SiO_x layer showed different properties even when they were prepared from the same sputtering chamber. During the lithography, the different developing rate between top and bottom photoresists can create an undercut for the developed photoresist pattern, which was described in §2.2.2, the microscope pictures of large and small undercuts will be shown in Fig. 6.4. For Fig. 6.3 (c) sample 1 with a small magnetic track undercut, when the voltage was applied over 1 V, the SiO_x layer resistance decreased significantly, and we suspected an electrical breakdown happened. Also, the data shows that the SiO_x layer is conductive but has a large resistance over 1MΩ . For Fig. 6.3 (d) sample 2, the contact between the Pt and SiO_x layer presented a similar V-I slope to metal-semiconductor junction. The positive voltage has a steeper V-I slope than the negative voltage data. By using the V-I slope of sample 1 with a small mag-

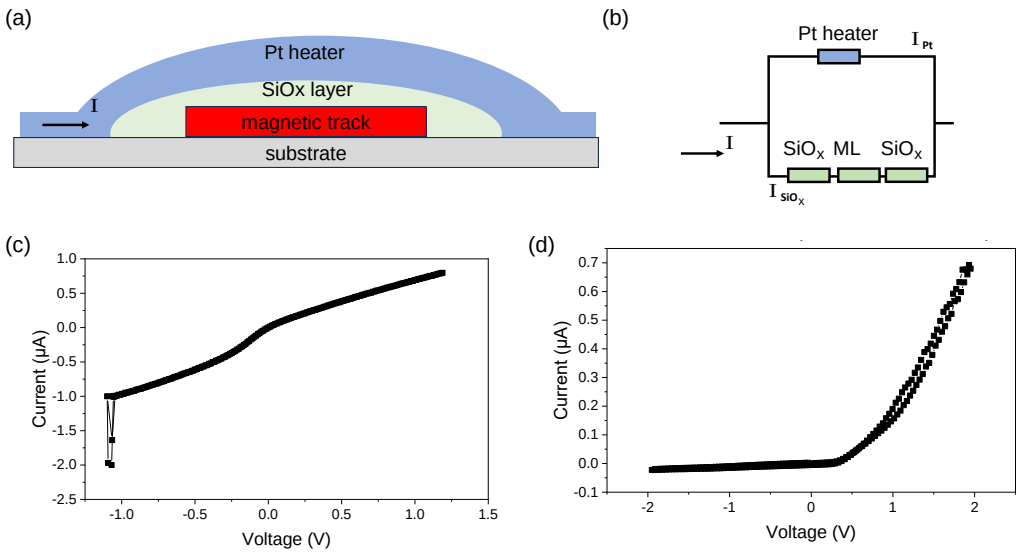

Figure 6.3: (a) The side view of the chip and (b) its equivalent circuit. (c) and (d) is the transport measurement data of the sample growth in the same RF sputtering chamber with small undercut during lithography.

netic track undercut, the resistance of the SiO_x can be estimated as $1{\times}10^6$ Ω. The Pt resistance on the chip is around 30 Ω; the measurement data will be shown in §6.4. Following the Ohm's law for parallel circuits, the ratio between the I_{Pt} and I_{SiO_x} will be $\frac{1}{3} \times 10^5$ Ω, 99.997% total current will go through the Pt heater. But to avoid the SiO_x layer broken with 1 V application (current on the Pt heater that SiO_x can tolerant is around 33 mA), we need to optimise the SiO_x layer.

The first step is cleaning the sputtering chamber; the dust or any black sediments drop from the linking part of the sputtering gun cap will increase the holes in the SiO_x layer, which will create a shortcut for the electrons to break the SiO_x.

Secondly, as mentioned in §2.2.2, the undercut's proper size will reduce the sample's crowning or fencing at its edges. An undercut will allow the thickness of SiO_x covered on the magnetic track to be more uniform, which is highly probable to improve the performance of the SiO_x. Different Defoc (the parameter of the objective lens defocusing level without unit) levels, laser exposure energy and developer solutions will also affect the undercut shape mentioned in the §2.2.2. The first recipe used for exposure and developing is: expose in MLA with Dose: 130 mJ/cm^2, Defoc: -4 and Developer

solution: 4:1 H2O: F351 for 45 s; the second recipe is: expose in MLA with Dose: 85 mJ/cm^2, Defoc: -4 and Developer solution: 3:1 H2O: F351 for 45 s. The undercut in Figure 6.4 (b) is significantly bigger than the one as shown in Figure 6.4 (c).

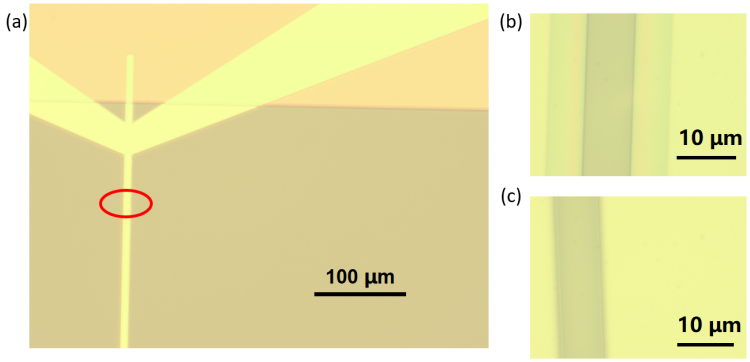

Figure 6.4: (a) The photo of the pattern under the microscope, the area circled by the red circle is expanded. (b) is the undercut created with the second recipe, and (c) is the first recipe. The yellow colour region in (a) is the magnetic track when the dark region is the SiO_x layer. In (b) and (c), the dark region is the region perpared for the magnetic layer sputtering.

In Figure. 6.5 (a) and (b), we can see the data of transport data measurement of the samples with larger undercut during the lithography. The SiO_x above a large undercut can withstand around 3 V, while the SiO_x above a small undercut will break or hit the compliance current 1 µA around 1-2 V. The resistance of the SiO_x can be estimated as 3×10^6 Ω, which is 3 times the resistance of the SiO_x layer above a small undercut. Also, the samples do not show semiconductor-like properties with a large undercut underneath.

After using the vacuum cleaner to clean the target and wiping the target cover with IPA, we deposited 1 SiO_x film with pure Ar gas and 1 SiO_x film with a mixture of oxygen and Ar gas for 1 hour. The chamber pressure needs to be maintained around 25 mTorr; the gas flow rate will be around 7.5 sccm after a few tests. The mixture of 97% Ar gas and 3% O_2 gas by sccm flow rate was used. With fixed chamber pressure, adding oxygen gas flow means reducing the Ar flow rate, so the Ar ion in the chamber will be reduced, and the SiO_x deposition rate will decrease. Also, the poisoning of target is another problem we need to concern with the increasing percentage of the reactive gas. Over 4.5% of the O_2 in Ar gas flow will lead to the poison mode [174]. The

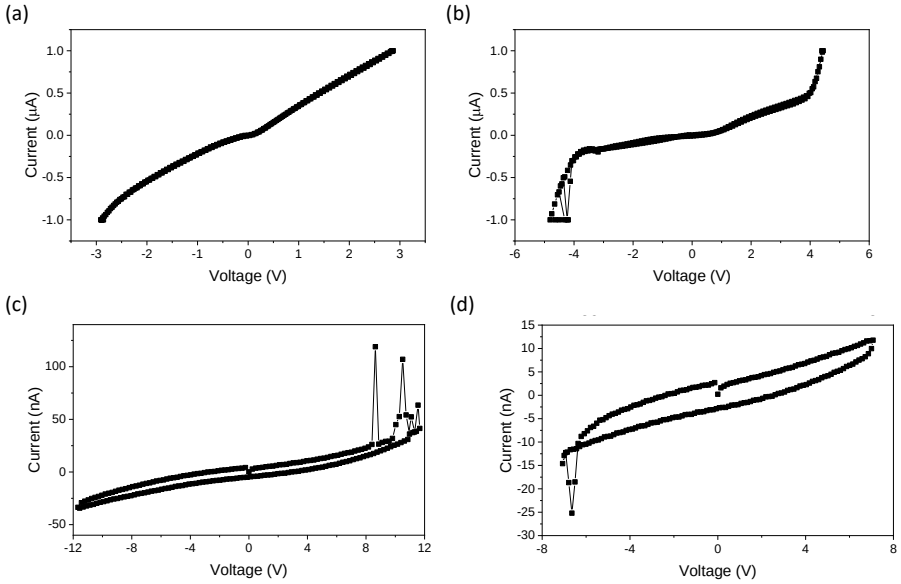

Figure 6.5: (a)-(b) The transport measurement of large undercut photoresist pattern of two different samples fabricated in the same chamber. The transport measurement of SiO_x sputtered in (c) pure Ar and (d) Ar-O_2 atmosphere (95% Ar gas and 5% O2), respectively. The data scales of all the graphs are different.

SiO_x thickness with and without oxygen during the deposition is 36 nm and 66 nm for 1 hour. The breakdown voltage of SiO_x deposited in an oxygen atmosphere shown in Fig. 6.4 (d) is 6.79 V while (c) the pure Ar atmosphere deposition sample can withstand at 9.77 V. The SiO_x breakdown voltage improves by 0.14 V/nm, and the optimisation methods are both working well. However, the growth rate of SiO_x in PVD is non-linear; 2 hours of deposition with an oxygen atmosphere can not guarantee producing a 60 nm SiO_x layer. To cover the magnetic track and its fencing, the thickness of SiO_x must be 2 times thicker than the magnetic track (at least 30 nm). So, we choose to use pure Ar gas to deposit SiO_x.

In summary, comparing to the SiO_x without optimisation, the SiO_x layer would provide a better performance when being sputtered on a sample with large undercut lithography photoresist mask inside a clean chamber with pure Ar gas flow.

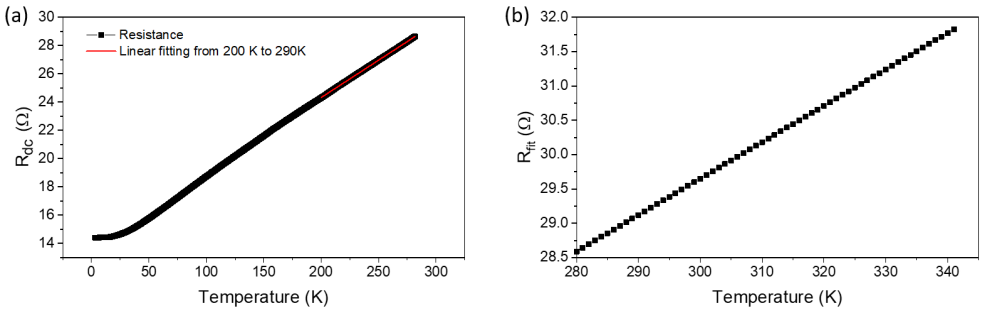

Figure 6.6: (a) Resistance of Pt heater on a flat surface with a sense current of 10 μA in a cryostat from 298K to 2K and (b) its extrapolation of linear fitting function $y = 0.053x + 13.751$ in the over 290 K region, where y is the Pt resistance and x is the temperature.

6.4 Pt Heater Resistance and Heat Gradient

Two Pt heaters/thermometers cross the magnetic track, as shown in Figure 6.1, which can be used to create a heat gradient along the magnetic track or detect the temperature at that position. To achieve those functions, the temperature-dependent resistance of the Pt heater need to be tested and calibrated with the ac resistance when a certain dc current applies to the heater. Because the resistance of Pt has a linear relationship with temperature, we can test the dc resistance of Pt heater R_{dc} by 10 μA dc current in a cryostat from 298K to 2K since this current is low enough to avoid measurable Joule heating. Also, the extrapolation of the linear fit to get the trend of R_{fit} resistance over room temperature is shown in Fig. 6.6. The reason why we did not measure the sample above room temperature is because of the equipment constraint; we did not have a hot plate that could provide the expected temperature and support the measurement at the same time.

Ideally, the thickness of the Pt will be uniform when the Pt heater is directly fabricated on the clean and flat substrate. But when the Pt is sputtered on a step structure, the thickness of Pt heater around the step edge will be non-uniform and might have mechanical deformation. The changes of the thickness will lead to a different resistance since $R = \rho\frac{L}{A}$, where ρ is the resistivity of the metal and A is the cross-sectional area of the conductor . Also, the deformation of the Pt layer might change the atoms spacing and affect the scattering of electrons. So, the resistance will be different because the

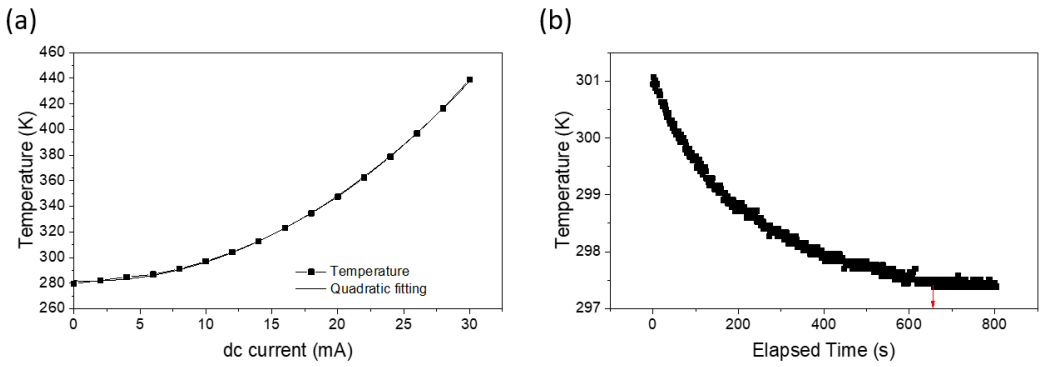

Figure 6.7: (a) The relation between Pt heater temperature and applied dc current. (b) The cooling time of a switch-off Pt heater stabilises after 600 s.

Pt heater will lay on the SiO_x layer and magnetic track. An additional calibration measurement for the temperature-dependent Pt heater resistance of this sample was measured. The ac resistance of heater R_{ac} on the actual chip was measured by 50 μA ac current. Using the lock-in amplifier, we can measure the ac resistance of the Pt heater with a dc current offset to heat the Pt heater. The Pt heater resistance in the cryostat was measured. The resistance of Pt still has linear relationship to temperature higher than room temperature. The measured ac resistance shows the temperature of the Pt heater by using the relationship between Pt resistance and the temperature. The generated temperature is associated with the dc current and the relationship between the temperature of the heater and the applied dc current is shown in Fig. 6.7 (a). The temperature of the heater is around 380 K when the applied current is 25 mA. So, 100 K temperature rise needs current is around 25 mA. The resistance of heater at 380 K is less than 40 Ω as shown in Fig. 6.6. Once the SiO_x layer breakdown voltage is larger than 1 V, it can withstand for the experiment-applied dc current.

It would need few minutes to cool down the heater into the room temperature. For example, a 286 K heater needs 600 s to cool down to 278 K after switching off the applied 10 mA dc current as shown In Fig. 6.7 (b). The time-varying heater temperature without dc current offset shows the time length for heater cooling down to a stable temperature.

6.5 Checking the Fabrication Process

Over 40 minutes of evaporation of Ti/ Au contact pads over 80 °C will decrease the interaction between the magnetic sample and the MFM tip after the sample fabrication. To find out which step of the fabrication caused the signal to disappear, MFM measurements with a small magnetic field after every layer of fabrications were made. The RF PVD and thermal evaporator are the steps that easily cause the magnetic sample annealing.

To ensure the RF sputtering lighting up correctly, we need to use another gun to light up the SiO_x gun with 40 sccm Ar flow rate. After lighting the plasma correctly, the Ar gas flow rate will be adjusted back to 24 sccm. The chamber temperature did not increase over 80 °C. For the thermal evaporator, the current to heat the target boat needs to increase slowly with the 0.2 A step and it is necessary to stop increasing the current when the sensor starts to display a positive growth rate. To maintain the temperature in the chamber not higher than 60 °C, the current for Ti material evaporation is less than 23 A and less than 40 A for Au.

6.6 Summary of the Correct Steps to Prepare Sample

The samples need to be taken care of in every step to reach the requirement of the good performance of the chips. A large undercut of the lithography pattern is needed in the early stage by exposing the sample in MLA with Dose: 85 mJ/cm^2, Defoc: -4 and Developer solution: 3:1 H2O: F351 for 45 s. Then, the SiO_x rf sputtering needs to provide at least 100 nm thick SiO_x by pure Ar gas with an effective lighting-up gun. Finally, the depositions of all the layers upon the magnetic track need strict temperature control, such as the controlled current for Ti and Au evaporation, 23 A and 40 A, respectively.

Chapter 7

Observation of Domain Wall Motion Driven by Varying Heater Currents

7.1 Introduction

Spin transfer torque (STT), resulting from spin-polarized electric currents, and spin-orbit torque (SOT), arising from spin-orbit interactions in materials, are two primary mechanisms that drive magnetic textures and have been extensively studied by numerous researchers.[15, 19, 35, 79, 175–177] In the actual application of the electric current to drive magnetic texture, the varying Joule heating on the devices is unavoidable. The complex domain motion under different driving forces can be analyzed by the sum of individual effective fields from different effects in the LLG equation, such as Eq. 1.1. So, the domain motion only depends on the thermal gradient, which is worth studying.

In this chapter, we will show the domain displacements of domains under different temperature gradients. When the temperature difference between the heater and the room temperature is larger than 65 °C, the domains start moving forward to the heater (hot region). Due to Oersted's law and the dc current being used to generate the thermal gradient, the effect of the magnetic field created by Oersted's law also needs to be considered. We subtracted out the effects of the Oersted field and a temperature gradient driven motion was still measured. The result also shows that the domain will have a more significant displacement when it is closer to the heater.

7.2 DC Current Setup for the Thermal Gradient

In the equipment setup, the dc or ac current was applied on the PCB when the PCB was under the AFM head. The MFM measurements were done before and after the dc currents were applied in this project. The current source model 6221 from Keithley Instruments, Lock-in amplifier SR83 from Stanford Research Systems and breakout box are needed to realize the setup. The model 6221 can provide a dc current and ac current simultaneously, and the lock-in amplifier can measure the voltage response of a small ac current to get the ac resistance of the heater. The PCB will connect to the breakout box, as shown in Fig. 5.11 (a). The two six-pin Lemo plugs and their sockets realize the connection of 12 wires between the PCB and the breakout box. Then, the wires have parallel connections to each switch and BNC socket. Two non-isolated BNC connectors will connect with the triax connectors (one of the pins was grounded) to get the current supply into the box. The current supply is from the Keithley 6221.

To use the lock-in amplifier to measure the ac resistance, the Model 6221 will provide ac current, but the current will also go through the lock-in amplifier by the trigger link cable connection. The dc current form is set as a DC square wave with a 2-minute pulse, and the current amplitude is from 20 mA to 50 mA with a 10 mA step.

The temperature of the Pt heater can be inferred from the resistance measurement using the calibration in §6.4. However, because we have the heater on the magnetic track separated by SiO_x layer in the middle, the actual temperature on the track cannot be measured. Since the Pt and SiO_x layers are very thin and flat with a large contact area, the actual temperature on the track in the region directly under the heater can be assumed to be roughly the same but smaller than the temperature of the heater. There will then be a temperature gradient down the track as the distance from the heater increases.

7.3 Different Current Pulse Direction with Opposite Track Magnetization Direction

The first step to start the experiment is finding the domains from the MFM measurement and figuring out the positions and sizes of the defects. In Fig. 7.1, the MFM measurement data gives the reference point that around 30 Oe, the worm-like domains start to appear. In this chapter, all the defects will be circled by the yellow dashed line. The incomplete lift-off might happen because it is hard to determine whether the transparent SiO_x got effectively and fully removed. So some residues of the SiO_x or Pt can remain as defects. These structural defects might affect the way that nearby domains propagate or nucleate. The structural defects were identified by the dark region in the MFM measurement with the external magnetic field, which is much larger than the sample saturation field. So, any new regions of dark contrast outside the yellow circles are magnetic textures. The subplot on the right-hand side of Fig. 7.1 was made when the magnetic track was fully saturated. The dark defects on the bottom left are the defects of the edge of the SiO_x layer. The edge of the SiO_x layer is the edge of the green area in the KLayout designed in the top-left subplot. The edge of the SiO_x layer is also the reference line to measure the distance between domains and the heater. The background noise is the small but high-frequency stripes in the saturated state MFM figure. The magnetic domains are bigger than the size of the background noise stripes,

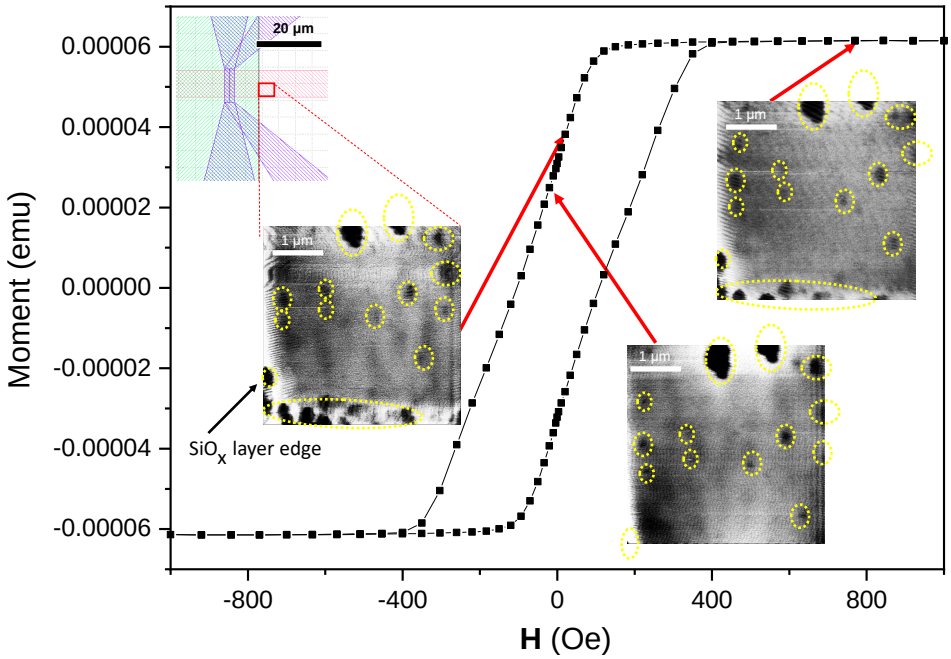

Figure 7.1: The hysteresis loop of magnetic track and MFM measurements with different external fields.

as shown in the subplots on the left-hand side.

The 20 mA current with a 2-minute width pulse is first applied to the heater. The heater can generate 65 °C temperature difference with room temperature. As shown in Fig. 7.2, the yellow dashed circles point out the defects and make sure the figures are aligned. By exporting the line profile at the middle of the figure with a 50-pixel width average, we can see that the dips in the line profile represent the dark domains. Using the Gaussian dip fitting $y = A \exp\left(-\frac{(x-\mu)^2}{2\sigma^2}\right)$, where μ is the position of the peak's center, σ is the width of the peak. The data shows that the locations of Guass dips did not change after applying the 20 mA in Table. 7.1. Though we see a slight difference between (b) and (c), the locations of the domain line profile Gaussian dips are within the fitting error, which suggests that the domains did not move. So, the critical current that can move domains is higher than 20 mA with our device. Meanwhile, we can see the sizes of dips, which represent the sizes of the domains, were decreasing for responding to the dc current application. The Oersted field can not be ignored and will be discussed later. We defined the direction of the 20 mA in this measurement as positive current.

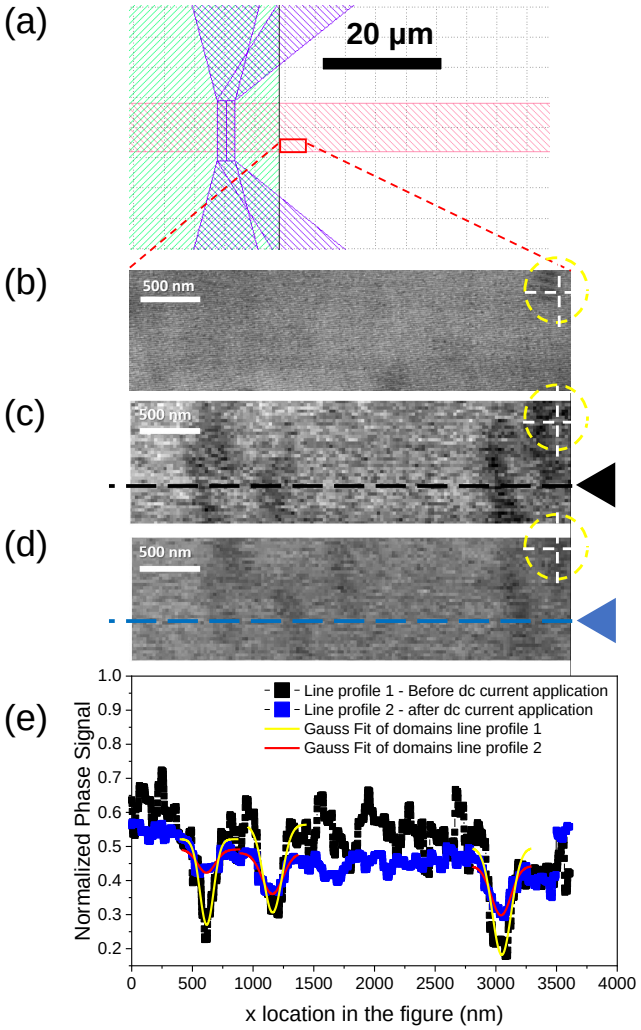

Figure 7.2: (a) The MFM measurement region of interest. (b) The MFM image when the track is fully saturated with 600 Oe. (c) and (d) are the MFM images in 30 Oe before and after heating. The line profiles of the MFM images (c) and (d) are shown in (e). The dashed black and blue lines show where the line profiles were taken from (c) and (d). The cross hairs are at the middle of the circle, which helps us align the position of the defects.

No.	I_{dc} application	Dip width (nm)	Dip location (nm)
1	before	110 ± 40	620 ± 20
1	after	150 ± 10	620 ± 20
2	before	150 ± 30	1160 ± 20
2	after	170 ± 20	1160 ± 20
3	before	160 ± 40	3050 ± 80
3	after	160 ± 40	3040 ± 60

Table 7.1: The Gaussian fitting dip details of line profile of domains with 20 mA dc current application.

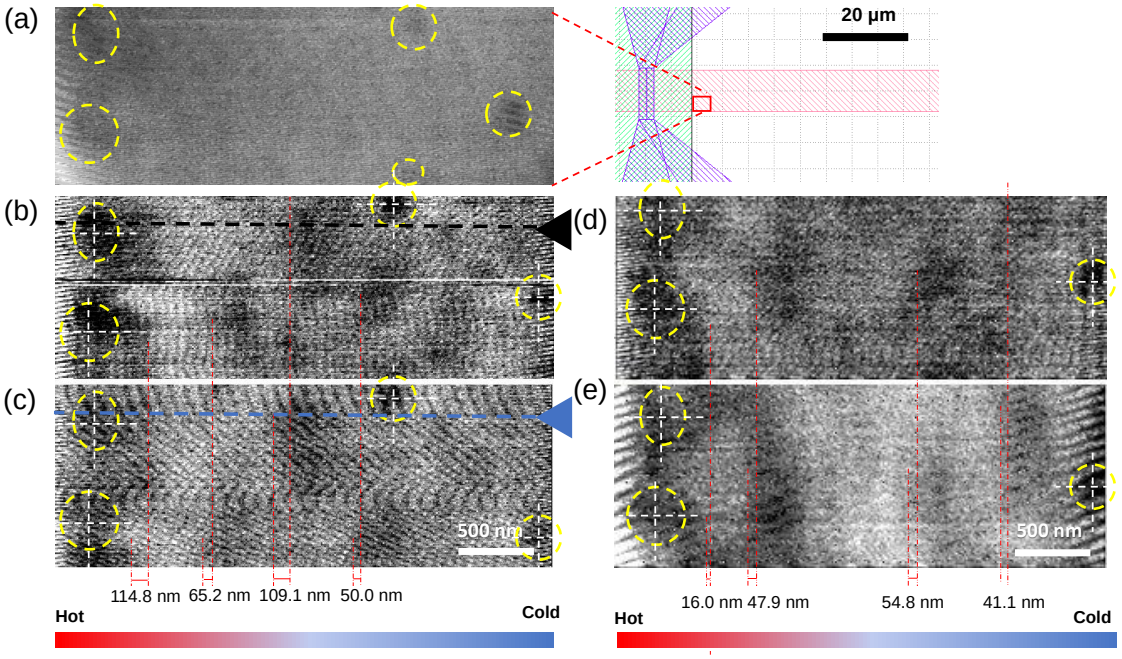

Figure 7.3: (a) The MFM image when the track is fully saturated with 700 Oe and the dark regions in the dash yellow circles are the defects on the track surface. The right-hand side is the MFM measurement region on the sample. (b)-(c) are the MFM images in 30 Oe before and after +30 mA current applied to the heater, respectively. The dashed black and blue lines show where the profiles in Fig. 7.4 were taken from (b) and (c). (d)-(e) MFM image in 30 Oe before and after -30 mA current applied to the heater, respectively.

Fig. 7.3 (a) is the MFM image when the magnetic track is fully saturated. The defects circled by the dashed yellow circles are used to align the track position. With the alignment of the defects, the domain displacement measurement can be more reliable and accurate.

Fig. 7.3 (b) and (c) show the MFM images before and after the +30 mA current is applied, respectively. The colour bar under the figures shows the position of the hotter (red) region and colder (blue) region. The red dashed lines were manually drawn to show the movement of the edge of the domains. However, the displacements were still calculated by the positions of the Gaussian dips on the line profiles as Fig. 7.2. We renucleated the domains by saturating the sample and then decreasing the field to the previous value. The domains re-appear in a similar position each time. After

renucleating the domains, the MFM measurements were done before and after the -30 mA current application. The MFM images when the -30 mA current was applied (d) before and (e) after are shown in Fig. 7.3. Both positive and negative currents can generate a thermal gradient that drives domains towards the heater.

We used one of the domains driven by the positive 30 mA dc current to do Gaussian fitting. Its line profile is shown in Fig. 7.4. Comparing the locations of the defects, we aligned the figures, and the domain displacement can be calculated by the Gaussian dip location as shown in Table. 7.2. This domain got around 110 nm displacement. Also, the domain line profile Gaussian dips change in the Table. 7.2 shows that domain size decreased after the positive dc current application.

Because of the dc current I_{dc} we applied to the heater, the influence of the Oersted field is another critical factor that must be considered. To prove the motion of domains purely depends on the thermal gradient, the effects of Oersted fields from dc current need to be studied and removed by averaging the displacement from both positive and negative current.

Firstly, the Oersted field will affect the size of the domains. Since the direction of the magnetic field was the same as the domain magnetization direction, the field made the spin of the domain wall align with the direction of the field, which caused the expansion of the domains.

Secondly, if the domains are regarded as rigid objects, the interaction between the field and the domain will lead to the displacement difference between different directions of the Oersted field.

The data in Table. 7.1 and 7.2 showed that the domain size changes differently with the application of the different direction currents and different domain displacement between different direction currents. So, we speculate that the different heating current direction generates different forces to the magnetic patterns as shown in Fig. 7.5. F_{heat} is the force generated by the heat gradient. $F_{\text{repulsion}}$ and $F_{\text{attraction}}$ are defined as the repulsion force and attraction force from the interaction between the Oersted field and domains, respectively.

The Oersted field generated by 30 mA can be decribed by $H = \frac{I}{2\pi r}$, where r is the distance from the single wire Pt heater. With a distance of 5000 nm (the closest domain location to the heater), the approximately Oersted field strength is 0.96 Oe.

Owing to the phenomenon of electromagnetic induction, the dc current induces a

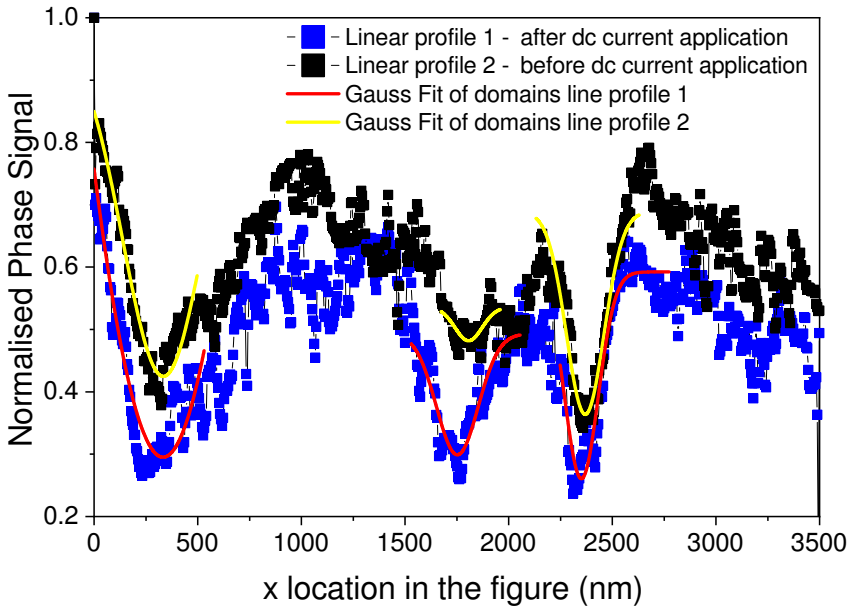

Figure 7.4: The line profiles of one of the domains with 30 mA positive dc current application in Fig. 7.3 (b) and (c). The domain had around 110 nm displacement.

No.	I_{dc} application	Dip width (nm)	Dip location (nm)
defect 1	before	390 ± 30	335 ± 4
defect 1	after	400 ± 20	336 ± 4
domain	before	130 ± 10	1880 ± 10
domain	after	410 ± 20	1770 ± 30
defect 2	before	210 ± 20	2370 ± 4
defect 2	after	180 ± 10	2370 ± 3

Table 7.2: The Gaussian fitting dip details of line profile of one of the domains with 30 mA positive dc current application. The domain had around 110 nm displacement.

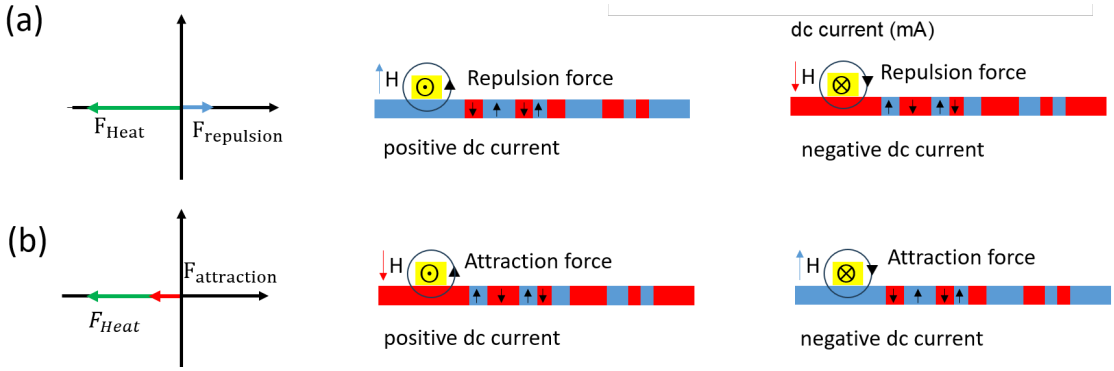

Figure 7.5: (a) The force model of repulsive force from the different currents created Oersted field with different magnetization of domain patterns. (b) The force model of the force of attraction from the different currents created an Oersted field with different magnetization of domain patterns.

small magnetic field with a tiny gradient along the magnetic track. As derived from Maxwell's equations, $\mathbf{F} = -\nabla U = \nabla(\mathbf{M} \cdot \mathbf{B})$, where U is the magnetic energy density, $\mathbf{M}$ is the magnetization vector of the material, $\mathbf{B}$ is the magnetic flux density, the domain which has magnetization direction aligned with the dc current induced magnetic field will have a attractive force towards the direction of stronger field (heater), as shown in Fig. 7.5 (b). Conversely, as shown in Fig. 7.5 (a),when the magnetization direction is anti-paralleled to the dc current induced field, they have a repulsive force away from the heater. $F_{\text{repulsion}}$ and $F_{\text{attraction}}$ are defined as the repulsion force and attraction force from the interaction between the Oersted field and domains, respectively. The direction of $F_{\text{repulsion}}$ is opposite to the direction of F_{heat}. But $F_{\text{repulsion}}$ has a smaller amplitude than F_{heat}, this keeps the domains toward to the heater. Also, the Oersted field will affect the size of the domains. To minimize the magenetic energy of the system, the magnetization of the domain prefers aligning to the stronger total external field.

In our experimental data shown in Fig. 7.6, though the displacement of the domain driven by +30 mA is smaller than the domain displacement driven by -30 mA with +z sample magnetisation direction, the domains were all forwarded to the hotter region. This means the amplitude of $F_{\text{repulsion}}$ or $F_{\text{attraction}}$ is smaller than the F_{heat} as shown in Fig. 7.5(a).

The domains driven by both positive and negative 30 mA current with different

magnetization directions were measured to prove the force model of the domain motion under the effect of the Oersted field. In Fig. 7.6, the solid black square symbol and solid red circle symbol are the domain displacement with sample magnetization direction on the +z-axis driven by negative and positive heater current, respectively. The negative current can drive the domain closer to the heater than the positive current, which means the Oersted field created by the positive heater current has the different direction to the domains downstream of the thermal gradient. Also, the larger distance between the domain and the SiO_x edge, the smaller difference between the domain displacements driven by different direction currents, refers to the lower efficiency of the Oersted field. After renucleation of the domains with opposite external magnetic fields, the MFM images were measured when the magnetization of the magnetic track orientation was in the -z-direction. As shown in Fig. 7.6, the domain displacement is driven by positive and negative heater current with a hollow red circle symbol and hollow black square symbol. The experimental results, as anticipated, show that the positive current application leads to a larger domain displacement compared to the negative current when the magnetization direction of the sample is flipped over. The measurements were done in 4 repeats, and the uncertainties were from the standard deviation/ $\sqrt{4}$ of 4 repeats measurements.

Using the same symbols to show the same experiment setup, we showed the sizes of domains that responded to the different dc current applications with different sample magnetization directions in Fig. 7.7. The domains shrank when the Oersted field was parallel to the external field. The difference of the sizes of domains before and after the dc current application is Δd_d, the region of negative values is marked with pink colour. When the domains are closer to the heater, a larger Oersted field is applied to the domains.

7.4 Different Current Pulse Amplitude

In recent publications, researchers have discussed the theory for thermal-gradient-driven domain-wall motion. The motion of the domains is due to both the entropy originating from the magnon-bound states and a magnonic spin current from the Seebeck effect. [92, 178] In this project, we are concerned about the STT between the magnonic spin current and the domains.

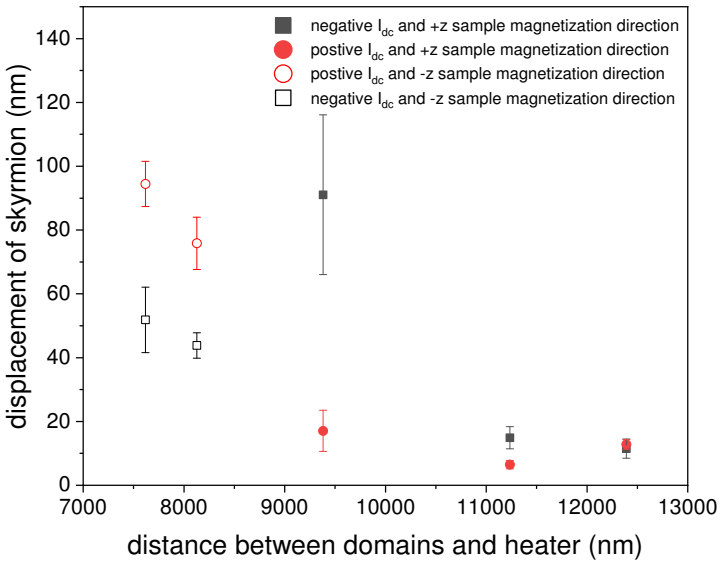

Figure 7.6: The domains were driven by both positive and negative 30 mA current with different magnetization directions.

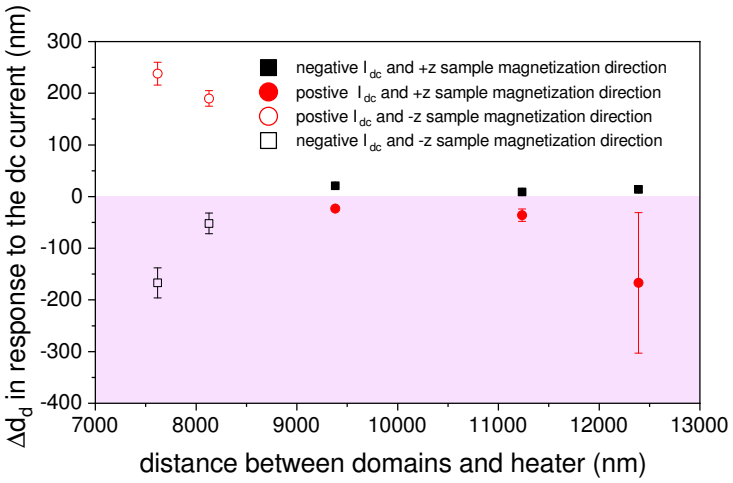

Figure 7.7: The sizes of domains responded to the positive and negative 30 mA current with different magnetization directions.

The LLG equation can always describe the dynamic magnetic domains by modelling the effects of a field. By substituting the Walker ansatz into the Landau-Lifshitz-Gilbert equation Eq.1.1, we can write:

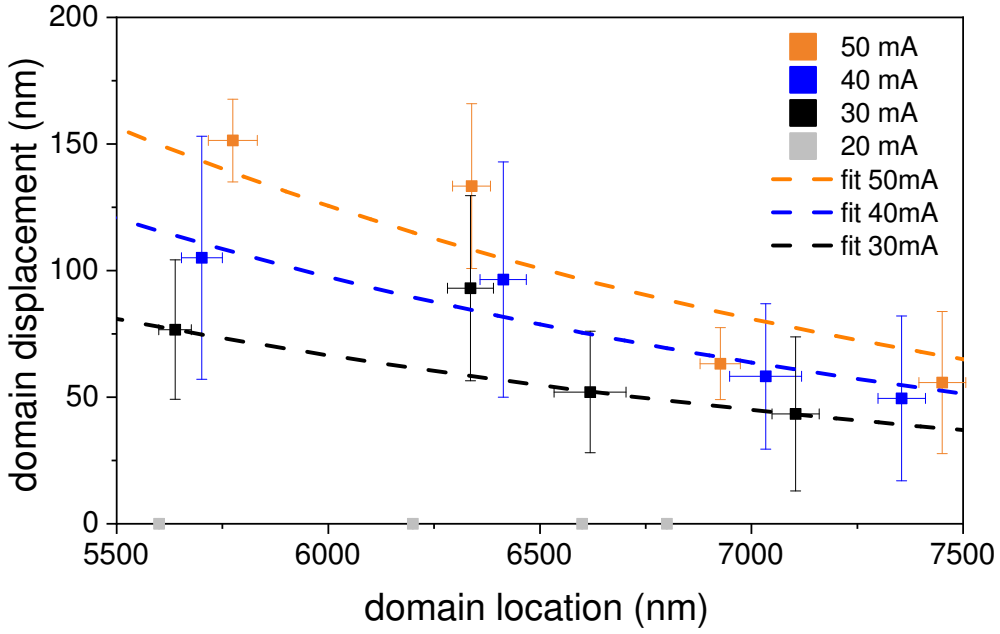

Figure 7.8: The average of the domain displacement driven by varying positive and negative currents.

$$M_s = -\gamma \mathbf{M} \times \mathbf{H}_{\text{eff}} + \alpha \frac{\mathbf{M}}{M_s} \times \frac{d\mathbf{M}}{dt} + \gamma \hbar J_s \left(\frac{\partial \mathbf{M}}{\partial x} - \beta \frac{\mathbf{M}}{M_s} \times \frac{\partial \mathbf{M}}{\partial x} \right), \tag{7.1}$$

where the J_s is the spin current current from the spin Seebeck effect. The current J_s is proportional to the heat gradient. The larger the heat gradient, the stronger the magnon current flow from the hot region to the cold region.

Fig. 7.3 (b) and (c) show a few domains before and after a 30 mA current excitation on the heater with a time width of 2 minutes, respectively. The relationship between the domain displacement and the temperature generated by the heater is also studied and shown in Fig. 7.8. The domain displacement with a positive and negative current pulse is averaged to mitigate the impact of the Oersted field. The x-axis shows the distance from the domain to the heater, and the error is from the standard deviation of the positions of 4 different domains after every pulse (3 repeat pulses for each condition). The y-axis shows the domain displacement, and the y error is from the standard deviation of the displacement of domains after every pulse.

In Fig. 7.8, the domains start to have significant displacement when the current is larger than 30 mA. The tiny displacement of domains with 20 mA dc current application is due to the line profile fitting error. With increasing current amplitude applied to the Pt heater, the higher temperature gradients generate J_{m} with higher density. The higher density of magnons will have a stronger total STT between the magnons and domains, which leads to larger domain displacement. Because the CoB material is a metal with good thermal conductivity and allowing the heat gets transport to the substrate rapidly. So the magnetic track has rapid heat dissipation across along the track, and the heat gradient in the area away from the heater is smaller. The domains will have smaller displacement when they are away from the heater since lower heat gradient. The value of the first data point of the 30 mA is not as large as expected. By checking the MFM images (for example, Fig. 7.3), the first domain is found already close to the defect. Because the area near defects has nonuniform growth of the material layers, this will cause the varying and nonuniform anisotropy of the sample. The pinning energy for domains will be increased by the defects, which will slow down the domain motion. [179]

We can have the temperature distribution along the track by fitting the domain average displacement with domain displacement $\mathrm{Y_d}$ exponential decay model.

$$T(x) = \Delta T e^{(-x/l_T)}, \tag{7.2}$$

$$\nabla T = \frac{-\Delta T}{l_T} e^{(-x/l_T)}, \tag{7.3}$$

$$Y_{\mathrm{d}} = k_{\mathrm{track}} \left(-\frac{\Delta T}{l_{\mathrm{T}}} e^{-\frac{x}{l_{\mathrm{T}}}} \right), \tag{7.4}$$

where k_{track} is a parameter that shows the effect of the temperature on domain displacement with unit $\mathrm{m^2/K}$, ΔT is the temperature difference along the track, and l_{T} is the temperature decay length along the track due to both the thermal conductivity of the CoB track and the thermal conductance of the CoB/SiO_x interface. The ratio between thermal conductivity of CoB layer (unit : $\mathrm{W/(m \cdot K)}$ and thermal conductance (unit : W/K) of the CoB/SiOx interface is the characteristic length scale l_{T}.

By using the data in the Table. 7.3, we can get the average of the characterization temperature decreasing length is 2400 nm ± 200 nm. The temperature along the track can be estimated by $\mathrm{l_T}$ as shown in Fig. 7.9. The baseline T is the ambient temperature in the lab during the winter (290 K). Here, we use x to represent the distance between

I_{dc}	ΔT (K)	k_{track} (nm^2/K)	l_T (nm)
30 mA	162	−3900 ± 900	2600 ± 400
40 mA	280	−5200 ± 500	2400 ± 100
50 mA	445	−5000 ± 1000	2300 ± 100

Table 7.3: The parameter of exponential fitting for the average of the domain displacement driven by varying positive and negative currents.

a certain location on the track and the heater. With 50 mA dc current applied to the heater, the temperature at x = 5800 nm was lower than 330 K. The MFM observation of the domains means the temperature within the interested area was still lower than the Curie temperature. The temperature of the track generated by 20 mA at x = 5800 nm is lower than the temperature generated by 30 mA current at x = 7000 nm. The defect located around x = 5800 nm has high pining energy. In this case, the spin transfer torque from the spin current generated by the heater with 20 mA can not move the domain at x = 5800 nm.

The relationship between the Oersted field and varying current amplitude applied to the heater can also be studied by taking the difference of the domain displacement with positive and negative currents. In Fig. 7.10, the domains with higher amplitude current applied to the Pt heater have larger domain displacement differences than the smaller current-driven domains. The decreasing of the magnitude of the Oersted field outside of a current-carrying wire obeys the rule $B = \mu_o I/2\pi r$, where r is the distance to the current-carrying wire (heater). Both domain displacement differences of 50 mA and 40 mA are inversely proportional to the distance between domains and the heater but have different slopes. The unexpected last data point of the 30 mA might be because some of the renucleated domains are close to the defects with higher pinning energy, leading to a significant difference in the domain displacements between pulses.

7.5 Conclusion

To summarise, the displacement of reverse domains in a perpendicularly magnetised metallic multilayer driven by a temperature gradient were observed by MFM. The force from the Oerster field generated by the dc current is smaller than the force from the heat gradient denerated spin current. So, the domains always move up the

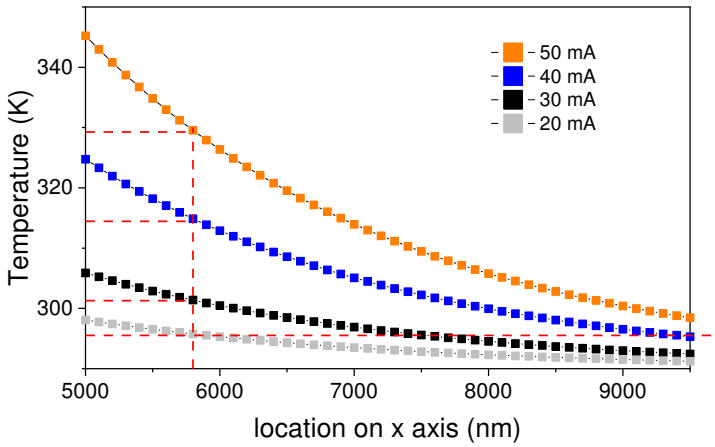

Figure 7.9: The temperature along the magnetic track is generated by varying dc currents. This determination is based on fitting the observed domain motion and employing the temperature calibration of the thermometer. The red dashed lines are used to point out the different temperatures at x= 5800 nm generated by different dc currents. The red dashed line also indicates that a larger distance from the heater is required to achieve the same temperature produced by a 20 mA current at x = 5800 nm when the temperature is generated by a 30 mA current.

temperature gradient towards the hotter region with the force from the Oersted field.

By cancelling the effect of Oersted fields generated by the calibrated thermometer/heater wire we are able to quantify the effect and find that the scale of motion we see is consistent with spin transfer torques generated by the electronic spin Seebeck effect. The larger heat gradient, the larger domain displacement. The domain displacement can be used to model the temperature distribution along the track. The temperature model shows that the heat generated by the 20 mA (lower than the critical current 30 mA) in the area close to the heater is smaller than the heat generated by the critical current in the area away from the heater and domain had a tiny displacement.

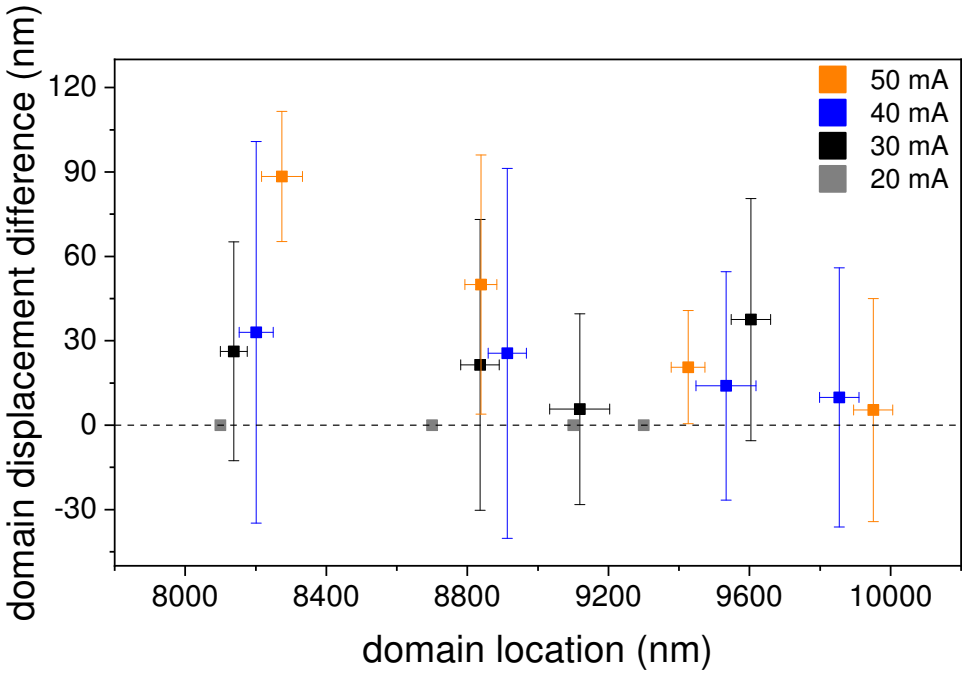

Figure 7.10: The difference of the displacement of the domain driven by varying positive and negative currents.

Chapter 8

Conclusions and Further Work

8.1 Conclusions

This thesis has focused on magnetic texture dynamics within the Ta/[Pt/$Co_{68}B_{32}$/Ir]$_n$/Pt heterostructure. The critical role of spin currents in driving magnetic texture dynamics motion has been highlighted, establishing a clear understanding of the forces at play in the manipulation of domains and quasiparticles - skyrmions.

The sample characterisation methods were reported in Chapter 2. The samples were successfully fabricated and proved to stabilise worm-like domains and skyrmions with an external magnetic field. The micromagnetic simulation software OOMMF was used in the simulation part to set up the environment. In Chapter 4, simulations based on the Ta/[Pt/$Co_{68}B_{32}$/Ir]/Pt sample were studied. The skyrmion transient retrograde motion on the x-axis driven by the spin waves was found in magnetic tracks wider than 50 nm with damping constant $\alpha = 0.02$. With a fixed magnetic track width of 100 nm, the varying damping constants were set up to the magnetic track. The skyrmions showed motion simply along with the spin wave propagation direction. The motion of the skyrmion on the y-axis is always towards the upper sample edge because of the skyrmion Hall effect.

In this project, the forces from the spin wave were assumed to arise from the time-varying transmitted and reflected spin wave rather than just the fixed scattered spin wave. The SW data collection for simulation celles in a line parallel to the x-axis is easier than the cells in a line which has an skyrmion hall angle to x-axis. The simulation results for transmitted and reflected spin waves can be obtained from the spin wave amplitude downstream and upstream of the skyrmion, which will be more precise than the model based on a fixed strength of the scattering. The Thiele equation was used to analyse the skyrmion motion with force from the transmitted, reflected spin wave and the repulsive force from the track edge. The spin transfer torque from the transmitted spin wave drove the skyrmion to the spin wave source, while the linear momentum transfer from the reflected spin wave pushed the skyrmion away from the spin wave source. The force on the y-axis also affected the skyrmion velocity on the x-axis due to the gyrovector. The predicted skyrmion motion fits with the observed skyrmion motion. This result revealed the relationship between the skyrmion motion and the balance of the forces from the spin wave and the track edge, explaining the skyrmion retrograde motion. The force model also predicts the different skyrmion motion tendencies at different skyrmion initial positions.

Advanced experimental imaging techniques - Magnetic Force Microscopy for magnetic patterns have been discussed in Chapter 5 and 6, which are crucial for observing and understanding domain behaviour at the nanoscale. The experiment of spin current-driven magnetic texture was mentioned in Chapter 7. We have explored the effect of the spin current generated by heat gradient. The spin Seebeck effect initiates a spin current from cooler to warmer regions on the magnetic track. The critical temperature between the room temperature and heater temperature to move the domains is 338 K. The spin transfer torque from the spin current will drive the domains toward the hotter region. The dc currents were applied on the heater, which means the effect of the Oersted field is unavoidable. The Oersted field orientation affected the sizes of domains and their displacement after the heat gradient application. Discounting the effect of the Oersted field by averaging the domain displacement driven by both positive and negative dc currents, we found the larger heat gradient applied on the track, the larger domain displacement showed. The domain displacements from different initial positions on the x-axis were proportional to the exponentially decreasing temperature along the track.

In conclusion, direct observation of the magnetic texture driven by spin current arising from temperature gradient obeying the theoretical prediction was discussed in this thesis. In the theory, the larger temperature gradient on the magnetic track, the larger magnetic texture displacement will occur. The encouraging outcomes of the force from Oersted field model analysis give us confidence in the spin current application to the spintronic devices. At the same time, there are also many further researches worth studying in the future, which will be mentioned in the next section.

8.2 Further Work

8.2.1 Using FMR to Analysis the Exchange Stiffness

In this project, the alloy of Cobalt and Boron is used, which is hard to define the atom spacing for normal Bloch law. The unceratinty will arise from the Pt polarisation and the fitting of alloy Bloch law as mentioned in Chapter 3. The ferromagnetic resonance (FMR) is another way to obtain the spin wave stiffness, which does not require Bloch law fitting. The frequency of the resonance and the known anisotropy of the material can give the spin wave stiffness. Refering to $A = \frac{M_s(0K)C}{2g\mu_B} =$, the exchange stiffness can

be obtained more straight forward.

8.2.2 Skyrmion Motion Driven by the Spin Wave

In our prediction, different initial positions of the skyrmion will have different motions because of the gyrovector and the repulsive force from track edges on y-axis. The experiment of the skyrmion on a magnetic track wider than 100 nm is worth investigating and comparing with our simulation results. To inject spin waves into a magnetic layer, a coplanar waveguide can be built to excite alternating magnetic field on the track by injecting microwave frequency current [180, 181]. The oscillating magnetic field interacts with the magnetic spins in the magnetic layer just like the simulation setup and create a spin wave.

8.2.3 Micromagnetic Simulation about the Heat Gradient on the Magnetic track

Since the experimental data about the domain displacement under the heat gradient is collected without the measurement of the actural heat gradient along the track, it is worth to do micromagnetic simulation to figure out the distribution of the temperature along the track. The model with a characteristic length scale relevant to the heat flow is still rough.

Micromagnetic Monte Carlo (MMC) method was dicussed in published research, and it shows the simulations that with the same external OOP field, the magnetic texture formation will change from maze domains to skyrmions with increasing temperature. The non-uniform temperature will let the high temperature area shows skyrmion while there are domains in cooler area. In future study, a high temperature gradient can be applied on the track with 0 field to observe the changed pattern of magnetic textures along the track and compare with the simulation result to gain reliable temperature gradient.

8.2.4 Skyrmion Hall Effect Driven by the Spin Current

During the MFM measurement, we found the stripes-like background noise can bury the tiny skyrmion, which does not allow us to observe the skyrmion when the external field is close to the saturation field, like Fig. 5.7. Luckily, one skyrmion-like magnetic

pattern was found during one of the measurements with an opposite J_{m} generated by 30 mA dc current applied on another heater on the right-hand side of the track. The skyrmion-like magnetic pattern is smaller than the dark domains on the left hand side and with a round shape. with a slightly higher magnetic field applied on the sample, the sample got fully saturated. So, it is nearly certain to be a skyrmion. In Fig. 8.1, yellow circles circle the defects, and the skyrmion-like magnetic pattern is in the red circle. By aligning the defects and measuring the distance between the skyrmion and the defect from the initial skyrmion position and final position, the skyrmion Hall effect angle is $\theta_{sky} = \arctan \frac{441.9-360.5}{34.9} \approx 67^{\circ}$ and the uncertainties is 1°. In Yu's team's published paper, the skyrmion hall angle will slightly increase and then saturate within the increment of the thermal gradient from 0.1 K/mm to 1K/mm.[182] Due to the mechanical noise from the measurement system and the space limitation under the AFM head, we cannot observe clear skyrmions driven by varying heater excitation currents or measure the actual temperature on each point of the track. Requiring further investigation of the skyrmion driven by the thermal gradient, the relationship between the skyrmion Hall angle and the thermal gradient is an unignorable factor in applying spintronic devices.

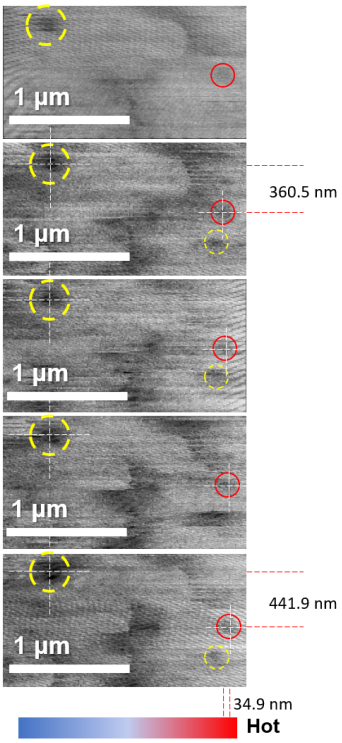

Figure 8.1: The skyrmion-like magnetic pattern (red circle) displacement after three pulses of 30 mA current.

Bibliography

[1] Lionel Juen Jin Tan, Daniel Swee Guan Ong, Jo Shien Ng, Chee Hing Tan, Stephen K. Jones, Yahong Qian, and John Paul Raj David. Temperature dependence of avalanche breakdown in inp and inalas. *IEEE Journal of Quantum Electronics*, 46:1153–1157, 2010. doi: 10.1109/JQE.2010.2044370. URL https://ieeexplore.ieee.org/document/5446447.

[2] Ya-Ju Lee, Yung-Chi Yao, Chun-Ying Huang, Tai-Yuan Lin, Li-Lien Cheng, Ching-Yun Liu, Mei-Tan Wang, and Jung-Min Hwang. High breakdown voltage in algan/gan hemts using algan/gan/algan quantum-well electron-blocking layers. *Nanoscale Research Letters*, 9:433, 2014. doi: 10.1186/1556-276X-9-433. URL https://doi.org/10.1186/1556-276X-9-433.

[3] J. Maserjian. Tunneling in thin MOS structures. *Journal of Vacuum Science and Technology*, 11:996–1003, 1974. doi: 10.1116/1.1318719. URL https://doi.org/10.1116/1.1318719.

[4] Gou Shinkai, Toshiaki Hayashi, Takeshi Ota, and Toshimasa Fujisawa. Correlated coherent oscillations in coupled semiconductor charge qubits. *Phys. Rev. Lett.*, 103:056802, 2009. doi: 10.1103/PhysRevLett.103.056802. URL https://link.aps.org/doi/10.1103/PhysRevLett.103.056802.

[5] Zhe Cheng and Samuel Graham. 16 - room-temperature bonded thermally conductive semiconductor interfaces. In Marko J. Tadjer and Travis J. Anderson, editors, *Thermal Management of Gallium Nitride Electronics*, Woodhead Publishing Series in Electronic and Optical Materials, pages 359–377. Woodhead Publishing, 2022. ISBN 978-0-12-821084-0. doi: https://doi.

org/10.1016/B978-0-12-821084-0.00008-1. URL https://www.sciencedirect.com/science/article/pii/B9780128210840000081.

[6] Iea. Energy efficiency 2019 - analysis. URL https://www.iea.org/reports/energy-efficiency-2019.

[7] Atsufumi Hirohata and Koki Takanashi. Future perspectives for spintronic devices. *Journal of Physics D: Applied Physics*, 47:193001, 2014. doi: 10.1088/0022-3727/47/19/193001. URL https://dx.doi.org/10.1088/0022-3727/47/19/193001.

[8] KL Wang, JG Alzate, and P Khalili Amiri. Low-power non-volatile spintronic memory: Stt-ram and beyond. *Journal of Physics D: Applied Physics*, 46:074003, 2013. doi: 10.1088/0022-3727/46/7/074003. URL https://dx.doi.org/10.1088/0022-3727/46/7/074003.

[9] Robert Perricone, Ibrahim Ahmed, Zhaoxin Liang, Meghna G Mankalale, X Sharon Hu, Chris H Kim, Michael Niemier, Sachin S Sapatnekar, and Jian-Ping Wang. Advanced spintronic memory and logic for non-volatile processors. In *Design, Automation & Test in Europe Conference & Exhibition (DATE), 2017*, pages 972–977. IEEE, 2017. doi: 10.23919/DATE.2017.7927132. URL https://ieeexplore.ieee.org/abstract/document/7927132.

[10] Atsufumi Hirohata, Keisuke Yamada, Yoshinobu Nakatani, Ioan-Lucian Prejbeanu, Bernard DiÃ©ny, Philipp Pirro, and Burkard Hillebrands. Review on spintronics: Principles and device applications. *Journal of Magnetism and Magnetic Materials*, 509:166711, 2020. doi: https://doi.org/10.1016/j.jmmm.2020.166711. URL https://www.sciencedirect.com/science/article/pii/S0304885320302353.

[11] A. N. Bogdanov and U. K. Rößler. Chiral symmetry breaking in magnetic thin films and multilayers. *Phys. Rev. Lett.*, 87:037203, 2001. doi: 10.1103/PhysRevLett.87.037203. URL https://link.aps.org/doi/10.1103/PhysRevLett.87.037203.

[12] Niklas Romming, André Kubetzka, Christian Hanneken, Kirsten von Bergmann, and Roland Wiesendanger. Field-dependent size and shape of single magnetic skyrmions. *Phys. Rev. Lett.*, 114:177203, 2015. doi: 10.1103/PhysRevLett.114.177203. URL https://link.aps.org/doi/10.1103/PhysRevLett.114.177203.

[13] Xichao Zhang, Yan Zhou, Kyung Mee Song, Tae-Eon Park, Jing Xia, Motohiko Ezawa, Xiaoxi Liu, Weisheng Zhao, Guoping Zhao, and Seonghoon Woo. Skyrmion-electronics: writing, deleting, reading and processing magnetic skyrmions toward spintronic applications. *Journal of Physics: Condensed Matter*, 32, 2020. doi: 10.1088/1361-648x/ab5488. URL https://doi.org/10.1088%2F1361-648x%2Fab5488.

[14] R. Saha, T. Srivastava, A.K.and Ma, and et al. Intrinsic stability of magnetic anti-skyrmions in the tetragonal inverse heusler compound mn1.4pt0.9pd0.1sn. *Nat Commun*, 10, 2019.

[15] Karin Everschor, Markus Garst, R. A. Duine, and Achim Rosch. Current-induced rotational torques in the skyrmion lattice phase of chiral magnets. *Phys. Rev. B*, 84:064401, 2011. doi: 10.1103/PhysRevB.84.064401. URL https://link.aps.org/doi/10.1103/PhysRevB.84.064401.

[16] T.H.R. Skyrme. A unified field theory of mesons and baryons. *Nuclear Phys.*, 31: 556 – 569, 1962. doi: https://doi.org/10.1016/0029-5582(62)90775-7. URL http://www.sciencedirect.com/science/article/pii/0029558262907757.

[17] David C. Wright and N. David Mermin. Crystalline liquids: the blue phases. *Rev. Mod. Phys.*, 61:385–432, 1989. doi: 10.1103/RevModPhys.61.385. URL https://link.aps.org/doi/10.1103/RevModPhys.61.385.

[18] U. Rößler, A. Bogdanov, and C. Pfleiderer. Spontaneous skyrmion ground states in magnetic metals. *Nature*, 442:797–801, 2006. doi: 10.1038/nature05056. URL https://doi.org/10.1038/nature05056.

[19] S. Mühlbauer, B. Binz, F. Jonietz, C. Pfleiderer, A. Rosch, A. Neubauer, R. Georgii, and P. Böni. Skyrmion lattice in a chiral magnet. *Science*, 323:915–919, 2009. doi: 10.1126/science.1166767. URL https://www.science.org/doi/abs/10.1126/science.1166767.

[20] Weiwei Wang, Maximilian Albert, Marijan Beg, Marc-Antonio Bisotti, Dmitri Chernyshenko, David Cortés-Ortuño, Ian Hawke, and Hans Fangohr. Magnon-driven domain-wall motion with the Dzyaloshinskii-Moriya interaction. *Phys. Rev. Lett.*, 114:087203, 2015. doi: 10.1103/PhysRevLett.114.087203. URL https://link.aps.org/doi/10.1103/PhysRevLett.114.087203.

[21] Dmitry A. Garanin, Daniel Capic, Senfu Zhang, Xixiang Zhang, and Eugene M. Chudnovsky. Writing skyrmions with a magnetic dipole. *Journal of Applied Physics*, 124:113901, 2018. doi: 10.1063/1.5044273. URL https://doi.org/10.1063/1.5044273.

[22] A. Wachowiak, J. Wiebe, M. Bode, O. Pietzsch, M. Morgenstern, and R. Wiesendanger. Direct observation of internal spin structure of magnetic vortex cores. *Science*, 298:577–580, 2002. doi: 10.1126/science.1075302. URL https://science.sciencemag.org/content/298/5593/577.

[23] S. X. Huang and C. L. Chien. Extended skyrmion phase in epitaxial FeGe(111) thin films. *Phys. Rev. Lett.*, 108:267201, 2012. doi: 10.1103/PhysRevLett.108.267201. URL https://link.aps.org/doi/10.1103/PhysRevLett.108.267201.

[24] Suzuki Takao. A study of magnetization distribution of submicron bubbles in sputtered ho-co thin films. *Journal of Magnetism and Magnetic Materials*, 31-34:1009 – 1010, 1983. doi: https://doi.org/10.1016/0304-8853(83)90772-2. URL http://www.sciencedirect.com/science/article/pii/0304885383907722.

[25] I. Dzyaloshinsky. A thermodynamic theory of 'weak' ferromagnetism of antiferromagnetics. *Journal of Physics and Chemistry of Solids*, 4:241 – 255, 1958. doi: https://doi.org/10.1016/0022-3697(58)90076-3. URL http://www.sciencedirect.com/science/article/pii/0022369758900763.

[26] Tsuyoshi Okubo, Sungki Chung, and Hikaru Kawamura. Multiple-q states and the skyrmion lattice of the triangular-lattice heisenberg antiferromagnet under magnetic fields. *Phys. Rev. Lett.*, 108:017206, 2012. doi: 10.1103/PhysRevLett.108.017206. URL https://link.aps.org/doi/10.1103/PhysRevLett.108.017206.

[27] Stefan Heinze, Kirsten von Bergmann, Matthias Menzel, Jens Brede, Andre Kubetzka, Roland Wiesendanger, Gustav Bihlmayer, and Stefan Bl/"ugel. Spontaneous atomic-scale magnetic skyrmion lattice in two dimensions. *Nat Phys*, 7:713–718, 2011. doi: 10.1038/nphys2045. URL https://doi.org/10.1038/nphys2045.

[28] Chen Gong. Skyrmion hall effect. *Nature Physics*, 13:112–113, 2017. doi: 10.1038/nphys4030. URL https://doi.org/10.1038/nphys4030.

[29] Michael Stone. Magnus force on skyrmions in ferromagnets and quantum hall systems. *Phys. Rev. B*, 53, Jun 1996. doi: 10.1103/PhysRevB.53.16573. URL https://link.aps.org/doi/10.1103/PhysRevB.53.16573.

[30] Xichao Zhang, Yan Zhou, and Motohiko Ezawa. Magnetic bilayer-skyrmions without skyrmion hall effect. *Nature Communications*, 7(1):10293, 2016. doi: 10.1038/ncomms10293. URL https://doi.org/10.1038/ncomms10293.

[31] Joseph Barker and Oleg A. Tretiakov. Static and dynamical properties of antiferromagnetic skyrmions in the presence of applied current and temperature. *Phys. Rev. Lett.*, 116:147203, 2016. doi: 10.1103/PhysRevLett.116.147203. URL https://link.aps.org/doi/10.1103/PhysRevLett.116.147203.

[32] Shi-Zeng Lin, Charles Reichhardt, Cristian D. Batista, and Avadh Saxena. Particle model for skyrmions in metallic chiral magnets: Dynamics, pinning, and creep. *Phys. Rev. B*, 87:214419, 2013. doi: 10.1103/PhysRevB.87.214419. URL https://link.aps.org/doi/10.1103/PhysRevB.87.214419.

[33] Takaaki Dohi, Samik DuttaGupta, Shunsuke Fukami, and Hideo Ohno. Formation and current-induced motion of synthetic antiferromagnetic skyrmion bubbles. *Nature Communications*, 10:5153, 2019. doi: 10.1038/s41467-019-13182-6. URL https://doi.org/10.1038/s41467-019-13182-6.

[34] A. Leonov and M. Mostovoy. Multiply periodic states and isolated skyrmions in an anisotropic frustrated magnet. *Nat Commun*, 6, 2015. doi: 10.1038/ncomms9275. URL https://doi.org/10.1038/ncomms9275.

[35] Wanjun Jiang, Pramey Upadhyaya, Wei Zhang, Guoqiang Yu, M. Benjamin Jungfleisch, Frank Y. Fradin, John E. Pearson, Yaroslav Tserkovnyak, Kang L. Wang, Olle Heinonen, Suzanne G. E. te Velthuis, and Axel Hoffmann. Blowing magnetic skyrmion bubbles. *Science*, 349:283–286, 2015. doi: 10.1126/science.aaa1442. URL https://www.science.org/doi/abs/10.1126/science.aaa1442.

[36] N S Kiselev, A N Bogdanov, R Schäfer, and U K Rößler. Chiral skyrmions in thin magnetic films: new objects for magnetic storage technologies. *Journal of Physics D: Applied Physics*, 44:392001, 2011. doi: 10.1088/0022-3727/44/39/392001. URL https://doi.org/10.1088%2F0022-3727%2F44%2F39%2F392001.

[37] Andrew S. Westover, Karine Chesnel, Kelsey Hatch, Philip Salter, and Olav Hellwig. Enhancement of magnetic domain topologies in co/pt thin films by fine tuning the magnetic field path throughout the hysteresis loop. *Journal of Magnetism and Magnetic Materials*, 399:164–169, 2016. doi: https://doi.org/10.1016/j.jmmm.2015.09.040. URL https://www.sciencedirect.com/science/article/pii/S0304885315305904.

[38] S. Andrieu, T. Hauet, M. Gottwald, A. Rajanikanth, L. Calmels, A. M. Bataille, F. Montaigne, S. Mangin, E. Otero, P. Ohresser, P. Le Fèvre, F. Bertran, A. Resta, A. Vlad, A. Coati, and Y. Garreau. Co/ni multilayers for spintronics: High spin polarization and tunable magnetic anisotropy. *Phys. Rev. Mater.*, 2:064410, 2018. doi: 10.1103/PhysRevMaterials.2.064410. URL https://link.aps.org/doi/10.1103/PhysRevMaterials.2.064410.

[39] D.C. Ralph and M.D. Stiles. Spin transfer torques. *Journal of Magnetism and Magnetic Materials*, 320:1190–1216, 2008. doi: https://doi.org/10.1016/j.jmmm.2007.12.019. URL https://www.sciencedirect.com/science/article/pii/S0304885307010116.

[40] A. Manchon and S. Zhang. Theory of spin torque due to spin-orbit coupling. *Phys. Rev. B*, 79:094422, Mar 2009. doi: 10.1103/PhysRevB.79.094422. URL https://link.aps.org/doi/10.1103/PhysRevB.79.094422.

[41] F. Jonietz, S. Mühlbauer, C. Pfleiderer, A. Neubauer, W. Münzer, A. Bauer, T. Adams, R. Georgii, P. Böni, R. A. Duine, K. Everschor, M. Garst, and A. Rosch. Spin transfer torques in mnsi at ultralow current densities. *Science*, 330:1648–1651, 2010. doi: 10.1126/science.1195709. URL https://science.sciencemag.org/content/330/6011/1648.

[42] Jing Xia, Yangqi Huang, Xichao Zhang, Wang Kang, Chentian Zheng, Xiaoxi Liu, Weisheng Zhao, and Yan Zhou. A microwave field-driven transistor-like skyrmionic device with the microwave current-assisted skyrmion creation. *J. Appl. Phys.*, 122:153901, 2017. doi: 10.1063/1.4999013. URL https://doi.org/10.1063/1.4999013.

[43] Ken ichi Uchida, Hiroto Adachi, Yousuke Kajiwara, Sadamichi Maekawa, and Eiji Saitoh. Chapter one - spin-wave spin current in magnetic insu-

lators. In Mingzhong Wu and Axel Hoffmann, editors, *Recent Advances in Magnetic Insulators â€“ From Spintronics to Microwave Applications*, volume 64 of *Solid State Physics*, pages 1–27. Academic Press, 2013. doi: https://doi.org/10.1016/B978-0-12-408130-7.00001-0. URL https://www.sciencedirect.com/science/article/pii/B9780124081307000010.

[44] Sadamichi Maekawa, Takashi Kikkawa, Hiroyuki Chudo, Junâ€™ichi Ieda, and Eiji Saitoh. Spin and spin currentâ€”From fundamentals to recent progress. *Journal of Applied Physics*, 133:020902, 01 2023. doi: 10.1063/5.0133335. URL https://doi.org/10.1063/5.0133335.

[45] J. Klos, Igor Lyubchanskii, Maciej Krawczyk, Pawel Gruszecki, Szymon Mieszczak, Justyna RychÅ‚y, Yuliya Dadoenkova, and N. Dadoenkova. *Magnonics and Confinement of Light in Photonicâ€“Magnonic Crystals*. 01 2021.

[46] Yuanyuan Jiang, H. Y. Yuan, Z.-X. Li, Zhenyu Wang, H. W. Zhang, Yunshan Cao, and Peng Yan. Twisted magnon as a magnetic tweezer. *Phys. Rev. Lett.*, 124:217204, 2020. doi: 10.1103/PhysRevLett.124.217204. URL https://link.aps.org/doi/10.1103/PhysRevLett.124.217204.

[47] Phoebe Tengdin, Benoit Truc, Alexey Sapozhnik, Simone Gargiulo, Ivan Madan, Thomas Schoenenberger, Priya R. Baral, Ping Che, Arnaud Magrez, Dirk Grundler, Henrik M. RÃ¸nnow, Thomas Lagrange, and Fabrizio Carbone. Imaging the controllable rotation of a skyrmion crystal driven by femtosecond laser pulses, 2021. URL https://www.mrs.org/meetings-events/presentation/2022_mrs_spring_meeting/2022_mrs_spring_meeting-3669538.

[48] Xiuzhen Yu, Fumitaka Kagawa, Shinichiro Seki, and et al. Real-space observations of 60-nm skyrmion dynamics in an insulating magnet under low heat flow. *Nature Commun.*, 12:5079, 2021. doi: 10.1038/s41467-021-25291-2. URL https://doi.org/10.1038/s41467-021-25291-2.

[49] Xichao Zhang, Motohiko Ezawa, Dun Xiao, G P Zhao, Yaowen Liu, and Yan Zhou. All-magnetic control of skyrmions in nanowires by a spin wave. *Nanotechnology*, 26:225701, 2015. doi: 10.1088/0957-4484/26/22/225701. URL https://dx.doi.org/10.1088/0957-4484/26/22/225701.

[50] Lingling Song, Huanhuan Yang, Bo Liu, Hao Meng, Yunshan Cao, and Peng Yan. A spin-wave driven skyrmion diode under transverse magnetic fields. *J. Magn. Magn. Mater.*, 532:167975, 2021. doi: https://doi.org/10.1016/j.jmmm.2021.167975. URL https://www.sciencedirect.com/science/article/pii/S0304885321002511.

[51] Xiaochen Shen, Rongzhi Zhao, Lianze Ji, Chenglong Hu, Wenling Ren, Wenchao Chen, Yixing Li, Jian Zhang, Xuefeng Zhang, and Xinglong Dong. Breaking the topological protection of target skyrmions by the excitation of spin wave modes under microwave magnetic field. *Journal of Magnetism and Magnetic Materials*, 541:168521, 2022. doi: https://doi.org/10.1016/j.jmmm.2021.168521. URL https://www.sciencedirect.com/science/article/pii/S0304885321007782.

[52] S. Seki, M. Garst, J. Waizner, and et al. Propagation dynamics of spin excitations along skyrmion strings. *Nat Commun*, 11:256, 2020. doi: 10.1038/s41467-019-14095-0. URL https://doi.org/10.1038/s41467-019-14095-0.

[53] Eleonora Raimondo, Elias Saugar, Joseph Barker, Davi Rodrigues, Anna Giordano, Mario Carpentieri, Wanjun Jiang, Oksana Chubykalo-Fesenko, Riccardo Tomasello, and Giovanni Finocchio. Temperature-gradient-driven magnetic skyrmion motion. *Phys. Rev. Appl.*, 18:024062, 2022. doi: 10.1103/PhysRevApplied.18.024062. URL https://link.aps.org/doi/10.1103/PhysRevApplied.18.024062.

[54] Serban Lepadatu. All-optical magnetothermoelastic skyrmion motion. *Phys. Rev. Appl.*, 19:044036, 2023. doi: 10.1103/PhysRevApplied.19.044036. URL https://link.aps.org/doi/10.1103/PhysRevApplied.19.044036.

[55] M A S Akanda, M T Islam, and X R Wang. Role of ssw on thermal-gradient induced domain-wall dynamics. *Journal of Physics: Condensed Matter*, 35:315701, 2023. doi: 10.1088/1361-648X/accfdc. URL https://dx.doi.org/10.1088/1361-648X/accfdc.

[56] LiZhi Yi, Dongchao Yang, Min Liu, Hua-Hua Fu, Linjie Ding, Yunli Xu, Bingbing Zhang, Liqing Pan, and John Q. Xiao. Concepts of spin seebeck effect in ferromagnetic metals. *Advanced Functional Materials*, 30:2004024, 2020. doi: https://doi.org/10.1002/adfm.202004024. URL https://onlinelibrary.wiley.com/doi/abs/10.1002/adfm.202004024.

[57] Wanjun Jiang, Pramey Upadhyaya, Yabin Fan, Jing Zhao, Minsheng Wang, Li-Te Chang, Murong Lang, Kin L. Wong, Mark Lewis, Yen-Ting Lin, Jianshi Tang, Sergiy Cherepov, Xuezhi Zhou, Yaroslav Tserkovnyak, Robert N. Schwartz, and Kang L. Wang. Direct imaging of thermally driven domain wall motion in magnetic insulators. *Phys. Rev. Lett.*, 110:177202, 2013. doi: 10.1103/PhysRevLett.110.177202. URL https://link.aps.org/doi/10.1103/PhysRevLett.110.177202.

[58] Minori Goto, Hikaru Nomura, and Yoshishige Suzuki. Stochastic skyrmion dynamics under alternating magnetic fields. *Journal of Magnetism and Magnetic Materials*, 536:167974, 2021. doi: https://doi.org/10.1016/j.jmmm.2021.167974. URL https://www.sciencedirect.com/science/article/pii/S030488532100250X.

[59] Chung T. Ma, Timothy Q. Hartnett, Wei Zhou, Prasanna V. Balachandran, and S. Joseph Poon. Tunable magnetic skyrmions in ferrimagnetic Mn4N. *Applied Physics Letters*, 119:192406, 2021. doi: 10.1063/5.0066375. URL https://doi.org/10.1063/5.0066375.

[60] Iu. V. Vetrova, M. Zelent, J. Å oltÃ½s, V. A. Gubanov, A. V. Sadovnikov, T. Å cepka, J. DÃ©rer, R. Stoklas, V. Cambel, and M. Mruczkiewicz. Investigation of self-nucleated skyrmion states in the ferromagnetic/nonmagnetic multilayer dot. *Applied Physics Letters*, 118:212409, 2021. doi: 10.1063/5.0045835. URL https://doi.org/10.1063/5.0045835.

[61] Luis Flacke, Valentin Ahrens, Simon Mendisch, Lukas Körber, Tobias Böttcher, Elisabeth Meidinger, Misbah Yaqoob, Manuel Müller, Lukas Liensberger, Attila Kákay, Markus Becherer, Philipp Pirro, Matthias Althammer, Stephan Geprägs, Hans Huebl, Rudolf Gross, and Mathias Weiler. Robust formation of nanoscale magnetic skyrmions in easy-plane anisotropy thin film multilayers with low damping. *Phys. Rev. B*, 104:L100417, 2021. doi: 10.1103/PhysRevB.104.L100417. URL https://link.aps.org/doi/10.1103/PhysRevB.104.L100417.

[62] Brindaban Ojha, Sougata Mallick, Sujit Panigrahy, Minaxi Sharma, André Thiaville, Stanislas Rohart, and Subhankar Bedanta. Driving skyrmions with low threshold current density in pt/cofeb thin film. *Physica Scripta*, 98:035819, 2023. doi: 10.1088/1402-4896/acb862. URL https://dx.doi.org/10.1088/1402-4896/acb862.

[63] Alexander Fernández Scarioni, Craig Barton, Héctor Corte-León, Sibylle Sievers, Xiukun Hu, Fernando Ajejas, William Legrand, Nicolas Reyren, Vincent Cros, Olga Kazakova, and Hans W. Schumacher. Thermoelectric signature of individual skyrmions. *Phys. Rev. Lett.*, 126:077202, 2021. doi: 10.1103/PhysRevLett.126.077202. URL https://link.aps.org/doi/10.1103/PhysRevLett.126.077202.

[64] Anthony K. C. Tan, Pin Ho, James Lourembam, Lisen Huang, Hang Khume Tan, Cynthia J. O. Reichhardt, Charles Reichhardt, and Anjan Soumyanarayanan. Visualizing the strongly reshaped skyrmion hall effect in multilayer wire devices. *Nature Communications*, 12:4252, 2021. doi: 10.1038/s41467-021-24114-8. URL https://doi.org/10.1038/s41467-021-24114-8.

[65] Andrada-Oana Mandru, Oğuz Yıldırım, Riccardo Tomasello, Paul Heistracher, Marcos Penedo, Anna Giordano, Dieter Suess, Giovanni Finocchio, and Hans Josef Hug. Coexistence of distinct skyrmion phases observed in hybrid ferromagnetic/ferrimagnetic multilayers. *Nature Communications*, 11: 6365, 2020. doi: 10.1038/s41467-020-20025-2. URL https://doi.org/10.1038/s41467-020-20025-2.

[66] Jakub Zázvorka, Florian Jakobs, Daniel Heinze, Niklas Keil, Sascha Kromin, Samridh Jaiswal, Kai Litzius, Gerhard Jakob, Peter Virnau, Daniele Pinna, Karin Everschor-Sitte, Levente Rózsa, Andreas Donges, Ulrich Nowak, and Mathias Kläui. Thermal skyrmion diffusion used in a reshuffler device. *Nature Nanotechnology*, 14:658–661, 2019. doi: 10.1038/s41565-019-0436-8. URL https://doi.org/10.1038/s41565-019-0436-8.

[67] Yongze Cao, Yue Zhao, Jin Tang, Haifeng Du, Yan Zhou, and Hitoshi Saito. Direct visualization of magnetic domain wall motion in nd-fe-b magnets by alternating magnetic force microscopy using co-gdox superparamagnetic tip. *Ultramicroscopy*, 212:112980, 2020. doi: https://doi.org/10.1016/j.ultramic.2020.112980. URL https://www.sciencedirect.com/science/article/pii/S0304399119302256.

[68] Lingwen Kong, Lan Bo, Rongzhi Zhao, Chenglong Hu, Lianze Ji, Yanhui Zhang, and Xuefeng Zhang. Linear dependence of skyrmion velocity on response resonance frequency of local magnetization. *Appl. Phys. Lett.*, 116:192407, 2020. doi: 10.1063/5.0004649. URL https://doi.org/10.1063/5.0004649.

[69] Peng Yan, Akashdeep Kamra, Yunshan Cao, and Gerrit E. W. Bauer. Angular and linear momentum of excited ferromagnets. *Phys. Rev. B*, 88:144413, 2013. doi: 10.1103/PhysRevB.88.144413. URL https://link.aps.org/doi/10.1103/PhysRevB.88.144413.

[70] Xi-Guang Wang, Guang-Hua Guo, Guang-Fu Zhang, Yao-Zhuang Nie, and Qing-Lin Xia. Spin-wave resonance reflection and spin-wave induced domain wall displacement. *J. Appl. Phys.*, 113:213904, 2013. doi: 10.1063/1.4808298. URL https://doi.org/10.1063/1.4808298.

[71] M. J. Donahue and D. G. Porter. OOMMF user's guide, version 1.0. Technical report, National Institute of Standards and Technology, Gaithersburg, MD, 1999. URL http://math.nist.gov/oommf.

[72] S. Rohart and A. Thiaville. Skyrmion confinement in ultrathin film nanostructures in the presence of Dzyaloshinskii-Moriya interaction. *Phys. Rev. B*, 88:184422, 2013. doi: 10.1103/PhysRevB.88.184422. URL https://link.aps.org/doi/10.1103/PhysRevB.88.184422.

[73] Stephen Blundell. *Magnetism in Condensed Matter*. University of Oxford, 2001.

[74] Andrew J. Newell, Wyn Williams, and David J. Dunlop. A generalization of the demagnetizing tensor for nonuniform magnetization. *Journal of Geophysical Research: Solid Earth*, 98:9551–9555, 1993. doi: https://doi.org/10.1029/93JB00694. URL https://agupubs.onlinelibrary.wiley.com/doi/abs/10.1029/93JB00694.

[75] A. A. Thiele. Steady-state motion of magnetic domains. *Phys. Rev. Lett.*, 30:230–233, 1973. doi: 10.1103/PhysRevLett.30.230. URL https://link.aps.org/doi/10.1103/PhysRevLett.30.230.

[76] R. Tomasello, E. Martinez, R. Zivieri, L. Torres, M. Carpentieri, and G. Finocchio. A strategy for the design of skyrmion racetrack memories. *Scientific Reports*, 4:6784, 2014. doi: 10.1038/srep06784. URL https://doi.org/10.1038/srep06784.

[77] O. A. Tretiakov, D. Clarke, Gia-Wei Chern, Ya. B. Bazaliy, and O. Tchernyshyov. Dynamics of domain walls in magnetic nanostrips. *Phys. Rev. Lett.*, 100:127204, 2008. doi: 10.1103/PhysRevLett.100.127204. URL https://link.aps.org/doi/10.1103/PhysRevLett.100.127204.

[78] Pramey Upadhyaya, Guoqiang Yu, Pedram Khalili Amiri, and Kang L. Wang. Electric-field guiding of magnetic skyrmions. *Phys. Rev. B*, 92:134411, 2015. doi: 10.1103/PhysRevB.92.134411. URL https://link.aps.org/doi/10.1103/PhysRevB.92.134411.

[79] Wanjun Jiang, Xichao Zhang, Guoqiang Yu, Wei Zhang, Xiao Wang, M. Benjamin Jungfleisch, John E. Pearson, Xuemei Cheng, Olle Heinonen, Kang L. Wang, Yan Zhou, Axel Hoffmann, and Suzanne G. E. te Velthuis. Direct observation of the skyrmion Hall effect. *Nature Phys.*, 13:162–169, 2017. doi: 10.1038/nphys3883. URL https://doi.org/10.1038/nphys3883.

[80] Carles Navau, Nuria Del-Valle, and Alvaro Sanchez. Interaction of isolated skyrmions with point and linear defects. *J. Magn. Magn. Mater.*, 465: 709–715, 2018. doi: https://doi.org/10.1016/j.jmmm.2018.06.044. URL https://www.sciencedirect.com/science/article/pii/S0304885318311533.

[81] Xichao Zhang, Jan Müller, Jing Xia, Markus Garst, Xiaoxi Liu, and Yan Zhou. Motion of skyrmions in nanowires driven by magnonic momentum-transfer forces. *New J. Phys.*, 19:065001, 2017. doi: 10.1088/1367-2630/aa6b70. URL https://dx.doi.org/10.1088/1367-2630/aa6b70.

[82] Carles Navau, Nuria Del-Valle, and Alvaro Sanchez. Analytical trajectories of skyrmions in confined geometries: Skyrmionic racetracks and nano-oscillators. *Phys. Rev. B*, 94:184104, 2016. doi: 10.1103/PhysRevB.94.184104. URL https://link.aps.org/doi/10.1103/PhysRevB.94.184104.

[83] Sarah Schroeter and Markus Garst. Scattering of high-energy magnons off a magnetic skyrmion. *Low Temperature Physics*, 41:817–825, 2015. doi: 10.1063/1.4932356. URL https://doi.org/10.1063/1.4932356.

[84] Christoph Schütte and Markus Garst. Magnon-skyrmion scattering in chiral magnets. *Phys. Rev. B*, 90:094423, 2014. doi: 10.1103/PhysRevB.90.094423. URL https://link.aps.org/doi/10.1103/PhysRevB.90.094423.

[85] P. Yan, X. S. Wang, and X. R. Wang. All-magnonic spin-transfer torque and domain wall propagation. *Phys. Rev. Lett.*, 107:177207, 2011. doi: 10.1103/PhysRevLett.107.177207. URL https://link.aps.org/doi/10.1103/PhysRevLett.107.177207.

[86] X. S. Wang, H. Y. Yuan, and X. R. Wang. A theory on skyrmion size. *Commun. Phys.*, 1:31, 2018. doi: 10.1038/s42005-018-0029-0. URL https://doi.org/10.1038/s42005-018-0029-0.

[87] Hans-Benjamin Braun. Fluctuations and instabilities of ferromagnetic domain-wall pairs in an external magnetic field. *Phys. Rev. B*, 50:16485–16500, 1994. doi: 10.1103/PhysRevB.50.16485. URL https://link.aps.org/doi/10.1103/PhysRevB.50.16485.

[88] A.M. Kosevich, B.A. Ivanov, and A.S. Kovalev. Magnetic solitons. *Physics Reports*, 194:117–238, 1990. doi: https://doi.org/10.1016/0370-1573(90)90130-T. URL https://www.sciencedirect.com/science/article/pii/037015739090130T.

[89] Zhengyi Li, Mangyuan Ma, Zhendong Chen, Kaile Xie, and Fusheng Ma. Interaction between magnon and skyrmion: Toward quantum magnonics. *Journal of Applied Physics*, 132:210702, 12 2022. doi: 10.1063/5.0121314. URL https://doi.org/10.1063/5.0121314.

[90] Sai Li, Jing Xia, Xichao Zhang, Motohiko Ezawa, Wang Kang, Xiaoxi Liu, Yan Zhou, and Weisheng Zhao. Dynamics of a magnetic skyrmionium driven by spin waves. *Appl. Phys. Lett.*, 112:142404, 2018. doi: 10.1063/1.5026632. URL https://doi.org/10.1063/1.5026632.

[91] Junichi Iwasaki, Wataru Koshibae, and Naoto Nagaosa. Colossal spin transfer torque effect on skyrmion along the edge. *Nano Lett.*, 14:4432–4437, 2014. doi: https://doi.org/10.1021/nl501379k. URL https://pubmed.ncbi.nlm.nih.gov/24988528/.

[92] X. S. Wang and X. R. Wang. Thermodynamic theory for thermal-gradient-driven domain-wall motion. *Phys. Rev. B*, 90:014414, 2014. doi: 10.1103/PhysRevB.90.014414. URL https://link.aps.org/doi/10.1103/PhysRevB.90.014414.

[93] N. L. Schryer and L. R. Walker. The motion of 180Â° domain walls in uniform dc magnetic fields. *Journal of Applied Physics*, 45:5406–5421, 2003. doi: 10.1063/1.1663252. URL https://doi.org/10.1063/1.1663252.

[94] A. Mougin, M. Cormier, J. P. Adam, P. J. Metaxas, and J. FerrÃ©. Domain wall mobility, stability and walker breakdown in magnetic nanowires. *Europhysics*

Letters, 78:57007, 2007. doi: 10.1209/0295-5075/78/57007. URL https://dx.doi.org/10.1209/0295-5075/78/57007.

[95] Neil W Ashcroft and N David Mermin. *Solid state physics*. Cengage Learning, 2022.

[96] Mark Johnson and R. H. Silsbee. Thermodynamic analysis of interfacial transport and of the thermomagnetoelectric system. *Phys. Rev. B*, 35:4959–4972, Apr 1987. doi: 10.1103/PhysRevB.35.4959. URL https://link.aps.org/doi/10.1103/PhysRevB.35.4959.

[97] Hiroto Adachi, Ken-ichi Uchida, Eiji Saitoh, and Sadamichi Maekawa. Theory of the spin seebeck effect. *Reports on Progress in Physics*, 76(3):036501, February 2013. doi: 10.1088/0034-4885/76/3/036501. URL http://dx.doi.org/10.1088/0034-4885/76/3/036501.

[98] Oleksandr Tsyplyatyev, Oleksiy Kashuba, and Vladimir I. Fal'ko. Thermally excited spin current and giant magnetothermopower in metals with embedded ferromagnetic nanoclusters. *Phys. Rev. B*, 74:132403, 2006. doi: 10.1103/PhysRevB.74.132403. URL https://link.aps.org/doi/10.1103/PhysRevB.74.132403.

[99] K. Uchida, S. Takahashi, K. Harii, J. Ieda, W. Koshibae, K. Ando, S. Maekawa, and E. Saitoh. Observation of the spin seebeck effect. *Nature*, 455:778–781, 2008. doi: 10.1038/nature07321. URL https://doi.org/10.1038/nature07321.

[100] K. Uchida, J. Xiao, H. Adachi, J. Ohe, S. Takahashi, J. Ieda, T. Ota, Y. Kajiwara, H. Umezawa, H. Kawai, G. E. W. Bauer, S. Maekawa, and E. Saitoh. Spin seebeck insulator. *Nature Materials*, 9:894–897, 2010. doi: 10.1038/nmat2856. URL https://doi.org/10.1038/nmat2856.

[101] Kjetil M.D. Hals, Arne Brataas, and Gerrit E.W. Bauer. Thermopower and thermally induced domain wall motion in (ga, mn)as. *Solid State Communications*, 150:461–465, 2010. doi: https://doi.org/10.1016/j.ssc.2010.01.023. URL https://www.sciencedirect.com/science/article/pii/S003810981000030X. Spin Caloritronics.

[102] Jairo Sinova. Thinks globally but acts locally. *Nature Materials*, 9:880–881, 2010. doi: 10.1038/nmat2880. URL https://doi.org/10.1038/nmat2880.

[103] D. Hinzke and U. Nowak. Domain wall motion by the magnonic spin seebeck effect. *Phys. Rev. Lett.*, 107:027205, 2011. doi: 10.1103/PhysRevLett.107.027205. URL https://link.aps.org/doi/10.1103/PhysRevLett.107.027205.

[104] Alexey A. Kovalev and Yaroslav Tserkovnyak. Thermomagnonic spin transfer and peltier effects in insulating magnets. *Europhysics Letters*, 97:67002, 2012. doi: 10.1209/0295-5075/97/67002. URL https://dx.doi.org/10.1209/0295-5075/97/67002.

[105] Gang Lu, Steven L. Bernasek, and Jeffrey Schwartz. Oxidation of a polycrystalline titanium surface by oxygen and water. *Surface Science*, 458:80–90, 2000. doi: https://doi.org/10.1016/S0039-6028(00)00420-9. URL https://www.sciencedirect.com/science/article/pii/S0039602800004209.

[106] W. Vedder and D. A. Vermilyea. Aluminum + water reaction. *Trans. Faraday Soc.*, 65:561–584, 1969. doi: 10.1039/TF9696500561. URL http://dx.doi.org/10.1039/TF9696500561.

[107] S. Z. Chu, K. Wada, S. Inoue, and S. Todoroki. Formation and microstructures of anodic alumina films from aluminum sputtered on glass substrate. *Journal of The Electrochemical Society*, 149, 2002. doi: 10.1149/1.1480017. URL https://dx.doi.org/10.1149/1.1480017.

[108] D. Depla. The measurement and impact of negative oxygen ions during reactive sputter deposition. *Critical Reviews in Solid State and Materials Sciences*, 0:1–36, 2023. doi: 10.1080/10408436.2023.2258159. URL https://doi.org/10.1080/10408436.2023.2258159.

[109] Young-Woo Kim, Yonghyun Kim, Daechul Kim, Jong-Sik Kim, Jung-Sik Yoon, Suk Jae Yoo, and Bongju Lee. Development and characterization of toroidal magnetron sputtering system for thin films deposition. *Thin Solid Films*, 518:6650–6653, 2010. doi: https://doi.org/10.1016/j.tsf.2010.03.145. URL https://www.sciencedirect.com/science/article/pii/S0040609010004748. Proceedings of the 2nd International Conference on Microelectronics and Plasma Technology - ICMAP 2009.

[110] URL https://www.lesker.com/process-equipment-division/thin-film-systems/pro-line-pvd-75-deposition-platform.cfm.

[111] L-C Xu and C.A. Siedlecki. 4.18 surface texturing and control of bacterial adhesion. In Paul Ducheyne, editor, *Comprehensive Biomaterials II*, pages 303–320. Elsevier, Oxford, 2017. ISBN 978-0-08-100692-4. doi: https://doi.org/10.1016/B978-0-12-803581-8.09295-X. URL https://www.sciencedirect.com/science/article/pii/B978012803581809295X.

[112] Matthias KÃ¼hne. KLayout, 2021. URL https://www.klayout.de/. Version 0.27.

[113] Shubhava, A. Jayarama, Ganesh K. Kannarpady, Sangeeta Kale, Shriganesh Prabhu, and Richard Pinto. Chemical etching of glasses in hydrofluoric acid: A brief review. *Materials Today: Proceedings*, 55:46–51, 2022. doi: https://doi.org/10.1016/j.matpr.2021.12.110. URL https://www.sciencedirect.com/science/article/pii/S2214785321077865. 9th National Conference on Condensed Physics and Applications.

[114] G. C. Schwartz and P. M. Schaible. Reactive ion etching of silicon. *Journal of Vacuum Science and Technology*, 16:410–413, 03 1979. doi: 10.1116/1.569962. URL https://doi.org/10.1116/1.569962.

[115] June W Lau and Justin M Shaw. Magnetic nanostructures for advanced technologies: fabrication, metrology and challenges. *Journal of Physics D: Applied Physics*, 44:303001, 2011. doi: 10.1088/0022-3727/44/30/303001. URL https://dx.doi.org/10.1088/0022-3727/44/30/303001.

[116] Hirokazu Ito, Kouichi Hasegawa, Tomohiro Matsuki, and Shiro Kusumoto. Development of lift-off photoresists with unique bottom profile. In *2015 International Conference on Electronics Packaging and iMAPS All Asia Conference (ICEP-IAAC)*, pages 633–637, 2015. doi: 10.1109/ICEP-IAAC.2015.7111091. URL https://api.semanticscholar.org/CorpusID:43976159.

[117] Heinz Kiessig. Untersuchungen zur totalreflexion von röntgenstrahlen. *Annalen der Physik*, 402:715–768, 1931. doi: https://doi.org/10.1002/andp.19314020607. URL https://onlinelibrary.wiley.com/doi/abs/10.1002/andp.19314020607.

[118] Peter Lindley and D. Moss. Elements of x-ray crystallography by l. v. azaroff. *Acta Crystallographica Section A*, 26, 1970. doi: 10.1107/S0567739470001808. URL https://doi.org/10.1107/S0567739470001808.

[119] Aaron M. Miller, Mellie Lemon, Marisa A. Choffel, Sarah R. Rich, Fischer Harvel, and David C. Johnson. Extracting information from x-ray diffraction patterns containing laue oscillations. *Zeitschrift fÃ¼r Naturforschung B*, 77:313–322, 2022. doi: doi:10.1515/znb-2022-0020. URL https://doi.org/10.1515/znb-2022-0020.

[120] Matts Björck and Gabriella Andersson. Genx : an extensible x-ray reflectivity refinement program utilizing differential evolution. *Journal of applied crystallography*, 40:1174–1178, 2007. doi: 10.1107/S0021889807045086.

[121] Artur Glavic and Matts Björck. *GenX 3*: the latest generation of an established tool. *Journal of Applied Crystallography*, 55:1063–1071, 2022. doi: 10.1107/S1600576722006653. URL https://doi.org/10.1107/S1600576722006653.

[122] I. V. Soldatov and R. SchÃ¤fer. Selective sensitivity in Kerr microscopy. *Review of Scientific Instruments*, 88:073701, 2017. doi: 10.1063/1.4991820. URL https://doi.org/10.1063/1.4991820.

[123] W. Kuch, R. Schäfer, P. Fischer, and F. Hillebrecht. *Magnetic Microscopy of Layered Structures*. Springer, New York, 2015. doi: https://doi.org/10.1007/978-3-662-44532-7.

[124] J.B. Adams. Bonding energy models. In K.H. JÃ¼rgen Buschow, Robert W. Cahn, Merton C. Flemings, Bernhard Ilschner, Edward J. Kramer, Subhash Mahajan, and Patrick VeyssiÃ¨re, editors, *Encyclopedia of Materials: Science and Technology*, pages 763–767. Elsevier, Oxford, 2001. ISBN 978-0-08-043152-9. doi: https://doi.org/10.1016/B0-08-043152-6/00146-7. URL https://www.sciencedirect.com/science/article/pii/B0080431526001467.

[125] Senfu Zhang, Junwei Zhang, Qiang Zhang, Craig Barton, Volker Neu, Yuelei Zhao, Zhipeng Hou, Yan Wen, Chen Gong, Olga Kazakova, Wenhong Wang, Yong Peng, Dmitry A. Garanin, Eugene M. Chudnovsky, and Xixiang Zhang. Direct writing of room temperature and zero field skyrmion lattices by a scanning local magnetic field. *Applied Physics Letters*, 112:132405, 2018. doi: 10.1063/1.5021172. URL https://doi.org/10.1063/1.5021172.

[126] Diamond Light Source. Quantum Design MPMS (SQUID-VSM Magnetometer) - - Diamond Light Source. URL https://www.diamond.ac.uk/Instruments/Magnetic-Materials/MCL/squid-vsm.html.

[127] Quantum Design. Mpms 3 platform measurement options. . URL https://atl.qdusa.com/siteDocs/productBrochures/1500-103.pdf.

[128] Quantum Design. Featuring quantum design's magnetic property measurement system. . URL https://qdusa.com/siteDocs/appNotes/FundPrimer.pdf.

[129] Quantum Design. Vsm sample mounting techniques-aplication note 1096-306. *VSM sample mounting techniques*, . URL https://www.qdusa.com/siteDocs/appNotes/1096-306.pdf.

[130] Z. Boekelheide and C. L. Dennis. Artifacts in magnetic measurements of fluid samples. *AIP Advances*, 6:085201, 2016. doi: 10.1063/1.4960457. URL https://doi.org/10.1063/1.4960457.

[131] Quantum Design. Subtracting the sample holder background from diluted samples. Technical report, Service Note 1014-213. 69, 2002.

[132] Sidi Fu, Weilong Cui, Matthew Hu, Ruinan Chang, Michael J. Donahue, and Vitaliy Lomakin. Finite-difference micromagnetic solvers with the object-oriented micromagnetic framework on graphics processing units. *IEEE Transactions on Magnetics*, 52(4):1–9, 2016. doi: 10.1109/TMAG.2015.2503262.

[133] D. Suess, S. Koraltan, F. Slanovc, F. Bruckner, and C. Abert. Accurate finite-difference micromagnetics of magnets including rkky interaction: Analytical solution and comparison to standard micromagnetic codes. *Phys. Rev. B*, 107: 104424, Mar 2023. doi: 10.1103/PhysRevB.107.104424. URL https://link.aps.org/doi/10.1103/PhysRevB.107.104424.

[134] Thomas L. Gilbert. A lagrangian formulation of the gyromagnetic equation of the magnetization field. *Physical Review D*, 100:1243, 1955. URL https://api.semanticscholar.org/CorpusID:197507556.

[135] J.R. Dormand and P.J. Prince. A family of embedded runge-kutta formulae. *Journal of Computational and Applied Mathematics*, 6:19–26, 1980. doi: https://doi.org/10.1016/0771-050X(80)90013-3. URL https://www.sciencedirect.com/science/article/pii/0771050X80900133.

[136] C Tannous and J Gieraltowski. The stonerâ€“wohlfarth model of ferromagnetism. *European Journal of Physics*, 29:475, mar 2008. doi: 10.1088/0143-0807/29/3/008. URL https://dx.doi.org/10.1088/0143-0807/29/3/008.

[137] Marcos F. de Campos, Fernanda A. Sampaio da Silva, Elio A. Perigo, and JosÃ© A. de Castro. Stonerâ€“wohlfarth model for the anisotropic case. *Journal of Magnetism and Magnetic Materials*, 345:147–152, 2013. ISSN 0304-8853. doi: https://doi.org/10.1016/j.jmmm.2013.06.028. URL https://www.sciencedirect.com/science/article/pii/S0304885313004496.

[138] N. Satchell, T. Mitchell, P. M. Shepley, E. Darwin, B. J. Hickey, and G. Burnell. Pt and cob trilayer josephson π junctions with perpendicular magnetic anisotropy. *Scientific Reports*, 11:11173, May 2021. doi: 10.1038/s41598-021-90432-y. URL https://doi.org/10.1038/s41598-021-90432-y.

[139] M Fettach, A Hassini, A Hamdoun, and L Driouch. Magnetic study of amorphous fe91-xyxzr9 alloys. *Physica B: Condensed Matter*, 325:203 – 207, 2003. doi: https://doi.org/10.1016/S0921-4526(02)01525-9. URL http://www.sciencedirect.com/science/article/pii/S0921452602015259.

[140] N. Lenge and H. Kronmüller. Low temperature magnetization of sputtered amorphous fe-ni-b films. *physica status solidi (a)*, 95:621–633, 1986. doi: https://doi.org/10.1002/pssa.2210950232. URL https://onlinelibrary.wiley.com/doi/abs/10.1002/pssa.2210950232.

[141] M. Konc, P. Spisak, P. Kollar, P. Sovak, O. Dusa, and T. Reininger. Temperature dependence of the magnetization and of the other physical properties of rapidly quenched amorphous cob alloys. *IEEE Transactions on Magnetics*, 30:524–526, 1994. doi: 10.1109/20.312324. URL https://ieeexplore.ieee.org/document/312324.

[142] R Lavrijsen. Magnetic properties of perpendicularly magnetized ultrathin pt/co100- x- yfexby/pt films cjt loermans. 2009.

[143] Jamileh Beik Mohammadi, Bartek Kardasz, Georg Wolf, Yizhang Chen, Mustafa Pinarbasi, and Andrew D. Kent. Reduced exchange interactions in magnetic tunnel junction free layers with insertion layers. *ACS Applied Electronic Materials*,

1:2025–2029, Oct 2019. doi: 10.1021/acsaelm.9b00381. URL https://doi.org/10.1021/acsaelm.9b00381.

[144] Gyung-Min Choi. Exchange stiffness and damping constants of spin waves in cofeb films. *Journal of Magnetism and Magnetic Materials*, 516:167335, 2020. doi: https://doi.org/10.1016/j.jmmm.2020.167335. URL https://www.sciencedirect.com/science/article/pii/S0304885320323027.

[145] A. Hrabec, N. A. Porter, A. Wells, M. J. Benitez, G. Burnell, S. McVitie, D. McGrouther, T. A. Moore, and C. H. Marrows. Measuring and tailoring the dzyaloshinskii-moriya interaction in perpendicularly magnetized thin films. *Phys. Rev. B*, 90:020402, 2014. doi: 10.1103/PhysRevB.90.020402. URL https://link.aps.org/doi/10.1103/PhysRevB.90.020402.

[146] Parnika Agrawal, Felix Büttner, Ivan Lemesh, Sarah Schlotter, and Geoffrey S. D. Beach. Measurement of interfacial dzyaloshinskii-moriya interaction from static domain imaging. *Phys. Rev. B*, 100:104430, 2019. doi: 10.1103/PhysRevB.100.104430. URL https://link.aps.org/doi/10.1103/PhysRevB.100.104430.

[147] Ivan Lemesh, Felix Büttner, and Geoffrey S. D. Beach. Accurate model of the stripe domain phase of perpendicularly magnetized multilayers. *Phys. Rev. B*, 95:174423, 2017. doi: 10.1103/PhysRevB.95.174423. URL https://link.aps.org/doi/10.1103/PhysRevB.95.174423.

[148] T. N. G. Meier, M. Kronseder, and C. H. Back. Domain-width model for perpendicularly magnetized systems with dzyaloshinskii-moriya interaction. *Phys. Rev. B*, 96:144408, 2017. doi: 10.1103/PhysRevB.96.144408. URL https://link.aps.org/doi/10.1103/PhysRevB.96.144408.

[149] K. Zeissler, M. Mruczkiewicz, S. Finizio, J. Raabe, P. M. Shepley, A. V. Sadovnikov, S. A. Nikitov, K. Fallon, S. McFadzean, S. McVitie, T. A. Moore, G. Burnell, and C. H. Marrows. Pinning and hysteresis in the field dependent diameter evolution of skyrmions in pt/co/ir superlattice stacks. *Scientific Reports*, 7:15125, 2017. doi: 10.1038/s41598-017-15262-3. URL https://doi.org/10.1038/s41598-017-15262-3.

[150] G. Venkat, D. Kumar, M. Franchin, O. Dmytriiev, M. Mruczkiewicz, H. Fangohr, A. Barman, M. Krawczyk, and A. Prabhakar. Proposal for a stand-

ard micromagnetic problem: Spin wave dispersion in a magnonic waveguide. *IEEE Trans. Magn.*, 49:524–529, 2013. doi: 10.1109/TMAG.2012.2206820. URL https://ieeexplore.ieee.org/document/6228538.

[151] Jiadong Zang, Maxim Mostovoy, Jung Hoon Han, and Naoto Nagaosa. Dynamics of skyrmion crystals in metallic thin films. *Phys. Rev. Lett.*, 107:136804, 2011. doi: 10.1103/PhysRevLett.107.136804. URL https://link.aps.org/doi/10.1103/PhysRevLett.107.136804.

[152] Junichi Iwasaki, Masahito Mochizuki, and Naoto Nagaosa. Current-induced skyrmion dynamics in constricted geometries. *Nature Nanotech.*, 8:742–747, 2013. doi: 10.1038/nnano.2013.176. URL https://doi.org/10.1038/nnano.2013.176.

[153] A. V. Chumak, A. A. Serga, and B. Hillebrands. Magnonic crystals for data processing. *J. Phys. D: Appl. Phys.*, 50:244001, 2017. doi: 10.1088/1361-6463/aa6a65. URL https://dx.doi.org/10.1088/1361-6463/aa6a65.

[154] Xiaoyong Liu, Wenzhe Zhang, Matthew J. Carter, and Gang Xiao. Ferromagnetic resonance and damping properties of cofeb thin films as free layers in mgo-based magnetic tunnel junctions. *Journal of Applied Physics*, 110:033910, 2011. doi: 10.1063/1.3615961. URL https://doi.org/10.1063/1.3615961.

[155] A. Conca, E. Th. Papaioannou, S. Klingler, J. Greser, T. Sebastian, B. Leven, J. Lösch, and B. Hillebrands. Annealing influence on the gilbert damping parameter and the exchange constant of CoFeB thin films. *Applied Physics Letters*, 104:182407, 2014. doi: 10.1063/1.4875927. URL https://doi.org/10.1063/1.4875927.

[156] Young-Gwan Choi and Gyung-Min Choi. Investigation of stiffness and damping constant of spin waves in a soft magnet $Co_{100-x}B_x$ alloy. *Applied Physics Letters*, 121:012404, 2022. doi: 10.1063/5.0098398. URL https://doi.org/10.1063/5.0098398.

[157] Xichao Zhang, G. P. Zhao, Hans Fangohr, J. Ping Liu, W. X. Xia, J. Xia, and F. J. Morvan. Skyrmion-skyrmion and skyrmion-edge repulsions in skyrmion-based racetrack memory. *Scientific Reports*, 5:7643, 2015. doi: 10.1038/srep07643. URL https://doi.org/10.1038/srep07643.

[158] Sheng Yang, Kai Wu, Yuelei Zhao, Xue Liang, Jing Xia, Yuqing Zhou, Xiangjun Xing, and Yan Zhou. Inhibition of skyrmion Hall effect by a stripe domain wall. *Phys. Rev. Applied*, 18:024030, 2022. doi: 10.1103/PhysRevApplied.18.024030. URL https://link.aps.org/doi/10.1103/PhysRevApplied.18.024030.

[159] Lin Huang, Gavin Burnell, and Christopher H. Marrows. Transient retrograde motion of spin wave driven skyrmions in magnetic nanotracks. *Phys. Rev. B*, 107: 224418, 2023. doi: 10.1103/PhysRevB.107.224418. URL https://link.aps.org/doi/10.1103/PhysRevB.107.224418.

[160] Mahmoud Nasrollahzadeh, Monireh Atarod, Mohaddeseh Sajjadi, S. Mohammad Sajadi, and Zahra Issaabadi. Chapter 6 - plant-mediated green synthesis of nanostructures: Mechanisms, characterization, and applications. In Mahmoud Nasrollahzadeh, S. Mohammad Sajadi, Mohaddeseh Sajjadi, Zahra Issaabadi, and Monireh Atarod, editors, *An Introduction to Green Nanotechnology*, volume 28 of *Interface Science and Technology*, pages 199–322. Elsevier, 2019. doi: https://doi.org/10.1016/B978-0-12-813586-0.00006-7. URL https://www.sciencedirect.com/science/article/pii/B9780128135860000067.

[161] Aaron Clauset, Cosma Rohilla Shalizi, and M. E. J. Newman. Power-law distributions in empirical data. *SIAM Review*, 51:661–703, 2009. doi: 10.1137/070710111. URL https://doi.org/10.1137/070710111.

[162] Chia-Yun Lai, Tuza Olukan, Sergio Santos, Amal Al Ghaferi, and Matteo Chiesa. The power laws of nanoscale forces under ambient conditions. *Chem. Commun.*, 51:17619–17622, 2015. doi: 10.1039/C5CC05755H. URL http://dx.doi.org/10.1039/C5CC05755H.

[163] Asylum Research. *Asylum research — atomic force microscope manufacturer*. URL https://afm.oxinst.com/assets/uploads/products/asylum/documents/VFM4-DS-22MAR2021.pdf.

[164] Milton Ohring. 14 - magnetic properties of materials. In Milton Ohring, editor, *Engineering Materials Science*, pages 711–746. Academic Press, 1995. ISBN 978-0-12-524995-9. doi: https://doi.org/10.1016/B978-012524995-9/50038-6. URL https://www.sciencedirect.com/science/article/pii/B9780125249959500386.

[165] Anne Henschel, Michael Binnewies, Marcus Schmidt, Ulrich Burkhardt, Yurii Prots, and Yuri Grin. Preparation of cobalt borides by solid-gas reactions. *Dalton Transactions*, 48:17184–17191, 2019. doi: 10.1039/C9DT03249E. URL http://dx.doi.org/10.1039/C9DT03249E.

[166] J. Borowiecka-Jamrozek and J. Lachowski. Diffusion of boron in cobalt sinters. *Archives of Metallurgy and Materials*, 58:1131 1136, 2013. doi: 10.2478/amm-2013-0137. URL http://journals.pan.pl/Content/87941/PDF/10172%20Volume%2058%20Issue%204-20%20paper.pdf.pdf.

[167] Sita Dugu, Karuna Kara Mishra, Dhiren K. Pradhan, Shalini Kumari, and Ram S. Katiyar. Coupled phonons and magnetic orderings in GaFeO3: Raman and magnetization studies. *Journal of Applied Physics*, 125:064101, 02 2019. doi: 10.1063/1.5072766. URL https://doi.org/10.1063/1.5072766.

[168] Serban Lepadatu. Micromagnetic Monte Carlo method with variable magnetization length based on the Landauâ€“Lifshitzâ€“Bloch equation for computation of large-scale thermodynamic equilibrium states. *Journal of Applied Physics*, 130:163902, 10 2021. doi: 10.1063/5.0059745. URL https://doi.org/10.1063/5.0059745.

[169] Zhuolin Li, Qiangwei Yin, Yi Jiang, ZhaoZhao Zhu, Yang Gao, Shouguo Wang, Jun Shen, Tongyun Zhao, Jianwang Cai, Hechang Lei, Shi-Zeng Lin, Ying Zhang, and Baogen Shen. Discovery of topological magnetic textures near room temperature in quantum magnet tbmn6sn6. *Advanced Materials*, 35:2211164, 2023. doi: https://doi.org/10.1002/adma.202211164. URL https://onlinelibrary.wiley.com/doi/abs/10.1002/adma.202211164.

[170] Dmitry A. Garanin, Eugene M. Chudnovsky, Senfu Zhang, and Xixiang Zhang. Thermal creation of skyrmions in ferromagnetic films with perpendicular anisotropy and dzyaloshinskii-moriya interaction. *Journal of Magnetism and Magnetic Materials*, 493:165724, 2020. ISSN 0304-8853. doi: https://doi.org/10.1016/j.jmmm.2019.165724. URL https://www.sciencedirect.com/science/article/pii/S0304885319316713.

[171] J.D. Wei, M. Kirsch, M.R. Koblischka, and U. Hartmann. Optimization of high-frequency magnetic force microscopy by ferrite-coated cantilevers. *Journal*

of Magnetism and Magnetic Materials, 316:206–209, 2007. doi: https://doi.org/10.1016/j.jmmm.2007.02.088. URL https://www.sciencedirect.com/science/article/pii/S0304885307001722. Proceedings of the Joint European Magnetic Symposia.

[172] Asylum. Asymfmlc-r2. *ASYMFMLC-R2 - Asylum Research AFM Probe Store*. URL https://estore.oxinst.com/eu/products/microscopy-supplies/search-by-mode/magnetic-force-microscopy-(mfm)/zid805.ASYMFM.LC-R2#product-description.

[173] Bruker. Mesp-lm-v2. *Bruker AFM Probes - MESP-LM-V2*. URL https://www.brukerafmprobes.com/p-3952-mesp-lm-v2.aspx.

[174] M.M. Waite and S. Ismat Shah. Target poisoning during reactive sputtering of silicon with oxygen and nitrogen. *Materials Science and Engineering: B*, 140:64–68, 2007. doi: https://doi.org/10.1016/j.mseb.2007.04.001. URL https://www.sciencedirect.com/science/article/pii/S0921510707001924.

[175] J. Sampaio, V. Cros, S. Rohart, A. Thiaville, and A. Fert. Nucleation stability and current-induced motion of isolated magnetic skyrmions in nanostructures. *Nature Nanotech.*, 8:839–844, 2013. doi: 10.1038/nnano.2013.210. URL https://doi.org/10.1038/nnano.2013.210.

[176] Olle Heinonen, Wanjun Jiang, Hamoud Somaily, Suzanne G. E. te Velthuis, and Axel Hoffmann. Generation of magnetic skyrmion bubbles by inhomogeneous spin Hall currents. *Phys. Rev. B*, 93:094407, 2016. doi: 10.1103/PhysRevB.93.094407. URL https://link.aps.org/doi/10.1103/PhysRevB.93.094407.

[177] Yang Zhao, Dongying Guo, Zhongming Zeng, Maokang Shen, Yue Zhang, Riccardo Tomasello, Giovanni Finocchio, Ruilong Wang, and Shiheng Liang. 24:053053, 2022. doi: 10.1088/1367-2630/ac6c45. URL https://dx.doi.org/10.1088/1367-2630/ac6c45.

[178] D. Hinzke and U. Nowak. Domain wall motion by the magnonic spin seebeck effect. *Phys. Rev. Lett.*, 107:027205, 2011. doi: 10.1103/PhysRevLett.107.027205. URL https://link.aps.org/doi/10.1103/PhysRevLett.107.027205.

[179] Qi-Chao Sun, Tiancheng Song, Eric Anderson, Andreas Brunner, Johannes Förster, Tetyana Shalomayeva, Takashi Taniguchi, Kenji Watanabe, Joachim Gräfe, Rainer Stöhr, Xiaodong Xu, and Jörg Wrachtrup. Magnetic domains and domain wall pinning in atomically thin crbr3 revealed by nanoscale imaging. *Nature Communications*, 12:1989, 2021. doi: 10.1038/s41467-021-22239-4. URL https://doi.org/10.1038/s41467-021-22239-4.

[180] O. Gladii, M. Collet, K. Garcia-Hernandez, C. Cheng, S. Xavier, P. Bortolotti, V. Cros, Y. Henry, J.-V. Kim, A. Anane, and M. Bailleul. Spin wave amplification using the spin Hall effect in permalloy/platinum bilayers. *Applied Physics Letters*, 108:202407, 2016. doi: 10.1063/1.4952447. URL https://doi.org/10.1063/1.4952447.

[181] Satoshi Sugimoto, Mark C. Rosamond, Edmund H. Linfield, and Christopher H. Marrows. Observation of spin-wave Doppler shift in Co90Fe10/Ru micro-strips for evaluating spin polarization. *Applied Physics Letters*, 109:112405, 2016. doi: 10.1063/1.4962835. URL https://doi.org/10.1063/1.4962835.

[182] Xiuzhen Yu, Fumitaka Kagawa, Shinichiro Seki, Masashi Kubota, Jan Masell, Fehmi S. Yasin, Kiyomi Nakajima, Masao Nakamura, Masashi Kawasaki, Naoto Nagaosa, and Yoshinori Tokura. Real-space observations of 60-nm skyrmion dynamics in an insulating magnet under low heat flow. *Nature Communications*, 12:5079, 2021. doi: 10.1038/s41467-021-25291-2. URL https://doi.org/10.1038/s41467-021-25291-2.